ผลของโลหะออกไซด์ต่อกัมมันตภาพและเสถียรภาพของตัวเร่งปฏิกิริยาเชิงไฟฟ้าแพลทินัม-
โคบอลต์/คาร์บอนสำหรับรีดักชันของออกซิเจนในเซลล์เชื้อเพลิงพีอีเอ็ม

นางสาวณภาภัช ไชยทรัพย์อนันต์

วิทยานิพนธ์นี้เป็นส่วนหนึ่งของการศึกษาตามหลักสูตรปริญญาวิทยาศาสตรดุษฎีบัณฑิต
สาขาวิชาเคมีเทคนิค ภาควิชาเคมีเทคนิค
คณะวิทยาศาสตร์ จุฬาลงกรณ์มหาวิทยาลัย
ปีการศึกษา 2558

EFFECTS OF METAL OXIDE ON ACTIVITY AND STABILITY OF Pt-Co/C ELECTROCATALYSTS FOR OXYGEN REDUCTION IN PEM FUEL CELLS

Miss Napapat Chaisubanan

จุฬาลงกรณ์มหาวิทยาลัย
CHULALONGKORN UNIVERSITY

A Dissertation Submitted in Partial Fulfillment of the Requirements

for the Degree of Doctor of Philosophy Program in Chemical Technology

Department of Chemical Technology

Faculty of Science

Chulalongkorn University

Academic Year 2015

| | |
|---|---|
| Thesis Title | EFFECTS OF METAL OXIDE ON ACTIVITY AND STABILITY OF Pt-Co/C ELECTROCATALYSTS FOR OXYGEN REDUCTION IN PEM FUEL CELLS |
| By | Miss Napapat Chaisubanan |
| Field of Study | Chemical Technology |
| Thesis Advisor | Professor Mali Hunsom, Ph.D.,  Dr. de l'INP |
| Thesis Co-Advisor | Associate Professor Kejvalee Pruksathorn, Dr. de l'INP |
| | Assistant Professor Hugues Vergnes, Dr. de l'INP |

Accepted by the Faculty of Science, Chulalongkorn University in Partial Fulfillment of the Requirements for the Doctoral Degree

　　　　　　　　　　　　　　　　　　　　　　　　　　Dean of the Faculty of Science

(Associate Professor Polkit Sangvanich, Ph.D.)

THESIS COMMITTEE

　　　　　　　　　　　　　　　　　　　　　　　　　　Chairman

(Associate Professor Somkiat Ngamprasertsith, Dr. de l'INP)

　　　　　　　　　　　　　　　　　　　　　　　　　　Thesis Advisor

(Professor Mali Hunsom, Ph.D.,  Dr. de l'INP)

　　　　　　　　　　　　　　　　　　　　　　　　　　Thesis Co-Advisor

(Associate Professor Kejvalee Pruksathorn, Dr. de l'INP)

　　　　　　　　　　　　　　　　　　　　　　　　　　Thesis Co-Advisor

(Assistant Professor Hugues Vergnes, Dr. de l'INP)

　　　　　　　　　　　　　　　　　　　　　　　　　　Examiner

(Assistant Professor Kunakorn Poochinda, Ph.D.)

　　　　　　　　　　　　　　　　　　　　　　　　　　Examiner

(Assistant Professor Nisit Tantavichet, Ph.D.)

　　　　　　　　　　　　　　　　　　　　　　　　　　External Examiner

(Associate Professor Terdthai Vatanatham, Ph.D.)

ณภาภัช ไชยทรัพย์อนันต์ : ผลของโลหะออกไซด์ต่อกัมมันตภาพและเสถียรภาพของตัวเร่งปฏิกิริยาเชิงไฟฟ้าแพลทินัม-โคบอลต์/คาร์บอนสำหรับรีดักชันของออกซิเจนในเซลล์เชื้อเพลิงพีอีเอ็ม (EFFECTS OF METAL OXIDE ON ACTIVITY AND STABILITY OF Pt-Co/C ELECTROCATALYSTS FOR OXYGEN REDUCTION IN PEM FUEL CELLS) อ.ที่ปรึกษาวิทยานิพนธ์หลัก: ศ. ดร. มะลิ หุ่นสม Ph.D., Dr. de l'INP, อ.ที่ปรึกษาวิทยานิพนธ์ร่วม: รศ. ดร. เก็จวลี พฤกษาทร Dr. de l'INP, ผศ. ดร. อุ๊ก แวงฝ Dr. de l'INP, 127 หน้า.

งานวิจัยนี้ศึกษาผลของโลหะออกไซด์ต่อกัมมันตภาพและเสถียรภาพของตัวเร่งปฏิกิริยาเชิงไฟฟ้าแพลทินัม-โคบอลต์/คาร์บอน ตัวแปรในการศึกษา คือ ชนิดของโลหะออกไซด์ ($TiO_2$ $MoO_2$ และ $CeO_2$) ปริมาณโลหะออกไซด์ (0.03-0.45 มิลลิกรัมต่อตารางเซนติเมตร) และศึกษาเปรียบเทียบผลของ $TiO_2$ ที่เตรียมจากวิธีการพอกพูนด้วยไอเคมี (Chemical vapor deposition) กับ $TiO_2$ เชิงพาณิชย์ จากผลการทดลองพบว่าชนิดและปริมาณไม่ส่งผลต่อโครงสร้างผลึกและสัณฐานวิทยาของตัวเร่งปฏิกิริยาเชิงไฟฟ้าแพลทินัม-โคบอลต์/คาร์บอน ในส่วนของการทดสอบกัมมันตภาพและสมรรถนะของตัวเร่งปฏิกิริยาในเซลล์เชื้อเพลิง พบว่าการเติม $CeO_2$ และ $MoO_2$ ให้ผลในเชิงลบ ในขณะที่การเติม $TiO_2$ เชิงพาณิชย์ในปริมาณตั้งแต่ 0.03-0.06 มิลลิกรัมต่อตารางเซนติเมตร สามารถเพิ่มกัมมันตภาพของตัวเร่งปฏิกิริยาและสมรรถนะของเซลล์เชื้อเพลิงให้สูงขึ้นได้ โดยค่าความหนาแน่นกระแสไฟฟ้าทางจลนพลศาสตร์และความหนาแน่นกระแสไฟฟ้าในเซลล์เชื้อเพลิงที่ 0.6 โวลต์ ของตัวเร่งปฏิกิริยาเชิงไฟฟ้าแพลทินัม-โคบอลต์/คาร์บอนมีค่าสูงสุด (8.05 และ 435 มิลลิแอมแปร์ต่อตารางเซนติเมตร ตามลำดับ) ที่ปริมาณ $TiO_2$ เท่ากับ 0.06 มิลลิกรัมต่อตารางเซนติเมตร ส่วนค่าดังกล่าวสำหรับ $TiO_2$ ที่เตรียมโดยวิธีการพอกพูนด้วยไอเคมีจะมีค่าสูงกว่าเล็กน้อย คือ 20.24 และ 454.80 มิลลิแอมแปร์ต่อตารางเซนติเมตร ตามลำดับ ในส่วนการศึกษาผลของโลหะออกไซด์ต่อเสถียรภาพของตัวเร่งปฏิกิริยาเชิงไฟฟ้าแพลทินัม-โคบอลต์/คาร์บอน พบว่า $CeO_2$ และ $MoO_2$ ไม่สามารถส่งเสริมเสถียรภาพของตัวเร่งปฏิกิริยาได้ ในขณะที่ $TiO_2$ ให้ผลในเชิงบวกต่อเสถียรภาพของตัวเร่งปฏิกิริยา

| ภาควิชา | เคมีเทคนิค | ลายมือชื่อนิสิต | |
|---|---|---|---|
| สาขาวิชา | เคมีเทคนิค | ลายมือชื่อ อ.ที่ปรึกษาหลัก | |
| ปีการศึกษา | 2558 | ลายมือชื่อ อ.ที่ปรึกษาร่วม | |
| | | ลายมือชื่อ อ.ที่ปรึกษาร่วม | |

# # 5472820923 : MAJOR CHEMICAL TECHNOLOGY

KEYWORDS: PLATINUM-COBALT ALLOY CATALYST / ORR ACTIVITY / CATALYST STABILITY / PEM FUEL CELL

NAPAPAT CHAISUBANAN: EFFECTS OF METAL OXIDE ON ACTIVITY AND STABILITY OF Pt-Co/C ELECTROCATALYSTS FOR OXYGEN REDUCTION IN PEM FUEL CELLS. ADVISOR: PROF. MALI HUNSOM, Ph.D., Dr. de l'INP, CO-ADVISOR: ASSOC. PROF. KEJVALEE PRUKSATHORN, Dr. de l'INP, ASST. PROF. HUGUES VERGNES, Dr. de l'INP, 127 pp.

This work was carried out to study the effect of metal oxide ($MO_2$) on activity and stability of Pt-Co/C electrocatalyst. The investigated parameters were types of the metal oxides ($TiO_2$, $MoO_2$, and $CeO_2$) and the loadings of the metal oxide ($0.03 – 0.45$ mg/cm$^2$) and also compared the effect of $TiO_2$ prepared by chemical vapor deposition and commercial $TiO_2$. The experiment reported that the types of the metal oxide, quantity did not influence to the structure and the morphology of Pt-Co/C electrocatalyst. For the test of ORR activity in acid electrolyte and in PEM fuel cell, it was found that the addition of $CeO_2$ and $MoO_2$ provided the negative result, while adding the commercial $TiO_2$ by 0.03 up to 0.06 mg/cm$^2$ could increase the ORR activity test. The kinetic current density and current density at 0.6 V of the Pt-Co/C electrocatalyst were around 8.05 mA/cm$^2$ and 435 mA/cm$^2$, respectively when approximately 0.06 mg/cm$^2$ of $TiO_2$ were added. For the $TiO_2$ prepared by the chemical vapor deposition technique, it provided a higher rate up to 20.24 and 454.80 mA/cm$^2$, respectively. Regarding the stability, the $CeO_2$ and $MoO_2$ could not improve the stability of the Pt-Co/C electrocatalyst, while the $TiO_2$ gave the positive effect.

| | | | |
|---|---|---|---|
| Department: | Chemical Technology | Student's Signature | |
| Field of Study: | Chemical Technology | Advisor's Signature | |
| Academic Year: | 2015 | Co-Advisor's Signature | |
| | | Co-Advisor's Signature | |

# ACKNOWLEDGEMENTS

# CONTENTS

## LIST OF TABLES

LIST OF FIGURES

# CHAPTER 1

## Introduction

### 1.1 Motivation

Proton exchange membrane (PEM) fuel cells are currently recognized as the most competitive candidate to replace traditional forms of power conversion devices due to their various advantages, including their zero emissions, high efficiency and relatively simple design and operation [1, 2]. They are able to meet the transportation and stationary power requirements owing to their low operating temperature, quick start, light weight and high power density [3]. Although the PEM fuel cells have various advantages, their commercialization and utilization are still not currently widespread because of two major technical gaps: their high cost and low reliability and durability [4].

Theoretically, the cell potential of PEM fuel cell is 1.23 V/SHE. However, in actual application, there are many losses in fuel cell including activation-, ohmic- and concentration losses. The fuel cell voltage is directly proportional to the exchange current density which is the electrical properties of the electrocatalyst. The exchange current density for the hydrogen oxidation reaction (HOR) is greater than that of the oxygen reduction reaction (ORR), resulting in a fast reaction rate of HOR in comparison to that of ORR. The alloying between Pt and other metal was selected to improve the catalytic activity. The exchange current density of Pt-M alloy for ORR is higher than that of pure platinum [5]. This is because the composite metal (M) in Pt-M alloy electrocatalysts can modify the geometrical structure of the Pt metal via decreasing the Pt-Pt bond distance [6], dissolution of the more oxidizable alloying component [7], and changing the surface structure [8] or the electronic structure by increasing the Pt $d$-electron vacancy [9].

The loss of PEM fuel cells stability has been explained by the loss of active surface area due in part to various factors including *(i)* metal coalescence, the growth of particles due to dissolution/precipitation process (Ostwald ripening), *(ii)* metal cluster migration and coalescence [10], *(iii)* metal loss by dissolution into the electrolyte [11] and *(iv)* support

corrosion associated with a loss of electrical contact of metal nanoparticles [12]. It has been found that the solubility of Pt is proportional to potential, pH of acid solution as well as reciprocal of particle size. It is crucial to find corrosion resistant (highly stable) electrocatalysts for improving the durability of PEM fuel cell. Recently, metal oxide such as $CeO_2$, $ZrO_2$ were introduced to a Pt/C electrocatalyst resulting in higher sintering resistance and corrosion resistance for PEM fuel cells [13, 14].

This research studies the effect of metal oxide on activity and stability of PtCo/C electrocatalyst to get a highly effective catalyst and to reduce the amount of platinum used, which can reduce the cost of fuel cells for commercialization and utilization.

## 1.2 Objectives

1. To investigate the effect of $MO_x$ on the activity and stability of PtCo/C electrocatalyst
2. To optimize the $MO_x$- PtCo /C preparation conditions for the oxygen reduction reaction (ORR)

## 1.3 Scopes of the dissertation

1. Literature review for involved publications from both national and international journals
2. Prepare all tools, equipments and chemical reagents required for the experiments
3. Prepare $MO_x$-PtCo/C electrocatalyst by the combined process of impregnation and seeding technique
4. Prepare $TiO_2$ on gas diffusion layer by chemical vapor deposition (CVD) technique

5.  Investigate the effect of $MO_x$ on the morphology of PtCo/C electrocatalysts, such as particle size, metal dispersion, crystal structure, electrochemical surface area (ESA)

6.  Investigate the effect of as-prepared $MO_x$ on the activity of PtCo/C electrocatalysts for ORR under $H_2/O_2$ condition and in acid electrolyte

7.  Study the stability of as-prepared $MO_x$-PtCo/C electrocatalysts in acid electrolyte by using cyclic voltammetry (CV)

8.  Analyze the experimental results, make conclusions and write the dissertation

## 1.4 Anticipated benefits

1.  Know the effect of the metal oxide on morphology, activity and stability of PtCo/C electrocatalyst

2.  Obtain the $MO_x$-PtCo/C electrocatalystes that have high activity, stability and suitable for using in PEM fuel cell
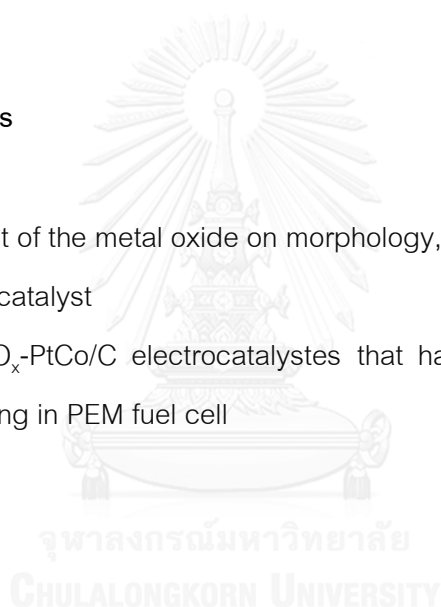
# CHAPTER 2
## Theory and Literature Review

Fuel cells can converts the chemical energy contained in hydrocarbon materials into thermal energy (heat), mechanical energy, and finally to electricity via an electric generator. Each stage has its own efficiency, with the overall efficiency up to over 30%. In addition, they allow a direct conversion of chemical energy to electricity, to ensure a high yields up to 50% [15]. This conversion process can be realized by different technologies depending on the intended applications.

## 2.1 History and characterization of fuel cell [16, 17]

The fuel cell principle was first demonstrated in 1801 by Humphry Davy. In 1839, William Grove fabricated a gas voltaic battery, which justified that an electric current could be generated from an electrochemical reaction between hydrogen and oxygen. In 1889, Charles Langer and Ludwig Mond discovered fuel cells by using coal gas as a fuel. The electrochemical process that presented the heart of each is summarized by the equation below:

$$H_2 + \frac{1}{2}O_2 \rightarrow H_2O + \text{Heat} \qquad (2.1)$$

The combination of a mole of hydrogen with a half mole of oxygen allows the production of water and heat. The chemical energy contained in the reagents is converted into electric energy as well as heat as showed in Figure 2.1. The operation of the fuel cell may appear relatively simple.
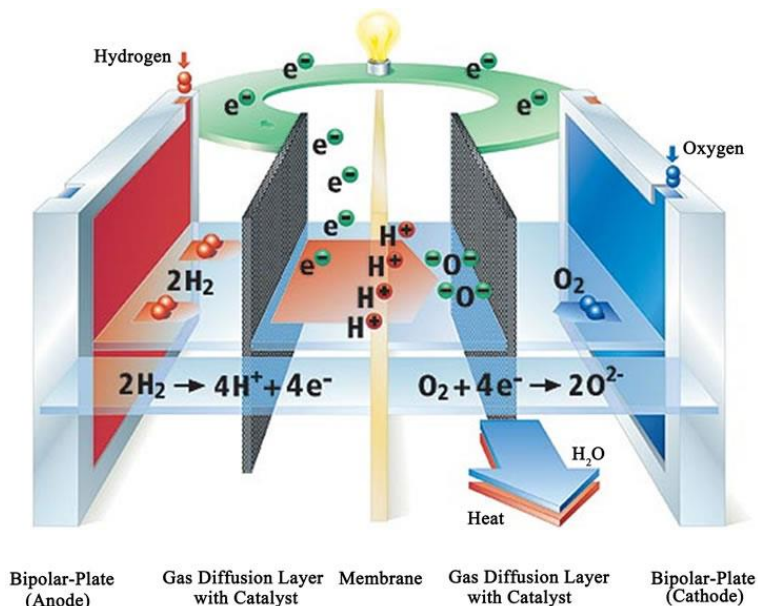
Figure 2. 1 Scheme of proton exchange membrane (PEM) fuel cell [18].

| Typical applications | Portable electronics equipment | Car, boats, and domestic combined heat and power | Distributed power generation, combined heat and power, also buses |
|---|---|---|---|
| Power in Watts | 1    10    100 | 1k    10k | 100k    1M    10M |
| Main advantages | Higher energy density than batteries Faster recharging | Potential for zero emissions Higher efficiency | Less pollution quiet Higher efficiency |

Range of application of the different types of fuel cell

DEMFC        AFC        MCFC

SOFC

PEMFC

PAFC

Figure 2. 2 Summarized chart of the fuel cell applications and advantages [19].

The fuel cells have many advantages, such as higher efficiency than diesel or gas engines, eliminate pollution or greenhouse gases, hydrogen (fuel gas) can be produced anywhere where there is water as a source of power, operating times are much longer than batteries, and etc.[19]. The advantages of each fuel cells are summarized as shown in Figure 2.2.

Although the fuel cell has a lot of advantages, it is still not popular in commercial and utilization because of the costly demanded, low reliability and durability [19].

## 2.2 Types of fuel cell [17]

Many fuel cell technologies are distinguished either by their fuel used (hydrogen, methanol, ethanol, biomass etc.), temperature range (40 to 800 °C) or type of electrolyte (polymer, ceramic, alkaline solution, acid solution). In this section, we will classify the fuel cells by the type of electrolyte.

### 2.2.1 Alkaline fuel cell

The alkaline fuel cell (AFC) has been developed since 1932. The ion carrier is potassium hydroxide (KOH), it contains the highest ions carrier ability compared with the other hydroxide groups. The cell temperature is approximately 200 °C. The reactions for AFC are shown below:

Anode         :         $H_{2(g)} + 2OH^-_{(aq)} \longrightarrow 2H_2O_{(l)} + 2e^-$         (2.2)

Cathode       :         $\frac{1}{2}O_{2(g)} + H_2O_{(g)} + 2e^- \longrightarrow 2OH^-_{(aq)}$         (2.3)

Total    :         $H_{2(g)} + \frac{1}{2}O_{2(g)} \longrightarrow H_2O_{(g)}$         (2.4)
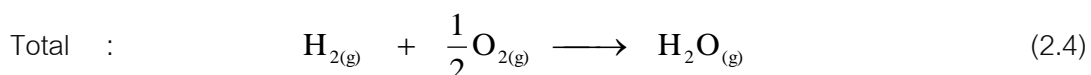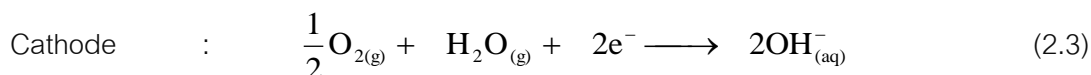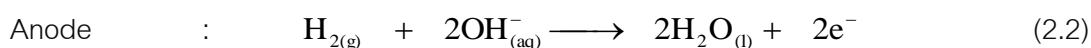
### 2.2.2 Phosphoric acid fuel cell

The phosphoric acid is the ion carriers used in the phosphoric acid fuel cell (PAFC). The operating temperature is 170-200 °C, the temperature at which a substance

also causes the charge carriers stable. The catalyst used is a noble metal. The reaction

for AFC are shown below:

Anode          :          $H_{2(g)} \longrightarrow 2H^+_{(aq)} + 2e^-$                                          (2.5)

Cathode        :          $\frac{1}{2}O_{2(g)} + 2H^+_{(aq)} + 2e^- \longrightarrow H_2O_{(g)}$              (2.6)

Total          :          $H_{2(g)} + \frac{1}{2}O_{2(g)} \longrightarrow H_2O_{(g)}$                        (2.7)
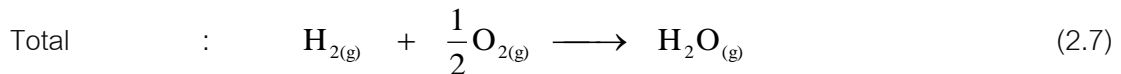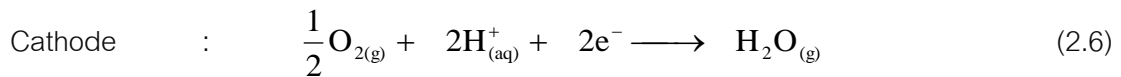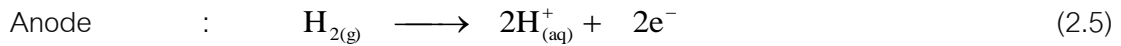
### 2.2.3 Molten carbonate fuel cell

A mixture of salt, lithium carbonate and potassium carbonate salt on lithium

alumina ($LiAlO_2$) are used as carriers in this fuel cell. The operating temperature is 500-

700 °C.

Anode          :          $H_{2(g)} + CO_3^{2-} \longrightarrow CO_{2(g)} + H_2O_{(g)} + 2e^-$          (2.8)

Cathode        :          $\frac{1}{2}O_{2(g)} + CO_{2(g)} + 2e^- \longrightarrow CO_3^{2-}$                (2.9)

Total          :          $H_{2(g)} + \frac{1}{2}O_{2(g)} \longrightarrow H_2O_{(g)}$                        (2.10)
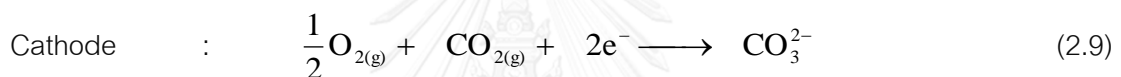
### 2.2.4 Solid oxide fuel cell

Solid oxide fuel cell (SOFC) is suitable for the large power stations because it

produces little electricity. Meanwhile, it can produce steam at high temperature, which

could be used to fabricate a gas turbine to generate electricity as well. However, this fuel

cell has to work at high temperature up to 1000 °C. The reactions are described as

following.

Anode :          $aH_{2(g)} + bCO_{(g)} + (a+b)O^{2-} \longrightarrow aH_2O_{(g)} + bCO_{2(g)} + 2(a+b)e^-$          (2.11)

Cathode:          $\frac{1}{2}(a+b)O_{2(g)} + 2(a+b)e^- \longrightarrow 2(a+b)O^{2-}$                        (2.12)

Total:          $aH_{2(g)} + \frac{1}{2}(a+b)O_{2(g)} + bCO_{(g)} \longrightarrow aH_2O_{(g)} + bCO_{2(g)}$          (2.13)
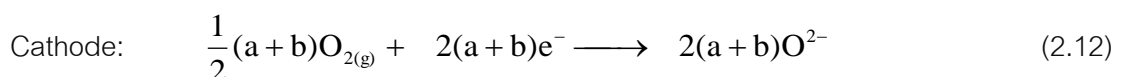
*2.2.5 Direct methanol fuel cell*

The direct methanol fuel cell (DEMFC) is one type of fuel cell that get a lot of attention in development. The principle of DEMFC is similar to the one of PEM fuel cell. The difference is that the methanol is used instead of $H_2$. The advantage is that methanol can be stored easily, portable and secure than using hydrogen gas as fuel as PEM fuel cells. The reactions are shown as following:

Anode :   $$CH_3OH_{(l)} + H_2O \longrightarrow CO_{2(g)} + 6H^+ + 6e^- \qquad (2.14)$$

Cathode:   $$\frac{3}{2}O_{2(g)} + 6H^+ + 6e^- \longrightarrow 3H_2O_{(l)} \qquad (2.15)$$

Total:   $$CH_3OH_{(l)} + \frac{3}{2}O_{2(g)} \longrightarrow CO_{2(g)} + 2H_2O_{(l)} \qquad (2.16)$$
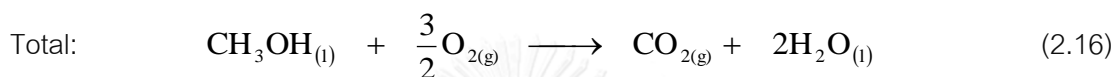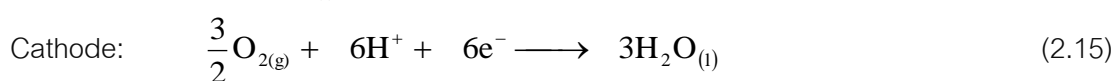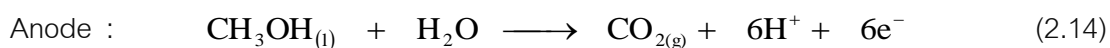
*2.2.6 Proton exchange membrane fuel cell*

The proton exchange membrane (PEM) fuel cell is consisted of two electrodes; anode and cathode. The oxidation of $H_2$ to produce electrons and protons from hydrogen gas occurs on the anode side (Reaction (2.17)) while the reduction of oxygen to produce heat and water occurs on the cathode side (Reaction (2.18)). The total reaction is summarized as reaction (2.19).

Anode :   $$H_{2(g)} \longrightarrow 2H^+_{(aq)} + 2e^- \qquad (2.17)$$

Cathode:   $$\frac{1}{2}O_{2(g)} + 2H^+_{(aq)} + 2e^- \longrightarrow H_2O_{(l)} \qquad (2.18)$$

Total:   $$H_{2(g)} + \frac{1}{2}O_{2(g)} \longrightarrow H_2O_{(g)} \qquad (2.19)$$
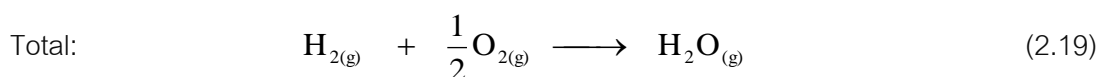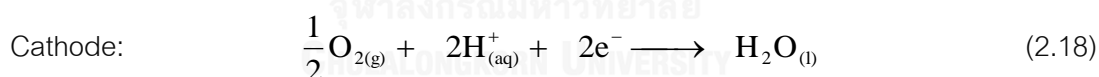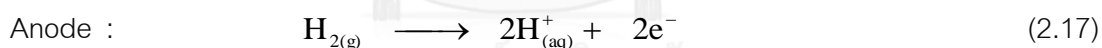
The characteristics of different types of fuel cells are summarized in Table 2.1.

Table 2. 1 Fuel cell characteristics. [15]

| Fuel cell | Charge carrier | Operating temperature (°C) | Fuel | Electrode material | Efficiency |
|---|---|---|---|---|---|
| AFC | $OH^-$ | 50-200 | Pure $H_2$ | Metal or carbon | 60 – 70% |
| PAFC | $H^+$ | 170-200 | $H_2+CO_2$ | Pt on carbon | 36 – 42% |
| MCFC | $CO_3^{2-}$ | 500-700 | $H_2+CO_2$ | Li-doped $NiO_2$ | 60% |
| SOFC | $O^{2-}$ | 500-1000 | $H_2+CO_2$ | Ni/$Y_2O_3$-$ZrO_2$, Sr-doped $LaMnO_3$ | 60% |
| DMFC | $H^+$ | 90 | $CH_3OH$ | Pt-Ru alloy | 60% |
| PEMFC | $H^+$ | 50-100 | Pure $H_2$ | Pt on carbon | 50 – 60% |

## 2.3 Proton exchange membrane (PEM) fuel cell [18, 20]

The basic phenomena of the PEM fuel cell must be described as the transportation of electron and ionic charges transport (reactants and products) via electrochemical reactions. Each of them can be described by their own law, such as Ohm's law, the Navier-Stokes or kinetics Tafel. In the operating process, hydrogen gas ($H_2$) is fed at anode side of fuel cell through the electrocatalyst layer. Then, it splits into two $H^+$ ions and two electrons ($e^-$), which is so-called hydrogen oxidation reaction (HOR). The $e^-$ and $H^+$ are respectively conducted to the cathode side by the external circuit and membrane. The $e^-$ and $H^+$ also react with oxygen ($O_2$) fed on the cathode side, which is so-called oxygen reduction reaction (ORR). The fuel cell reactions are summarized in the Equation (2.19).

The work output and/or fuel cell efficiency can be determined by thermodynamics analyzing in term of the free energy change of the reaction [19]. The Gibb's free energy of the fuel cell is expressed by the Eq. (2.20)

$$\Delta G = -nFE_r \tag{2.20}$$

Where $\Delta G$ is the changed free energy, $n$ is the number of electron, $E_r$ is the reversible potential, and $F$ is Faraday's constant.

The enthalpy ($\Delta H$) for the fuel cell reaction reveals the released heat from the reaction at the constant pressure. The fuel cell potential correspondence with $\Delta H$ is defined as Eq. (2.21).

$$\Delta H = -nFE_t \tag{2.21}$$

Where $E_t$ is the thermos-neutral potential.

Another equation that usually use to determine the fuel cell performance is Nernst equation. It can present the fuel cell potential related to reversible potential ($E_{r,T,P}$) and actual potential ($E_{cell}$) in term of temperature, pressure, and concentration of reactants and products as demonstrated in Eq. (2.22) .

$$E_{cell} = E_{r,T,P} - \eta_{act} - \eta_{ohm} - \eta_{con} \tag{2.22}$$

Where $\eta_{act}$ is the activation polarization, $\eta_{ohm}$ is the ohmic polarization, and $\eta_{con}$ is the concentration polarization.

Theoretically, the cell potential of PEM fuel cell is 1.23 V/SHE. However, in actual application, there are many losses in fuel cell including activation-, ohmic- and concentration losses. According to Eq. (2.22), the fuel cell voltage is directly proportional to the exchange current density which is the electrical properties of the electrocatalyst. It connects the current from the fuel cell to the voltage measured at its terminals, as indicated by the Figure 2.3. Experimentally, this measure is the most commonly performed, it provides the operating characteristics of the fuel cell depending on the operating conditions (reagents flow, temperature, humidity, etc.) [20].

1. The potential loss in the high potential zone is called activation loss or activation polarization. It concerns the high potential, typically between 1.0 and 0.8 V, or current densities of less than 100 mA/cm$^2$. The activation

polarization can be expressed as Equation (2.23). This scheme is controlled by the reaction kinetics which causes most of the losses.

$$\eta_{act} = \frac{RT}{\alpha nF}\left(\frac{j}{j_0}\right) \tag{2.23}$$

Where $R$ is gas constant, $T$ is absolute temperature, $\alpha$ is the mass transfer coefficient, $F$ is the Faraday's constant, $j$ is the current density, $j_0$ is the exchange current density.

2. The ohmic loss concerns the intermediate potential range between 0.8 and 0.4 V (around 500 mA/cm$^2$). This loss is relatively linear as shown in Eq. (2.24).

$$\eta_{ohm} = jR_i \tag{2.24}$$

Where $R_i$ is the internal resistance.

   All electrochemical phenomena, ohmic, and diffusion of the reactants have an influence. Indeed, the slope of the polarization curve is often attributed by the single membrane resistance. Furthermore, this zone is generally chosen for the nominal operation of fuel cell. This is also the maximum power area.

3. The last part shows the collapse of the fuel cell voltage of 0.4 to 0.0 V or low potential zone. The loss in this zone is called the concentration loss or mass transfer loss, coming from the limiting mass transfer of fuel gas as represented in Eq. (2.25).

$$\eta_{con} = \frac{RT}{nF}\left(\frac{j_L}{j_L - j}\right) \tag{2.25}$$

Where $j_L$ is the limiting current density.

This operating area should be avoided because it usually leads to irreversible damage such as heating of the fuel cell, membrane perforation, deterioration of the catalyst, and etc.
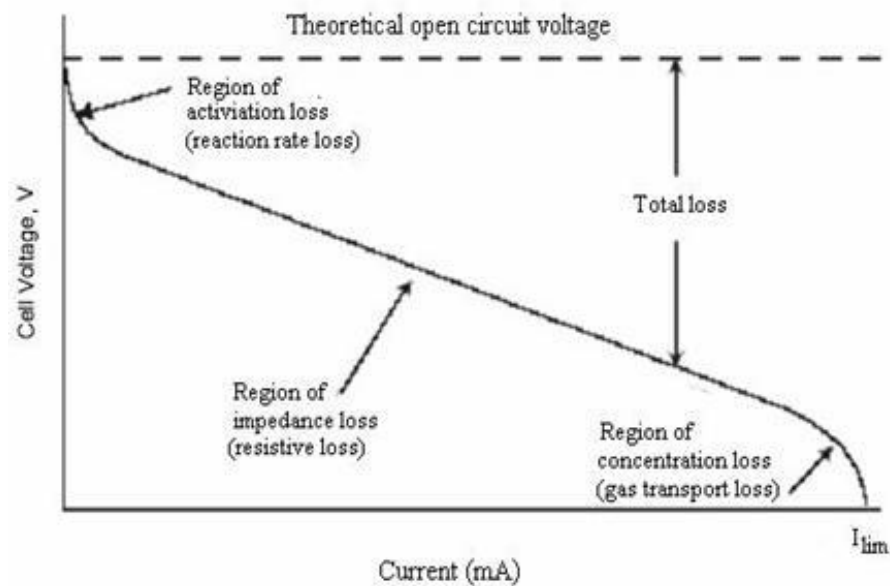


Figure 2. 3 Current / voltage characteristic of fuel cell [21].

## 2.4 Membrane electrode assembly [22-27]

Generally, the PEM fuel cell consists of gas diffusion layer (GDL), catalyst layer and electrolyte as shown in Figure 2.4 and a cross sectional photograph of MEA is shown in Figure 2.5. The left-hand side electrode is called an anode, which is enable the dissociation of the hydrogen molecule to electrons and protons. The electron go to the external load while the protons pass through the membrane to cathode and react with oxygen and other electrons from the external circuit to form water and heat. The contact area between electrolyte, electrode, and fuel gas is called triple phase boundary (TPB). The TPB density is one significant factor for PEM fuel cell performance. The TPB should contain high porosity to well disperse the fuel gasses and high ion with electron conductivity to promote the reaction rate [24]. The technical targets of the U.S.

Department of Energy for each component of MEAs for transportation applications are shown in Table 2.2-2.4.

Table 2. 2 Technical targets of electrocatalyst.

| Characteristic | Units | 2011 Status | 2017 Targets | 2020 Targets |
|---|---|---|---|---|
| Platinum group metal total content (both electrodes) | g/kW (rated) | 0.19 | 0.125 | 0.125 |
| Platinum group metal (pgm) total loading | mg PGM/$cm^2$ | 0.15 | 0.125 | 0.125 |
| Loss in initial catalytic activity | % mass activity loss | 48 | <40 | <40 |
| Electro catalyst support stability | % mass activity loss | < 10 | <10 | <10 |
| Mass activity | A/$mg_{Pt}$ at 900 $mV_{IR-free}$ | 0.24 | 0 | 0 |
| Non-Pt catalyst activity per volume of supported catalyst | A/$cm^3$ at 800 $mV_{IR-free}$ | 60 | 300 | 300 |

Table 2. 3 Technical targets of membrane.

| Characteristic | Units | 2011 Status | 2017 Targets | 2020 Targets |
|---|---|---|---|---|
| Maximum oxygen cross-over | mA/cm$^2$ | <1 | 2 | 2 |
| Maximum hydrogen cross-over | mA/cm$^2$ | <1.8 | 2 | 2 |
| Area specific proton resistance at: | | | | |
| Maximum operating temperature and water partial pressure from 40-80 kPa | Ohm cm$^2$ | 0.023 (40 kPa) 0.012 (80 kPa) | 0.02 | 0.02 |
| 80 °C and water partial pressures from 25-45 kPa | Ohm cm$^2$ | 0.017 (25 kPa) 0.006 (44kPa) | 0.02 | 0.02 |
| 30 °C and water partial pressures up to 4 kPa | Ohm cm$^2$ | 0.02 (3.8 kPa) | 0.03 | 0.03 |
| -20 °C | Ohm cm$^2$ | 0.1 | 0.2 | 0.2 |
| Operating temperature | °C | < 120 | $\leq$ 120 | $\leq$ 120 |
| Minimum electrical resistance | Ohm cm$^2$ | - | 1,000 | 1,000 |
| Cost | $/m$^2$ | - | 20 | 20 |

Table 2. 4 Technical targets of bipolar plate.

| Characteristic | Units | 2011 Status | 2017 Targets | 2020 Targets |
|---|---|---|---|---|
| Cost | $/kW | 10-May | 3 | 3 |
| Plate $H_2$ permeation coefficient | Std $cm^3$/(sec $cm^2$Pa) | N/A | $<1.3 \times 10^{-14}$ | $<1.3 \times 10^{-14}$ |
| Corrosion, anode | $\mu A/cm^2$ | <1 | <1 | <1 |
| Corrosion, cathode | $\mu A/cm^2$ | <1 | <1 | <1 |
| Electrical conductivity | S/cm | >100 | >100 | >100 |
| Areal specific resistance | Ohm-$cm^2$ | 0.03 | 0.02 | 0.02 |
| Flexural strength | MPa | >34 (carbon plate) | >25 | >25 |
| Forming elongation | % | 20-40 | 40 | 40 |
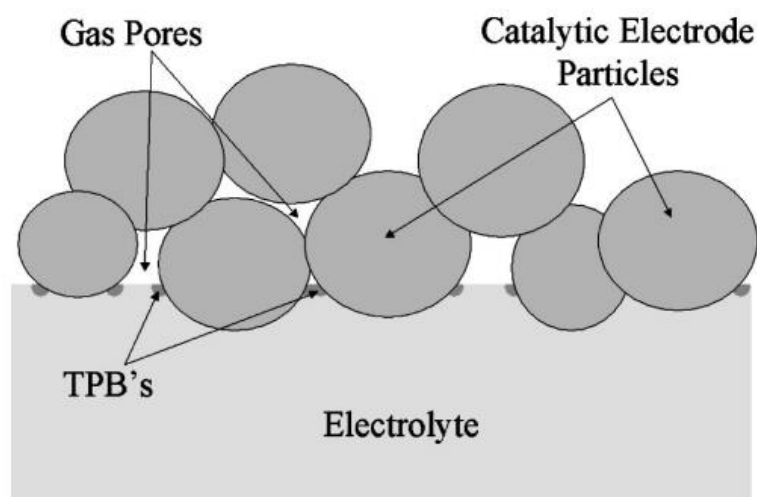


Figure 2. 4 Schematic of triple phase boundary (TPB) in PEM fuel cell [24].
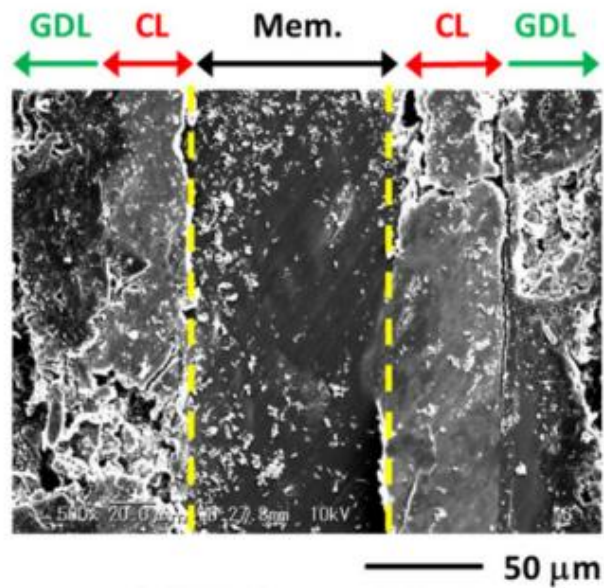
Figure 2. 5 Cross sectional SEM micrograph of membrane electrode assembly [25].

### 2.4.1 Gas diffusion layers

While approaching the center of the fuel cell, there will be the diffusion layers called gas diffusion layer (GDL). It is a gas-permeable and porous material for dispersing the reactants from the flow channel to the catalyst layer and having high electricity conductivities. The GDL is usually made from carbon fibers such as carbon cloth or carbon paper as shown in Figure 2.6.
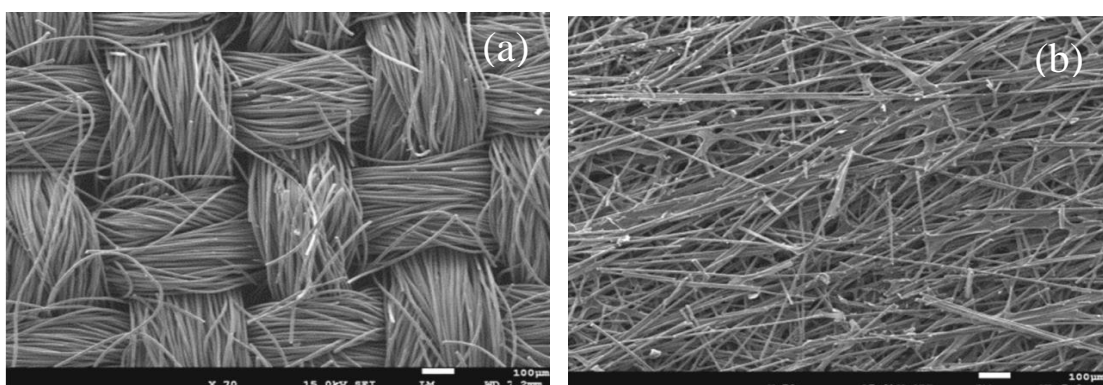


Figure 2. 6 SEM image of two different types of GDL; (a) carbon cloth and (b) carbon paper. [26]

The GDL are generally coated by hydrophobic material such as polytetrafluoroethylene (PTFE), which help to drain water presented in the electrode to the channels of the bipolar plate. In recent years, research is mainly carried out on this aspect through the addition of a micro porous layer (MPL) between the active layer and the GDL, in order to improve the water management in the heart of fuel cell and promote the electrical and thermal contact between GDL and catalyst layer [27].

*2.4.2 Catalyst layer* [5]

Many studies have been conducted to identify the best catalyst for ORR in PEM fuel cell. It is essential for reducing oxygen at the cathode and thereby maximizing the conversion of chemical energy while avoiding hydrogen peroxide formation that may degrade the utilized catalyst as well as fuel cell components. As showing in Figure 2.7, the most effective catalyst for ORR in PEM fuel cell is platinum. Therefore, the platinum is often used, in particular, in nanoparticle form.
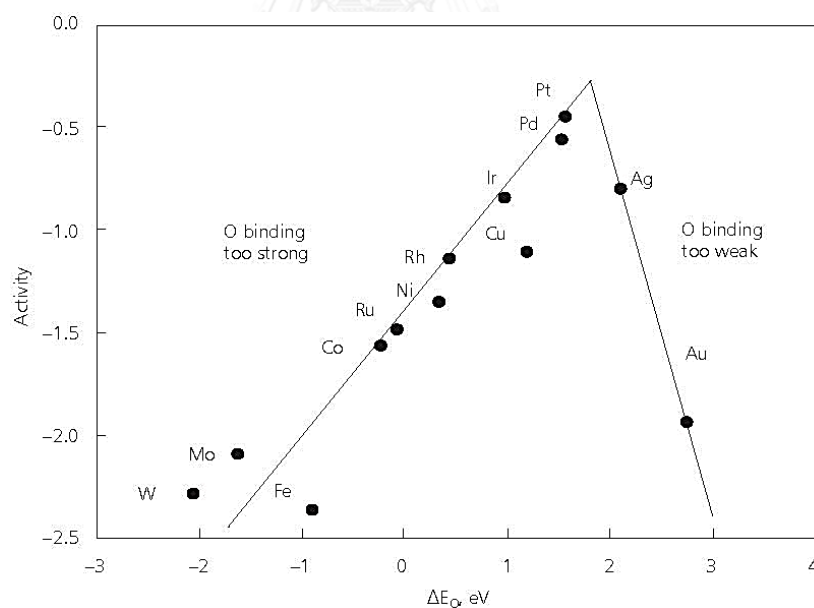
Figure 2. 7 Activity of different metals for the reduction of oxygen [28].

- Nanostructure of catalyst [5]

Nanostructure is one of the ways envisaged to reach the objectives of the Department of Energy (DOE) on catalysts for the fuel cell with increasing activity and

reducing the amount of noble metals. It allows us to get a better control of the ORR and an increase in the platinum utilization in the catalysts. More geometries and/or different compositions might lead to improve the electrocatalytic activity and the amount of noble metals used.

- Catalyst structure [5]

The activity of the catalyst in the ORR also depends on the structure of the catalyst. This kind of reaction is so-called the structure-sensitive reaction. It has been reported that the ORR are more active on the (111) and (100) crystal facets of Pt catalyst [29]. The proper structure of platinum suit for ORR is the cubo-octahedral structure (COS) as shown in Figure 2.8, which will feature a platinum structure with crystal planes (crystallographic faces) form [111] of 8 plane and [100] of 6 planes, each plane are welded together by atoms at the corners and the edges. The distribution of crystal planes can be displayed in two ways.

1. The distribution compared to the number of atoms inside. This is called the mass averaged distribution (MAD) which can be calculated from Eq. (2.26),

$$MAD(100) = \frac{N(100)}{N(t)} \tag{2.26}$$

where $N(t)$ shows the number of atoms inside the particles and $N(100)$ shows the number of atomic planes is [100].

2. The distribution compared to the number of atoms at the surface. This is called the surface-averaged distribution (SAD). It can be calculated from Eq. (2.27), where $N(s)$ shows the number of atoms on the surface of the particle itself.

$$SAD(100) = \frac{N(100)}{N(s)} \tag{2.27}$$
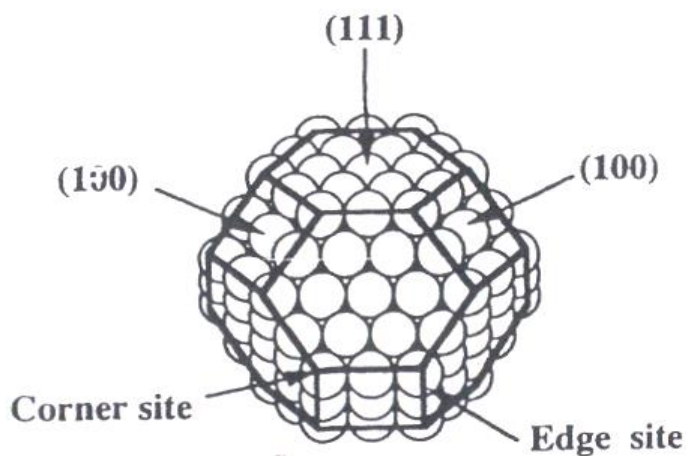
Figure 2. 8 Structural features of cubo-octahedral structure of platinum [5].

Figure 2.9 shows the dispersion trend of MAD and SAD as a function of particle size. It shows that the platinum with particle size of 2 to 3 nm is consisted of the most of a crystalline atomic planes [111] and [100] or structure of cubo octahedron (Figure 2.9(a)). In case of SAD (Figure 2.9(b)), the SAD[111] and SAD[100] dramatically increased with an increase in particle size in the range of 1-10 nm. The increasing SAD can suggest to the increasing of an active site. Then, the size of the platinum particle which is suitable for ORR is about 2-3 nm.
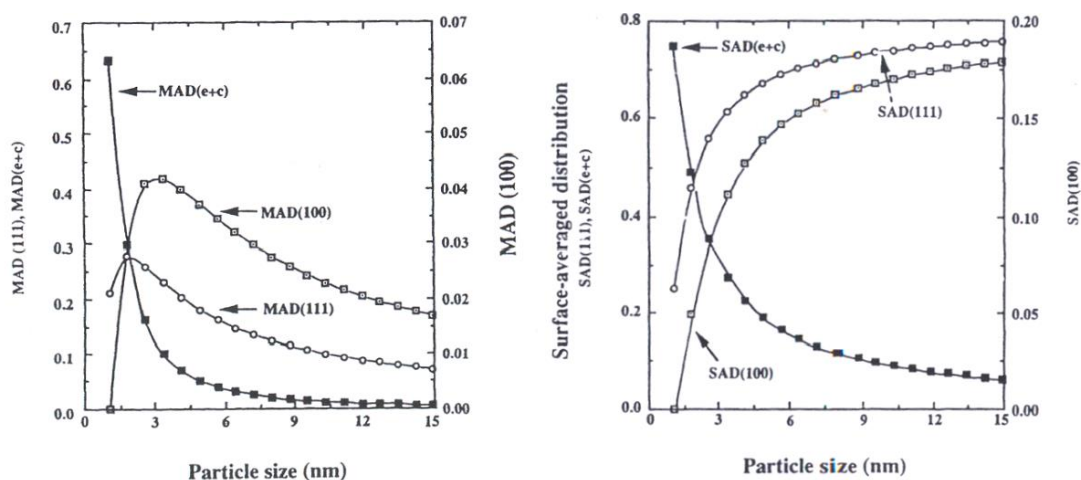


Figure 2. 9 (a) Average mass distribution, and (b) Distribution by the average surface [5].

*2.4.3 Membrane* [19]

Membrane is the most important component of PEM fuel cell because it allows the motion of the ion species from anode to cathode. It looks like a sheet of clear plastic, fabricated by a polymer. The main compound of a Nafion® membrane is sulfonated fluoro - Roberto polymer (sulphonated fluoropolymers) or fluoroethylene. The structure of Nafion membrane is represented in Figure 2.10.
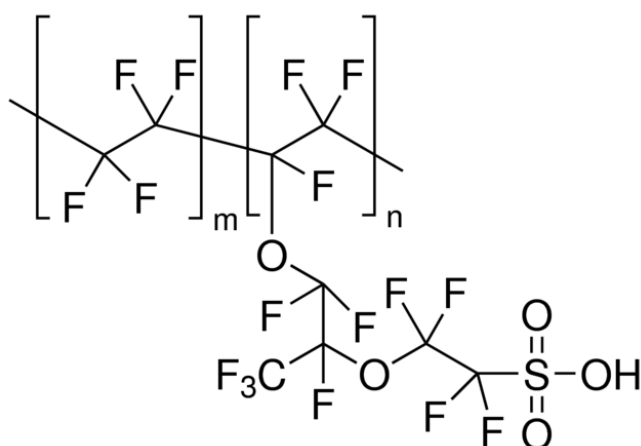


Figure 2. 10 Nafion® membrane structure [30].

*2.4.4 Bipolar plate*

It is designed to enable the delivery of reagents to the diffusion layers. Therefore, it is necessary to be a waterproof to prevent the leakage of gases to the outside. It can work as a current collector or the neighboring cell in the case of a stack, enable the heat dissipation generated by the reaction. Finally, it should have a high mechanical integrity for the cell. The popular materials used for fabricate bipolar plate are graphite or metals (stainless steel type aluminum, titanium or nickel). Both materials are the good electronic and thermal conductive, and can be machined to the route of the supply channels. Although, graphite is less economy than metal, it is more resist to the corrosion.

**2.5 ORR mechanism [5]**

The PEM fuel cells is usually operated at low working temperature. This causes an excess voltage (overpotential) for the ORR at the cathode side. The catalytic reduction of

oxygen at the cathode is generally slower than the HOR at anode side. Therefore, the performance of the fuel cell is controlled by the reaction rate of ORR at cathode side. The kinetics and reaction mechanism of ORR are depending on various variables such as type of catalyst, operating condition, and type of charge carrier substance.

The reduction of oxygen can be divided into two pathways. The first pathway is the 4-electron pathway which directly reduce oxygen to a hydroxide ions ($OH^-$) or water, as shown in Eqs. (2.28) and (2.29). The intermediate peroxide are adsorbed on the surface, but do not change to peroxide in solution. This pathway can also occur on more electrochemical catalyst such as platinum, noble metal palladium or silver metal oxides.

In alkaline media
$$O_2 + 2H_2O + 4e^- \longrightarrow 4OH^- \qquad E_0 = 0.401\,V/NHE \qquad (2.28)$$

In acid media
$$O_2 + 4H^+ + 4e^- \longrightarrow 2H_2O \qquad E_0 = 1.229\,V/NHE \qquad (2.29)$$

The second pathway is the 2-electron or peroxide pathway, as demonstrated as Eqs. (2.30) to (2.35).

In alkaline media
$$O_2 + H_2O + 2e^- \longrightarrow HO_2^- + OH^- \qquad E_0 = -0.065\,V/NHE \quad (2.30)$$
$$HO_2^- + H_2O + 2e^- \longrightarrow 3OH^- \qquad E_0 = 0.867\,V/NHE \quad (2.31)$$
$$2HO_2^- \longrightarrow 2OH^- + O_2 \qquad (2.32)$$

In acid media
$$O_2 + 2H^+ + 2e^- \longrightarrow H_2O_2 \qquad E_0 = 0.67\,V/NHE \qquad (2.33)$$
$$H_2O_2 + 2H^+ + 2e^- \longrightarrow 2H_2O \qquad E_0 = 1.77\,V/NHE \qquad (2.34)$$
$$H_2O_2 \longrightarrow H_2O + \frac{1}{2}O_2 \qquad (2.35)$$

The peroxide formation is generally undesirable in the PEM fuel cell since they contain the highly aggressive radicals HO· and $HO_2$·, which can damage the vital components.

## 2.6 Pt-M alloy

To reduce the amount of the platinum used without degrading the cell's performance, catalysts type associated with platinum metal, designated as Pt-M (where M is usually a transition metal) have been developed. The idea is to partially replace the platinum metal transition of the first series which, although less stable in corrosive environments, has catalytic properties. In recent years, the $Pt_3M$ systems (M = Co, Ni, Fe) have been extensively studied. In most cases, the bimetallic Pt-M shows the catalytic performance for ORR better than platinum alone. As demonstrated in Table 2.5, the exchange current density for the HOR is greater than that of ORR, suggesting a fast reaction rate of HOR in comparison to ORR. In addition, the exchange current density of Pt-M alloy for ORR is higher than that of pure platinum [6]. This is because the composite metal (M) in PtM alloy electrocatalysts can modify the geometrical structure of the Pt metal via decreasing the Pt-Pt bond distance [7], dissolution of the more oxidizable alloying component [8], and changing the surface structure or the electronic structure by increasing the Pt d-electron vacancy [9].

Some researches reported that the nanostructure of Pt-M alloy catalyst is easy to modify to obtain some designed properties. It is possible to obtain a platinum-backbone structure, to enrich their surface platinum, and thus to optimize their performance for the ORR [9]. This is because platinum-based alloy has less strong bonds with oxygen compared with pure platinum, which can improve the catalytic performance of the ORR as shown in Figure 2.11.

Table 2. 5 Exchange current density of metal electrocatalyst for reaction in proton exchange membrane fuel cell at standard condition (300 K and 1 atm). [5]

| Reactions | Metal | $\log j_0$ | Metal | $\log j_0$ | Metal | $\log j_0$ |
|---|---|---|---|---|---|---|
| $2H^+ + 2e^- \longrightarrow H_2$ (g) | Pd | 1 | Nb | -2.8 | Au | -1.4 |
| | Pt | 0.9 | Ti | -4.2 | W | -1.9 |
| | Ir | 0.3 | Cd | -6.6 | | |
| | Ni | -1.2 | Pb | -8 | | |
| $O_2 + 4H^- + 4e^- \longrightarrow 2H_2O$ | Pt | -7 | Ir | -10 | Pt-Co | -6.23 |
| | Ni | -7.45 | PtCr | -6.01 | Pt-Ni | -6.31 |
| | Co | -6.62 | PtFe | -6.16 | | |

Thus, to promote the commercial viability of fuel cells, the development of a cost-effective, active and stable electrocatalyst is needed. A number of different Pt based electrocatalyst concepts, such as Pt monolayer electrocatalysts, Pt alloys, and de-alloyed Pt-M alloy core-shell nanoparticles, have been developed in the last decade in order to improve the catalytic activity as well as stability. Some demonstrated that platinum alloys with transition metals, such as V, Cr, Co, Ti and Ni, as well as ternary alloys, exhibit significantly higher ORR electrocatalytic activities than Pt alone [28-29, 31-33]. The search for more active and less expensive ORR electrocatalysts with better stability than Pt based electrocatalysts has led to the development of binary and ternary Pt alloys. The Pt-Co alloy has been the most extensively studied [9, 34-35]. The Pt loading in the electrocatalysts at the cathode can be reduced if Pt-Co alloys are used as electrocatalysts for the ORR since the catalytic activity of the Pt-Co alloys for the ORR, based on the mass of Pt, is higher than that of pure Pt.
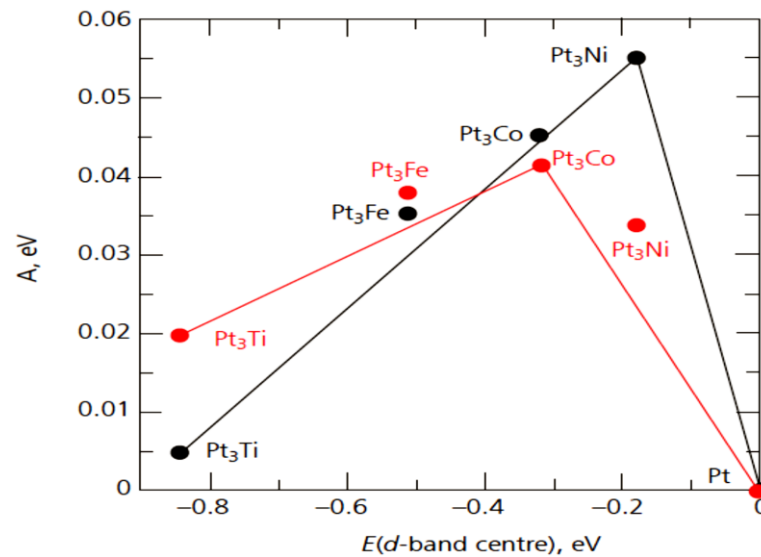
Figure 2. 11 Activity versus the experimentally measured d-band centre relative to platinum. The activity predicted from DFT simulations is shown in black, and the measured activity is shown in red. [28]

## 2.7 PEM fuel cell degradation [36]

The degradation of PEM fuel cell is generally caused by the degradation of fuel cell components such as membrane, catalyst, flow field plate, etc., or the presence of impurity in reactant gas. The major failure modes of PEM fuel cell component are summarized in Table 2.6.

### 2.7.1 Membrane degradation

The degradation of membrane can be divided into three types: mechanical degradation, thermal degradation, and chemical/electrochemical degradation.

- The mechanical degradation includes membrane cracks, tears, punctures, and pinholes due to the presence of foreign particles (*ex.* catalyst particle) or fibers introduced during the MEA fabrication process that might perforate the membrane. Besides, it can be caused by a non-uniform press pressure or inadequate humidification resulting in the fluoride loss.

- The thermal degradation occurs when the membrane becomes dehydrated due to the high-temperature operation, low humidity, and other causes, leading to the loss of proton conductivity.

- The chemical/electrochemical degradation originates from the trace metals (ex. $Ca^{2+}$, $Fe^{3+}$, $Cu^{2+}$, $Na^{2+}$, $K^+$, $Mg^{2+}$) or the radicals (ex. peroxy and hydroperoxy) resulting in the breakage of the membrane's backbone and side-chain groups and subsequent loss of mechanical strength and proton conductivity.
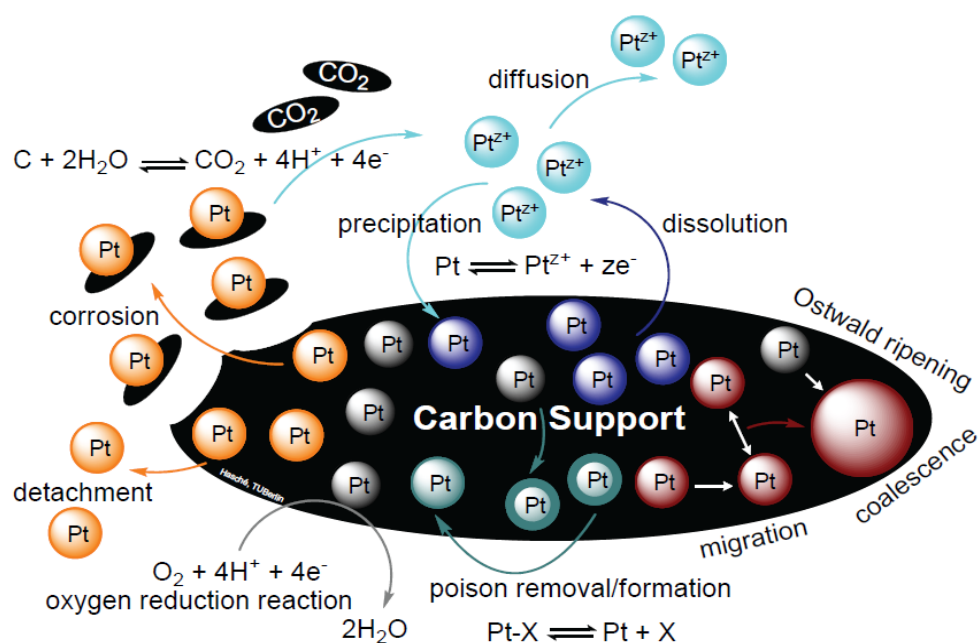


Figure 2. 12 Schematic illustrating the basic principles involved in the conceptual dissolution mechanisms for Pt in acid media and classified into Ostwald ripening and particle agglomeration [37].

Table 2. 6 Major failure modes of different components in PEM fuel cells [41]

| Component | Failure mode | Causes |
|---|---|---|
| Membrane | Mechanical degradation | Mechanical stress due to non-uniform press pressure, inadequate humidification |
|  | Thermal degradation | Thermal stress; thermal cycles |
|  | Chemical/electrochemical degradation | Contamination; radical attack |
| GDL | Decrease in mass transport | Degradation of backing material |
|  | Decrease in water management ability | Mechanical stress; Change in the hydrophobicity of materials |
|  | Conductivity loss | Corrosion |
| Catalyst/ catalyst layer | Loss of activation | Sintering or dealloying of electrocatalyst |
|  | Conductivity loss | Corrosion of electrocatalyst support |
|  | Decrease in mass transport rate of reactants |  |
|  | Loss of reformate tolerance | Contamination; radical attack |
|  | Decrease in water management ability | Change in hydrophobicity of materials to Nafion or PTFE dissolution |
| Bipolar plate | Conductivity loss | Corrosion; oxidation |
|  | Fracture/deformation |  |
| Sealing gasket | Mechanical failure | Corrosion; mechanical stress |

*2.7.2 Catalyst degradation*

The loss of PEM fuel cell stability has been explained by the loss of active on the surface area due in part to various factors including the dissolution of catalyst, catalyst growth, and carbon corrosion [38-39] as shown in Figure 2.12.

- Electrocatalyst dissolution [40-41 - 48]

The oxide species on the surface of Pt is important not only to facilitate the understanding of the kinetics of the ORR but also the dissolution of Pt. The Pt can match with oxygen and dissolution into an electrolyte because PtO is a mobile species and capable for moving to energetically preferring sites, that may result in more bare Pt being exposed to the electrolyte on the surface leading to facile dissolution. Figure 2.13 illustrates the experimental results of oxide growth and hypothesis. The dissolution of Pt can be classified into three potential ranges. The first range occurs during the potential of 0.85-1.15 V/SHE, Pt is not completely passivated with oxides. The second range occurs during the potential of 1.15-1.2 V/SHE [49], the surface is still not covered with a monolayer of oxide due to the place exchange mechanism. The last range occurs at high potential of 1.3-1.5 V/SHE, the surface is completely passivated with PtO and continues to dissolve at a lower rate.

- Crystallite growth

Many previous works reported on the crystallite growth of the metals on the supports. The mechanisms have been proposed for metal transport on the surface of the supports as shown in Figure 2.12. The small catalyst particles may migrate on the surface of the support in a manner similar to Brownian motion and collision coalesce with larger metal particles leading to particle growth. Besides, the particles may evaporate or diffuse as adatoms on the support surface and condense on larger ones similar to Ostwald ripening (dissolution-diffusion-re-deposition) in solutions.
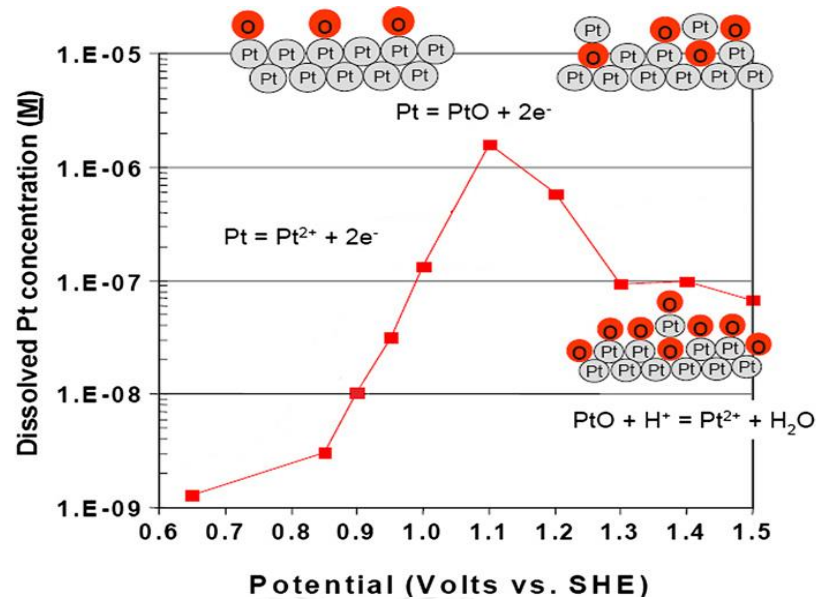
Figure 2. 13 Measured equilibrium concentration of Pt wire in 0.57 M perchloric acid at 23 °C [36].

- Carbon corrosion

The carbon black has high attractive for use as catalyst support because it has low cost, high surface area for dispersing the active species, and easy to modify the porous structure [38]. However, the carbon black can be oxidized to carbon dioxide ($CO_2$) and carbon monoxide (CO) at the potential higher than 0.2 V vs SHE, according to Eqs. (2.36) or (2.37);

$$C_{(s)} + 2H_2O \rightarrow CO_2 + 4H^+ + 4e^- \tag{2.36}$$

$$C_{(s)} + 2H_2O \rightarrow CO + 2H^+ + 2e^- \tag{2.37}$$
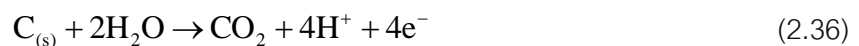
Some of the factors influencing the carbon corrosion are:

i) The carbon structure: some kind of carbon black such as Vulcan has an amorphous structure which could result to different corrosion kinetic rates [39].

ii) Oxide coverage and the presence of water can increase the oxidation of carbon to $CO_2$ [5].

iii)     The active species can speed up the carbon corrosion [40].

The all of major failures were summarized in Table 2.6.

*2.7.3 Gas diffusion layer degradation*

The degradation in this part causes by carbon oxidation, PTFE decomposition, and mechanical degradation as a result of compression, causing the loss of hydrophobicity and GDL conductivity.

## 2.8 Metal oxide

Recently, the metal oxide such as $SiO_2$, $CeO_2$, $ZrO_2$ and $TiO_2$ were introduced to a Pt/C catalyst in order to reduce the oxygen adsorption energy, the catalyst sintering and the corrosion of catalyst for PEM fuel cells. Many studies reported that the adsorption energy of oxygen affects the ORR activity in PEM fuel cell and the $5d$ transition metals are interested to use as the alloy with Pt or the catalyst for ORR in PEM fuel cell. Since, the increased of $5d$ vacancies on the catalyst surface induces an increasing link with the oxygen $2p$ states [42-43]. This leads to the decreased bond strength of the O-O bonds [42].  Figure 2.14 showed that the $5d$ metal had the lower oxygen adsorption energy than $3d$ and $4d$ metals. Then, the $5d$ metal such as Ti, Mo, and Ce become the interesting metal to improve ORR activity and stability of Pt or Pt-based catalyst in PEM fuel cell.
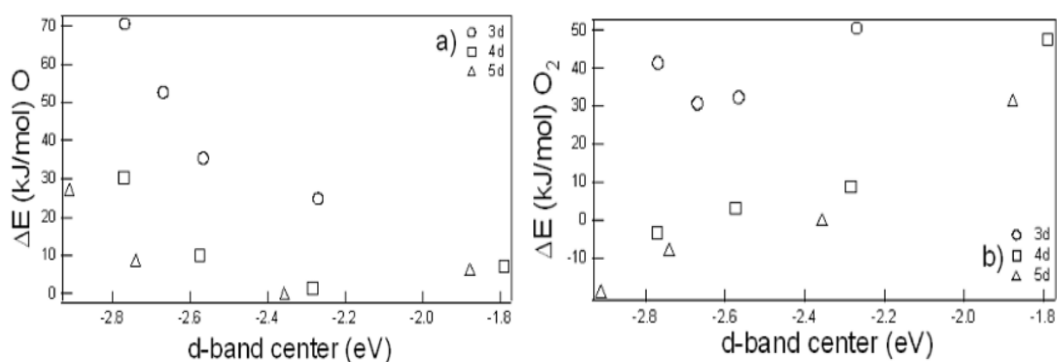


Figure 2. 14 (a) O and (b) $O_2$ adsorption energies as a function of d-band center. [44]

*2.8.1 Titanium dioxide* [45-46]

The titanium compounds are widely used in many fields because it has useful physical properties such as high refractive index and dielectric constant, high chemical stability and biocompatibility. Then, titanium dioxide ($TiO_2$) is involved in a wide range of industrial processes.

- Structural properties

$TiO_2$ is usually found in three different phases including rutile, anatase and brookite as shown in Figure 2.15. The transformations reversibility of anatase and brookite phases to rutile phase is the last phase and is the stable phase. The phase transformation of anatase to rutile occurs at $610 \pm 10 \degree$ C. Each crystallographic form consists of octahedral $TiO_6$ or each $Ti^{4+}$ anion is surrounded by an octahedron of six $O^{2-}$ cations. According to the structure, Ti-O and O-O distances are different and Ti-O apical bond and equatorial distances are slightly different as shown in Table 2.7. The rutile structure is based on body-centred tetragonal unit which shares two edges of the octahedral Ti atom with other octahedral of oxygen atom. For anatase, the octahedral shares four edges and the four fold axis. They form the eight faced tetragonal double pyramids. Finally, the structure of brookite is orthorhombic. At the center, a titanium ion is surrounded by oxygen ions at each of the six vertices and shared three edges with adjoining octahedral. Each octahedral shares three edges with closed other octahedral to create an orthorhombic structure. Brookite is often discovered compared to anatase and rutile, but it has been studied to be a photocatalyst [47].
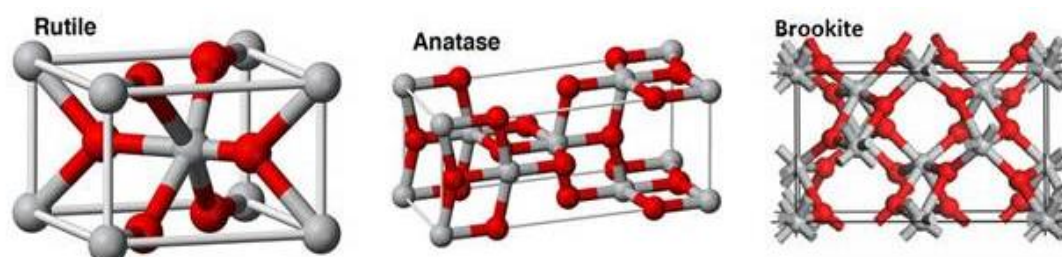


Figure 2. 15 $TiO_2$ structure [48].

In the acid electrolyte $TiO_2$ can dissolve into the solution and form the $Ti^{3+}$ ions [31], according the following reactions:

$$TiO_2+4H^+ \longrightarrow Ti^{4+}+2H_2O \tag{2.38}$$

Equation mention above is consisted of two elementary steps. First, after the protecting $TiO_2$ layer is dissolved from the electrode into acid electrolyte, the active state of titanium is promoted and $Ti^{3+}$ ions are created as displayed in Eq. (2.39). When hydrogen evolution occurs, the $Ti^{3+}$ is oxidized and Ti(IV) species, which is colorless, are created (Eq. (2.40)) [49]:

$$Ti+3H^+ \longrightarrow Ti^{3+}+3H_{ads} \tag{2.39}$$
$$4H^++4Ti^{3+}+ O_2 \longrightarrow 4Ti^{4+}+2H_2O \tag{2.40}$$

Table 2. 7 Physical property of $TiO_2$ [50]

| Property | Rutile | Anatase | Brookite |
|---|---|---|---|
| Form weight | 79.89 | 79.89 | 79.89 |
| Molar volume | 18.693 | 20.156 | 19.377 |
| Density | 4.2743 | 3.895 | 4.123 |
| Crystal system | Tet | Tet | Orth |
| Unit cell | | | |
| a (Å) | 4.5845 | 3.7842 | 9.184 |
| b (Å) | 5.447 | 5.447 | 5.447 |
| c (Å) | 2.9533 | 9.5146 | 5.145 |
| Cell volume | 62.07 | 136.25 | 257.38 |
| Molar volume | 18.693 | 20.156 | 19.377 |
| Density | 4.2743 | 3.895 | 4.123 |

*2.8.2 Molybdenum dioxide*[51]

Molybdenum is wildly used as alloying element in steel technology to improve the corrosion resistance. Although, it has many oxidation states, the stable states are Mo (IV) and Mo (VI). The reduction of $MoO_2$ is expressed in Equation (2.41)

$$MoO_2 + 4H^+ + 4e^- \rightarrow Mo + 4H_2O \qquad (2.41)$$

The crystal defects can shear planes compose nucleation sites for the formation and growth of $MoO_2$ since the lattice oxide is consisting of $MoO_6$ octahedron connected by edges (deformed rutile structure) as shown in Figure 2.16. Under low hydrogen pressure, the direct formation is observed of $MoO_2$ [52]. Unlike trioxide, a state density at the Fermi level is observed by UPS and XPS for the reducing oxides [53-54]. It is attributed to the $4d$ electrons molybdenum $MoO_2$ in the compound with metallic properties of its structure particular. The metallic character dioxides $MO_2$ (M = Mo, W) has been demonstrated by UPS high resolution analyzes [55]. The metal-metal bonding doubles band $4d$ conduction into two components corresponding to the binder states **σ** and **π** states.
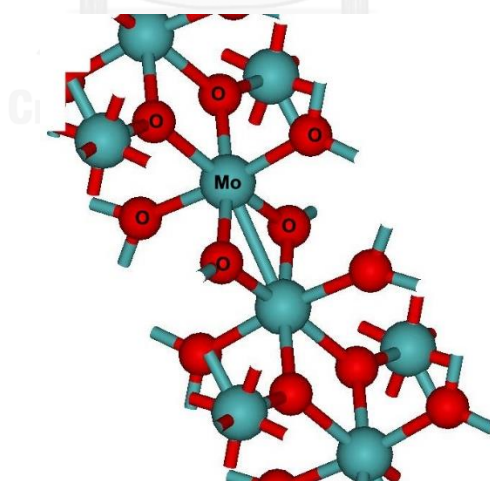


Figure 2. 16 Structure of molybdenum dioxide ($MoO_2$) [56]

The Pourbaix diagram of Mo in Mo-H$_2$O system is shown in Figure 2.17. The molybdenum is stable between two dash lines and corrodes in strongly acidic and alkaline solutions.
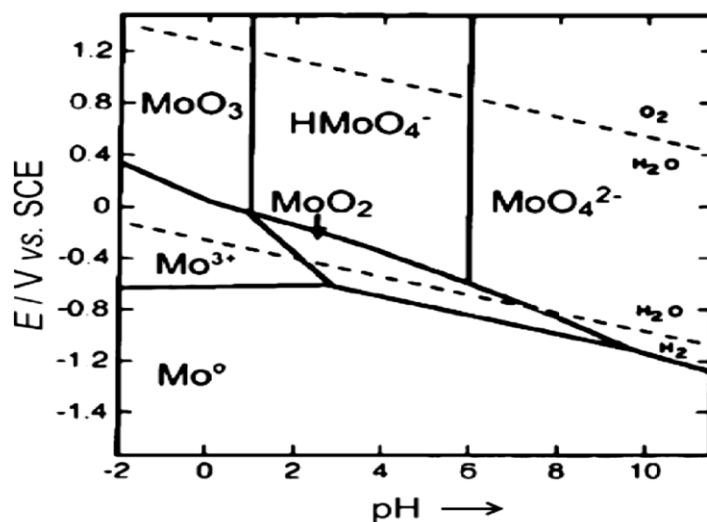


Figure 2. 17 Pourbaix diagram of Mo-H$_2$O system at 25 °C [57].

2.8.3   *Ceria oxide* [58]

Cerium is a metal belonging to the group lanthanides (rare earths). The electronic structure of cerium is [Xe] $6S^24F^15d^1$. It has two degrees of stable oxidation: + III + IV and can therefore form the two stoichiometric oxides CeO$_2$ (Ce$^{4+}$) and Ce$_2$O$_3$ (Ce$^{3+}$). CeO$_2$ can use as an oxygen donor by the following reaction.

$$2CeO_2 \leftrightarrow Ce_2O_3 + \frac{1}{2}O_2 \qquad (2.42)$$
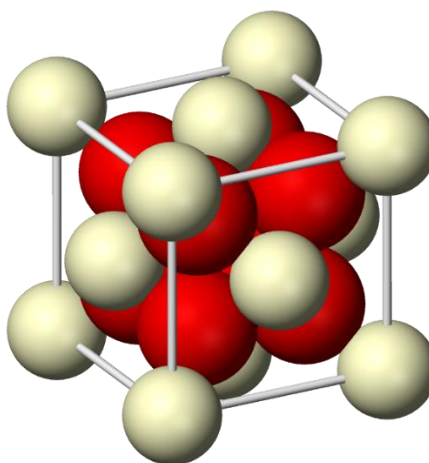


Figure 2. 18 Structure of Ceria dioxide (CeO$_2$) [59].

Cerium dioxide ($CeO_2$), also known as ceria, crystallizes in a cubic structure fluorite-type ($CaF_2$) (Figure 2.18). The structure of $CeO_2$ is a face-centered cubic structure wherein all of the tetrahedral sites is occupied by $O^{2-}$ anions. Each vertex and each face of the cubic cell are occupied by $Ce^{4+}$ cation, while each tetrahedral site is occupied by an anion $O_2$. Each $Ce^{4+}$ cation is linked to 8 $O^{2-}$ anions. The $CeO_2$ has a lattice parameter of 0.541 nm.

As demonstrated in Figure 2.19, in the range of potential and pH between dash line ① and ②, $CeO_2$ can be reduced to form $Ce^{3+}$ and give the oxygen vacancy. The decomposed oxygen from $CeO_2$ can also be reached to produce the water [60-61].
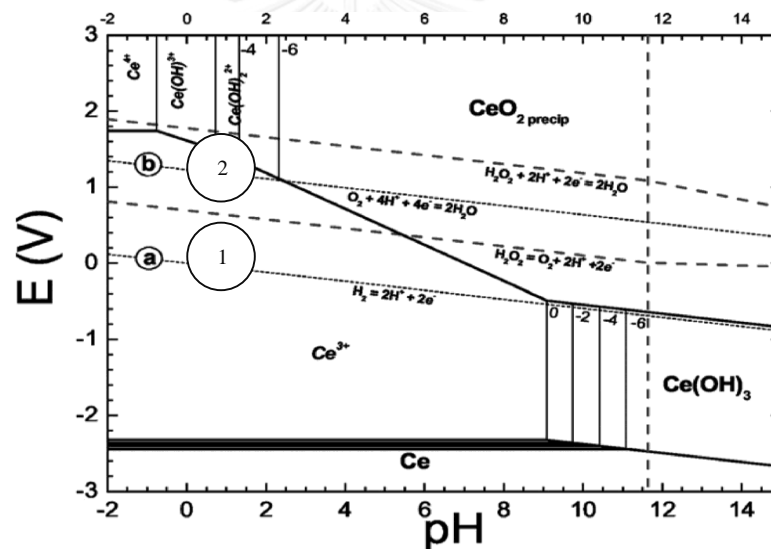
Figure 2. 19 Pourbaix diagram of Ce-$H_2$O system at 25 °C [61]

From above information, $TiO_2$, $MoO_2$, and $CeO_2$ represent their oxygen donation property and strong stability in acid environment. These are their advantages for promoting the ORR activity in PEM fuel cell.

## 2.9 Catalyst and metal preparation [62-63]

The catalyst and metal preparation method are consisted of two main stages.

1. Impregnation of the active species onto the supports by adsorption, impregnation, drying and precipitation

2. Removal of unwanted elements to keep only a catalyst

### 2.9.1 Impregnation method

The impregnation is a simple method widely used for metal preparation. The steps of impregnation are shown in Figure 2.20. It is consisted by mixing a solution of the active phase species precursor - mainly nitrates and metal acetates, as well as nanoparticles colloidal, previously prepared, stabilized by surfactants - and a carrier. The dissolved metal ions or colloids stabilized penetrate the pores of the support in the impregnation step. After the impregnation step performed, reducing, drying, and calcining are necessary to obtain the final catalyst.
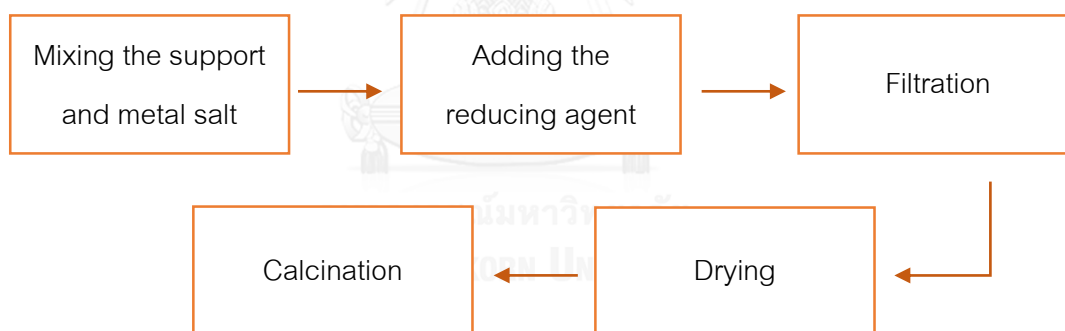


Figure 2. 20 Process steps of impregnation method.

### 2.9.2 Sol gel method

It is a simple process for the synthesis of many metals and ceramics. It is consisted of a hydrolysis of a metal precursor and followed by condensation. A colloidal suspension is then formed and then observed a transition to a solid gel after loss of solvent and full cure. After adjusting the reaction conditions (pH, solvent, addition of amines), several nanostructures can be formed. The advantages of this method are the purity of

the products, uniformity, flexibility, ease of implementation, the possibility of introducing dopant concentration and easy operation to make deposits on large and complex surfaces. The methods of micelles and inverse micelles may also be cited for the formation of nanoparticle size tightly control. The summarized sol gel process is demonstrated in Figure 2.21.
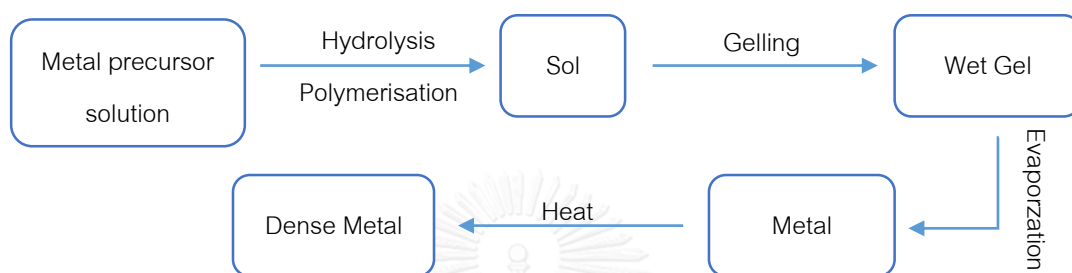


Figure 2. 21 Process steps of sol-gel method.

*2.9.3 Electrodeposition* [64]

Electrodeposition is the one of metal coating method (Figure 2.22). The thickness of the metal layer (or loading) and structure are modified by physical, chemical, and electrical parameters such as temperature, pH, metal precursor concentration, and current density. It is operated at low temperature, non-vacuum technique, and easily applied on different scales from micrometric to macroscopic areas. It also allows a good control of the amount of electrocatalyst, and can be used for depositing films or particles of metals, alloys and compound. The oxidation at anode side and the reduction and cathode side are shown in Eqs. (2.43) and (2.44), respectively.

Anode: $\quad\quad\quad\quad\quad\quad H_2O \quad\longrightarrow\quad$ ½ $O_2 + 2H^+ + 2e^-$ $\quad\quad\quad\quad\quad$ (2.43)

Cathode: $\quad\quad\quad\quad\quad Me^{Z+} + Ze^- \quad\longrightarrow\quad Me\ (s)$ $\quad\quad\quad\quad\quad\quad$ (2.44)
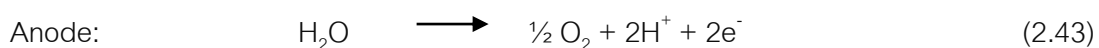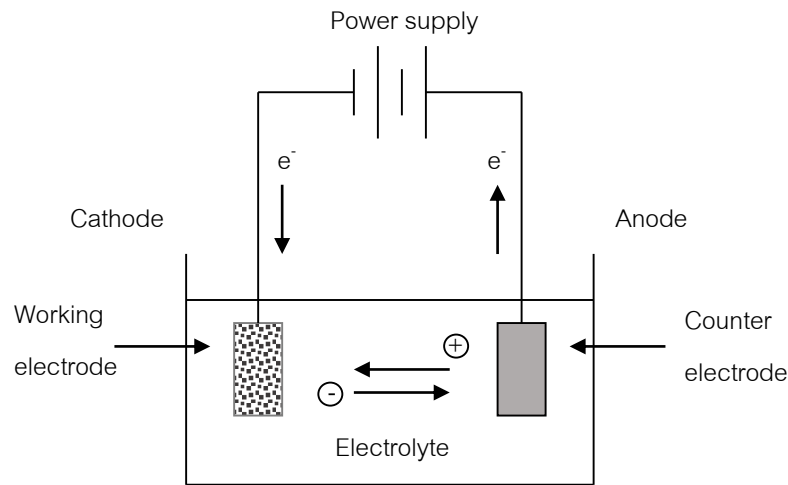
Figure 2. 22 Reaction of the electrodeposition process.

*2.9.4   Chemical vapor deposition (CVD)* [65]

The metal ion can deposit on the substrate by using chemical reaction of reactants in the gas phase. The reactant gases (precursors) are pumped into a reaction chamber (reactor). Under the suitable conditions. The products of the reaction, metal particle, deposites on the substrate. The by-products are pumped out. The significant parameters are reaction rates, gas transport, and gas diffusion. This method can be used continuously and is employed to form adherent coating on many substrates, films, and fiber, or to develop composite materials by filtration. Thus, $MO_2$ thin films with a controlled grain size, nanoparticles or nanorods are synthesized. The CVD process is consisted of several steps as shown in Figure 2.23:

    1.     Diffusion of reactant to the reaction zone

    2.     Change of reactant phase from liquid to gas phase

    3.     Transportation of reactants to the substrate surface

    4.     Chemical and/or physical adsorption

    5.     Surface reaction form the metal film

    6.     Desorption of volatile by- products

7.    Convective and diffusive transport of by-products away from the

reaction zone
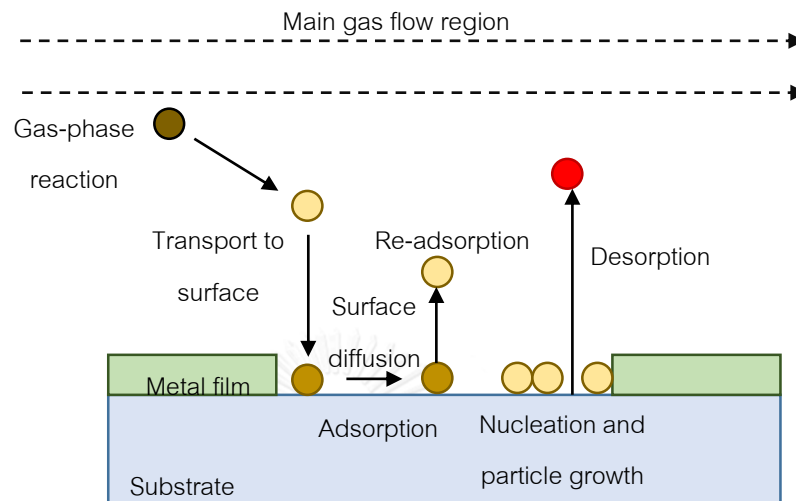


Figure 2. 23 Steps of chemical vapor deposition [66].

The film growth is determined by adsorption and reaction rates. The deposition rate is affected by the distance of the gas inlet, specification of the reaction, and radial variance. In order to improve film uniformity, it can be done by inclining substrate into gas flow direction and increasing the substrate temperature.

## 2.10 Literature Reviews

Wu et al. [31] showed that Ni can facilitate the desorption of the oxygenate species (e.g., -OH) from the surfaces of alloy particles because Ni had a lower electronegativity than Pt. This resulted in the change of the electronic properties of Pt. The cathodic current peaks associated with the reduction of platinum oxide positively shifted more than 5 mV for the $Pt_3Ni/C$ and $Pt_2Ni/C$ electrocatalysts, and about 15 mV for the PtNi/C electrocatalyst compared to the pure Pt electrocatalyst. This implied that the desorption of the oxygenate species from the surfaces of Pt alloy was easier than from the surface of pure Pt.

Toda et al. [33] reported that the electrocatalytic activity was depending on Pt-Fe alloy compositions. A dramatic reduction of the ORR overpotential was achieved by the presence of Fe in Pt structure. A maximum kinetic current density ($j_k$) of 4 mA/cm$^2$ was obtained at 50% Fe content, which was greater than that of pure Pt of around 25-fold at 0.8 V. Also, it was almost constant at less positive potentials as long as the $O_2$ was sufficiently supplied.

Takenaka et al. [35] investigated the ORR activity of $SiO_2$/Pt-Co/CB compared with Pt/C and Pt-Co/C electrocatalysts. The catalytic activity of $SiO_2$/Pt-Co/CB was high even in the region of a low cell voltage. The thickness of silica layers, which was wrapped around Pt-Co alloys, was very thin. Thus, the silica layers in the $SiO_2$/Pt-Co/CB electrocatalysts would not prevent the diffusion of oxygen molecules and protons onto Pt-Co alloy surface. For the stability test, they reported that the intensity of the peaks in the CVs for the PtCo/CB which temperature treatment at 773 K and 973 K decreased with the number of the potential cycling. The decrease in peak intensity was also observed in the CVs of $SiO_2$/Pt-Co/CB during the accelerated durability test. In contrast, the peak intensity due to Pt metal in the CVs for $SiO_2$/Pt-Co/CB did not change appreciably during the potential cycling experiments. The silica loading and the treatment temperature for $SiO_2$/Pt-Co/CB (773 K) were not high enough to improve the durability of the electrocatalyst during the potential cycling experiment. In contrast, dense silica layers in $SiO_2$/Pt-Co/CB (973 K) prevented the diffusion of Pt and/or Co species from Pt-Co alloys out of the electrocatalysts. Thus, the coverage of the Pt-Co electrocatalysts with dense silica layers further improved the durability of the electrocatalysts.

The results of different tests on the stability of PtM alloy electrocatalysts under fuel cell conditions and the consequences on the electrocatalytic activity and cell performance have been reviewed by Hector et al. [67], they pointed out that the Pt/C and Pt-Co/C electrocatalysts showed the similar stability both in acid electrolyte and in the fuel cell. A reduction on the hydrogen under potential desorption (HUPD) peak is observed for all electrocatalysts because during the CV measurements, the electrocatalysts were exposed to extremely corrosive conditions. By polarizing the electrocatalyst in acidic

media, the corrosion of the carbon support resulted in a loss of the active surface area due to particle sintering then the reduce of HUPD peak indicating an increase in the metal particle size.

A contradictory result was reported by Zignani et al. [68]. That is, a high loss of Pt-Co/C ORR activity and durability tests was observed in comparison to those of Pt/C. The low stability of the Pt-Co/C electrocatalyst during repetitive potential cycling was not ascribed to Co loss, but to the dissolution-redeposition of Pt, forming a surface layer of non-alloyed pure Pt. The result showed that the thermal treatment at 550 $^{\circ}$C increased the particle size for both Pt/C and Pt-Co/C electrocatalysts. The increase was 82% for Pt-Co and of 138% for Pt with respect to the as-prepared electrocatalysts. After thermal treatment, the presence of alloying increased the electrocatalyst particle size and decreased of the electrochemical surface area resulting in a low ORR activity of Pt-Co/C compared with Pt/C electrocartalyst.

Elezovic et al. [69] investigated the catalytic activity of $MoO_x$/Pt/C toward the activity of ORR. They pointed out that the presence of $MoO_x$ on platinum surface can reduce the active surface area of such electrocatalyst. The surface area of Pt particles would be decreased of about 95% and even more in the presence of the monolayer of $MoO_x$ because the $MoO_x$ can agglomerate on the surface of Pt nanoparticle. However, the presence of $MoO_x$ can increase the limiting current densities as well as the ORR catalytic activity of Pt/C electrocatalyst. This can be explained by the synergetic effects and spillover between the platinum and oxide materials.

Fugane et al. [70] pointed out that the ORR activity observed from home-made Pt/CB was almost constant during 1000 cycles test. Alternatively, the ORR activity observed from $CeO_x$/Pt/CB slightly decreased during 1,000 cycles test but the ORR activity on $CeO_x$/Pt/CB was still higher than home-made Pt/CB electroelectrocatalyst. This is because the Pt surface was covered by the amorphous cerium oxide ($Ce^{3+}$, $Ce^{4+}$) layer that can be prevented the dissolution of Pt into the acid solution during the long cycle CV experiment. Although small amount of amorphous cerium oxide ($Ce^{3+}$, $Ce^{4+}$) layer was

partially peeled off from the Pt surface during CV experiment, the loss of activity was still lower than that of Pt/C.

# CHAPTER 3

## Experimental and Characterization

### 3.1 Chemical and material

- Hexachloroplatinic acid hydrate ($H_2PtCl_6$. $6H_2O$, Sigma-Aldrich)

- Cobalt (II) chloride ($CoCl_2 \cdot 6H_2O$, Kanto Chemical)

- Sodium borohydride ($NaBH_4$, Labchem)

- Sulfuric acid (98%wt $H_2SO_4$, QReC)

- Nitric acid (65%wt $HNO_3$, QReC)

- Hydrochroric acid (37%wt HCl, Carlo Erba)

- Deionized water

- Nafion$^®$ perfluorinate resin solution (5%wt, Fluka)

- Nafion$^®$ membrane 115 (Electrochem)

- *i*-sopropanol (99.99 % $C_3H_7OH$, Fisher)

- Ethanol ($C_2H_5OH$, Merck)

- Titanium(IV) isopropoxide (97%wt $Ti(OCH(CH_3)_2)_4$, Sigma-Aldrich)

- Titanium (IV) dioxide (P25 Degussa, Sigma-Aldrich)

- Titanium (IV) dioxide ($TiO_2$, Sigma-Aldrich)

- Molybdenum (IV) oxide ($MoO_2$, Sigma-Aldrich)

- Cerium(III) nitrate hexahydrate ($Ce(NO_3)_3 \cdot 6H_2O$, Sigma-Aldrich)

- Polytetrafluoroethylene (60%wt PTFE, Sigma-Aldrich)

- Hydrogen peroxide (30%wt $H_2O_2$, Carlo Erba)

- Hydrogen gas (99.999% $H_2$, Praxair)

- Oxygen gas (99.999% $O_2$, Praxair)

- Nitrogen gas (99.99% $N_2$, Praxair)

- Carbon powder (Vulcan$^®$ XC-72, Cabot)

- Pt/C (20 %wt, ETEK)

- Carbon cloth (ETEK)

## 3.2 Laboratory instrument

- Spray gun (Crescendo, Model 175-7$^{TM}$)

- Pressure controller (Fujiyama)

- Oven (UFB 500, Memmert)

- Hot plate and stirrer (Ceramag midi, IKA)

- Compression mould (Model LP20, Laptech engineering)

- PEM single cell hardware (area 5 cm$^2$, Electrochem)

- Rotating disk electrode (Metrohm)

- Saturated calomel electrode (REF421, Radiometer)

- Ultrasonic water bath (NXPC-1505P, Koda)

## 3.3 Catalyst and MEA preparation

### 3.3.1 Treatment of the carbon support

Vulcan XC-72 was treated by mixed acid to remove the impurity before use as support. 12 M $H_2SO_4$ and 12 M $HNO_3$ were mixed at a volume ratio of 1:1. Vulcan XC-72 and mixed acid were added into a flask with the volumetric ratio of 70:30 and shaken at 120 rpm for 12 h. The treated Vulcan was filtrated and washed by de-ionized water until pH equal to de-ionized water's pH.

### 3.3.2 Membrane treatment

Nafion$^{®}$ membrane 115 was washed with 500 mL hot de-ionized water (80 °C) to clean the membrane surface. Then, it was boiled with 500 mL of 3%wt $H_2O_2$ in the shaker bath at 80 °C for 1 h to remove the organic impurity. Next, the obtained membrane was boiled again with 500 mL of 0.5M $H_2SO_4$ at 80 °C for 1 h to protonate the sulfonate site in

the membrane. Finally, the membrane was washed three times with hot de-ionized water (80 °C) and stored in de-ionized water.

3.3.3 Preparation of the PtCo/C catalyst

During the preparation of each electrocatalyst, the two elementary steps of seeding and impregnation were performed. Initially, 0.1 g of treated carbon black (Vulcan XC-72) was dispersed in 3 mL of deionized water, sonicated at 70 °C for 1 h and then the solution pH was adjusted 2 with 13.3 M HCl. The PtCo precursor was prepared by mixing the PtCo precursor 2.844 mL of 20 g/L $H_2PtCl_6 \cdot 6H_2O$ and 4.324 mL of 20 g/L $CoCl_2 \cdot 6H_2O$.

The seeding step was conducted by mixing the 0.7168 ml (10 % (v/v)) of PtCo precursor with the above carbon black slurry and sonicated at 70 °C for 30 min. The metal ions in the aqueous solution were then reduced to PtCo metal by the addition of 20 mL of 0.12 M $NaBH_4$ and sonicated for 30 min at 70 °C. The insoluble fraction was harvested by filtration and rinsed several times with de-ionized water to eliminate the excess reducing agent.

The impregnation step was performed by dispersing the obtained carbon powder covered by the seeded PtCo metal in de-ionized water, sonicating for 1 h and then adding to the remaining PtCo precursor (90 % (v/v)) solution to obtain the required electrocatalyst loading on the carbon support (30 % (w/w)). The mixture was reduced by the addition of 20 mL of 0.12 M $NaBH_4$ and sonicated for 30 min to obtain the catalyst powder, which settled out of the solution/suspension. The electrocatalyst suspension was filtered, and the filtrate was washed thoroughly with hot de-ionized water and dried for 2 h at 110 °C.

*3.3.4 Preparation of the sublayer, catalyst ink and catalyst-coated membrane*

The sublayer was prepared by mixing 0.5 mL of distilled $H_2O$ with 1.334 µL of 60 % (w/w) polytetrafluoroethylene and sonicating at room temperature (∼30 °C) for 30 min. The mixed solution was added to 1.0 mL of *i*-propanol and sonicated again at room temperature for 30 min. Next, 18.0 mg of treated carbon was added and sonicated at room temperature for 30 min to obtain the carbon ink, which was then coated onto a 2.25

X 2.25 cm carbon cloth as a gas diffusion layer (GDL) by brushing and then dried at 80 °C for 2 min to eliminate the excess solvent. The carbon ink coating was repeated as required until the sublayer loading was ~2.0 mg/ cm$^2$, and then the sublayer ink-coated GDL was dried at 300 °C for 1 h at atmospheric pressure (~101.3 kPa).

The catalyst ink was prepared by mixing 0.1 g PtCo/C catalyst powder with 0.4 mL of distilled H$_2$O and then sonicated at room temperature ($\sim$ 30 $^o$C) for 30 min. The obtained mixture was added into 0.916 mL Nafion solution sonicated at the same temperature for 1 h and then 3.2 mL of *i*-propanol was added and the solution was sonicated for 1 h.

The membrane electrode assembly (MEA), with a 5 cm$^2$ active surface area, was prepared as the catalyst-coated membrane by direct spraying with a spray gun onto the pretreated membrane (Nafion 115) at 80 $^o$C. For the cathode, the PtCo/C catalyst ink was sprayed slowly and then left at room temperature for 3-5 min to obtain a dry layer. The coating process was repeated several times to reach a catalyst loading of 0.15 mg/cm$^2$ and then dried at 80 °C for 10 min. This procedure was repeated for the anode side but using only the commercial Pt/C at a loading density of 0.15 mg/cm$^2$.

### 3.3.5 Preparation of MO$_2$ layer on the layer of PtCo/C catalyst

The commercial TiO$_2$, MoO$_2$, and prepared CeO$_2$ were used in this study. The CeO$_2$ powder was prepared by calcined Ce[NO$_3$]$_3$.6H$_2$O at 500 °C for 90 min [71].

To incorporate commercial TiO$_2$ and CeO$_2$ on catalyst layer, 6 mL of *i*-propanol was mixed with 0.4, 0.8, 1.5, 3.0 and 5.0 mg of either TiO$_2$ or CeO$_2$ and sonicate at room temperature of 15 min. For MoO$_2$ layer, the obtained MoO$_2$ weights similar to TiO$_2$ and CeO$_2$ were dispersed in 6 mL of ethanol and then sonicated at room temperature for 30 – 60 min. Sequentially, the MO$_2$ slurry was applied on PtCo/C layer by direct spray at different loadings in the range of 0.03 – 0.45 mg/cm$^2$.

For the coating of TiO$_2$ by CVD technique, the titanium tetraisopropoxide (TTIP) was used as a precursor. Initially, the 1.15 mL of 97 %(w/w) TTIP was mixed with 118.85 mL of *i*-propanol and stored in the stainless steel tank and maintained in N$_2$ atmosphere

as showed in Figure 3.1. Then, it was loaded into an evaporator and heated to 120 °C in flowing $N_2$ carrier gas at a flow rate of 267 sccm. The obtained TTIP gas are mixed with $N_2$ gas ($N_2$/TTIP), heated to 120 °C to prevent the condensation of the TTIP vapor and delivered to the reactor at a flow rate of 200 sccm. The vaporized precursor was transferred to a CVD reactor containing 2.5 x 2.5 cm carbon cloth coated sublayer as the substrate. The reactor temperature was raised from room temperature to 350 °C while its pressure was maintained at 0.26 atm. The CVD process was operated about 30 min to get the $TiO_2$ loading of 0.06 – 0.45 mg/cm$^2$.
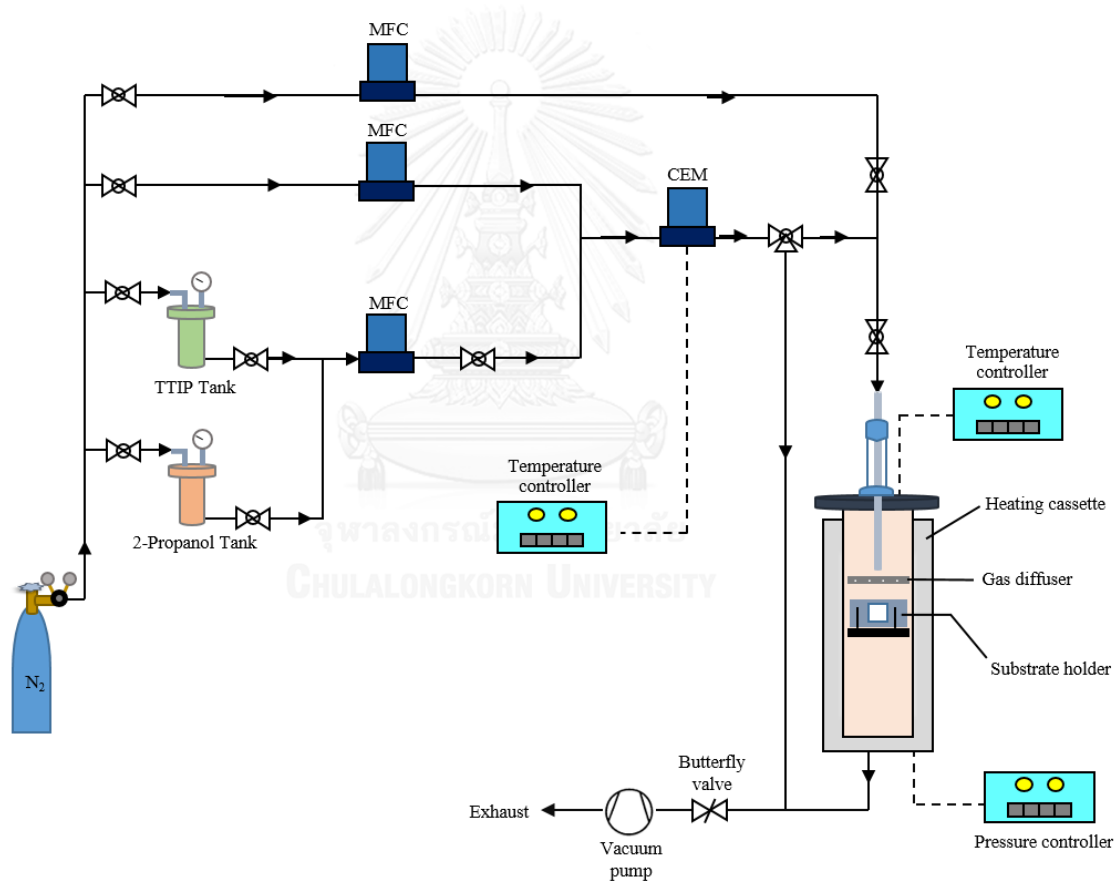


Figure 3. 1 Schematic diagram of the vertical CVD reactor.

## 3.4 Electrode physical characterization

The morphology of all as-prepared catalysts, including the evaluation of the crystalline size and $d$-spacing together with the metal content, was analyzed by X-ray diffractometer (XRD, D8 Discover-Bruker AXS) and scanning electron microscopy (SEM) with energy dispersive X-ray spectroscopy (EDX) on a JSM 6400 machine, respectively. Evaluation of the in-plane conductivity of the catalyst layer was performed with a fully-hydrated specimen using a 4-probe apparatus (RM3-AR).

## 3.5 Electrode chemical characterization

The electrochemical surface area (ESA) was estimated from the $H_2$ stripping method in $N_2$-saturated 0.5 M $H_2SO_4$. Initially, the catalyst ink prepared as described in section 3.3.4 was coated on the GDL substrate and cut as a square sheet with a dimension of $1\times1$ cm$^2$ and mounted with a home-made measuring template. The as-prepared catalyst-coated GDL, a Pt gauze and saturated calomel electrode (SCE, +0.2444 V vs SHE) were used as working-, counter- and reference electrodes, respectively. The potential was varied between -0.24 to +1.00 V vs SCE at a scan rate of 20 mV/s using a Potentiostat/Galvanostat (DEA332, Radiometer). The ESA of catalyst can be estimated from the hydrogen desorption peak according to Eq.(3.1) [43]:

$$ESA = \frac{Q_H}{[M]\times0.21}$$

(3.1)

where $Q_H$ is the charge for hydrogen desorption, 0.21 is the charge required to oxidize a monolayer of $H_2$ on bright Pt and [M] is the metal loading of Pt on the electrode.

## 3.6 ORR activity test

The ORR activity test of as-prepared electrocatalysts was carried out in two procedures including the activity tested in single PEM fuel cell under the $H_2/O_2$ environment and in $O_2$-saturated 0.5 M $H_2SO_4$ using a rotating disk electrode (RDE).

### 3.6.1 Activity test in PEM fuel cell

For the first test, the catalyst coated membrane (section 3.3) was assembled between two sheets of sublayer ink-coated GDL and pressed together by a compression mould under 65 kg/cm$^2$ in hot pressed at 137 °C for 2.5 min and cool pressed at room temperature for 2.5 min. The obtained MEA of each catalyst with a constant active surface area of 5 cm$^2$ was mounted on commercial single-cell hardware and tested in a single-cell test station (Figure 3.2). Prior to testing the cell performance, the run-in stage was performed under atmospheric pressure (~101.3 kPa) with a cell temperature of ~60 °C by feeding $H_2$ and $O_2$ at 100 sccm each (100 % humidity). The current was drawn at a high density (> 700 mA/cm$^2$) for a period of 6-12 h. Subsequently, the performance of the single cell was evaluated in the form of current-density-potential curves, monitored by an electronic load at 60 °C and ambient pressure.

### 3.6.2 Activity test in acid electrolyte

The catalyst ink prepared as described in section 3.3.4 was coated on the GDL and a 1 cm diameter circular sheet and assembled with the rotating disk substrate. Subsequently, it was connected with the Potentiostat/ Galvanostat (Metrohm) as the working electrode. A Pt gauze and SCE reference electrode were used as the counter and reference electrodes, respectively. The 0.5M $H_2SO_4$ was bubbled by $O_2$ gas for 1-2 h before test. The ORR activity of the $MO_2$-PtCo/C catalyst was determined by linear sweep voltammetry under GPES program, at 25 °C and ambient pressure. The potential was varied from -0.20 to 0.70 V vs SCE, at different rotation rates ranging from 500-2,000 rpm and a constant sweep rate of 10 mV/s.
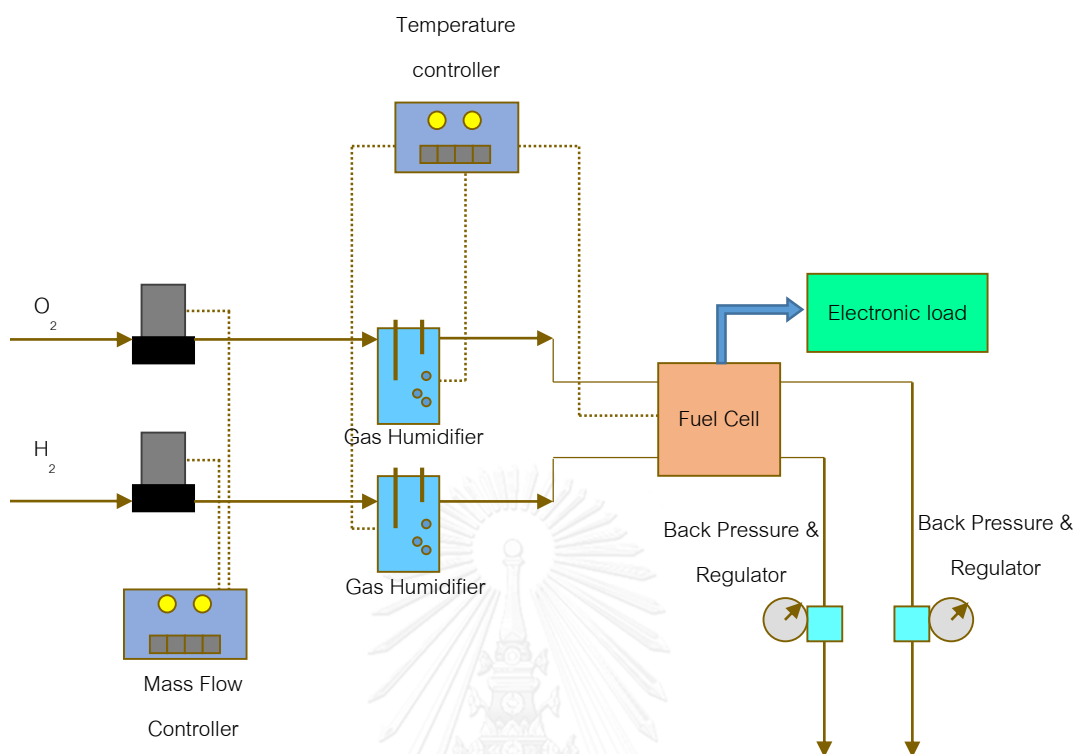
Figure 3. 2 Schematic diagram of the single cell test station.

## 3.7 Electrochemical impedance spectroscopy

The electrochemical impedance spectroscopy (EIS) was performed to measure the electrolyte resistance ($R\Omega$). The electrode preparation and the experimental set up were conducted as same as section 3.6.2. A multichannel potentiostat (Bio-Logic, France) was used and monitored with EC-Lab V10.32 software (Bio-Logic, France) using a computer. The frequency was varied in the range of 10 mHz-10 kHz at constant potential of 0.4 V vs SCE.

## 3.8 Corrosion measurement

The corrosion test was measured by using the linear sweep voltammetry technique in 0.5 M $H_2SO_4$. The electrode preparation and the experimental set up were conducted as same as section 3.6.2. The Potentiostat/Galvanostat (Metrohm) was used and monitored with GPES software using a computer. The potential was varied in the range of -0.2 - 0.8 V vs SCE with scan rate1 mV/sec [72].

## 3.9 Internal contact resistance

A 1-cm by 1.5-cm of electrode as prepared in section 3.6.2 was cut and placed between the two copper sheets (the thickness of electrode was measured by micrometer). They were pressed by bench vise at 40 $lb_f$-ft. The potential was applied through the copper sheets and varied between 0-0.5 V and collected the current data. The plot of potential and current were fitted to find the internal contact resistance by using Ohm's law as showed in Eq. 3.2.

$$V = IR \tag{3.2}$$

where $V$ is the potential (V), I is the current (A) and R is the resistance ($\Omega$).

# CHAPTER 4
## Results and Discussion

### ORR activity and stability of $MO_2$-PtCo/C catalyst in PEM fuel cell

In this work, the PtCo/C electrocatalyst is used as a candidate catalyst for improving the ORR in PEM fuel cell because it is cheaper than pure Pt/C catalyst which can reduce the amount of platinum catalyst in the cathode side of PEM fuel cell. Although the PtCo/C catalyst can increase the ORR activity, it is not stable in acid electrolyte. The corrosion of this catalyst reduces the stability of PEM fuel cell. To enhance the stability of PtCo/C catalyst, the addition of strong acid resistance metal into catalyst layer will be explored. Many metal oxides are studied and show the high sintering and corrosion resistances in acid media. In this chapter, we will evaluate the effects of different commercial metal oxides ($CeO_2$, $MoO_2$, and $TiO_2$) and their loadings on the ORR activity and stability of PtCo/C electrocatalyst. The physical characterizations, electrochemical results and activity are reported here.

## 4.1 Morphology of $MO_2$

The XRD patterns of the $CeO_2$, $MoO_2$, and $TiO_2$ are shown in Figure 4.1. The diffraction patterns of $CeO_2$ showed peaks at $2\Theta$ values of 28.59°, 33.03°, 47.31°, 56.03°, 59.18° assigned to [111], [200], [220], [311], and [222] crystalline planes, respectively, of cubic $CeO_2$. The XRD patterns of $MoO_2$ exhibits peak at 26.1°, 37.1°, 53.6° and 60.1°, corresponding respectively to the [011], [211], [022] and [031] lattice planes of the monoclinic $MoO_2$ crystal and $TiO_2$ showed the characteristic peaks at about 25.28°, 37.80° and 48.05° corresponding to the [101], [004], and [200] diffraction planes of anatase phase, respectively. Besides, the $TiO_2$ diffraction peaks also showed the peak at 27.5°, 62.3°, and 68.9°, representing the [110], [002], and [301] planes of rutile phase,

respectively. Then, it can conclude that the commercial $TiO_2$ is mixed phase between anatase and rutile. The crystalline size of $CeO_2$, $MoO_2$, and $TiO_2$ were calculated by Debye-Scherrer equation (Appendix A) and the results were shown in Table 4.1. The crystalline size of $CeO_2$, $MoO_2$, and $TiO_2$ were 44.21, 41.61, and 11.59 nm, respectively. Moreover, the SEM image (Figure 4.2) can clearly confirm the big size of $CeO_2$ and $MoO_2$ particles, while $TiO_2$ had small and uniform particle size.
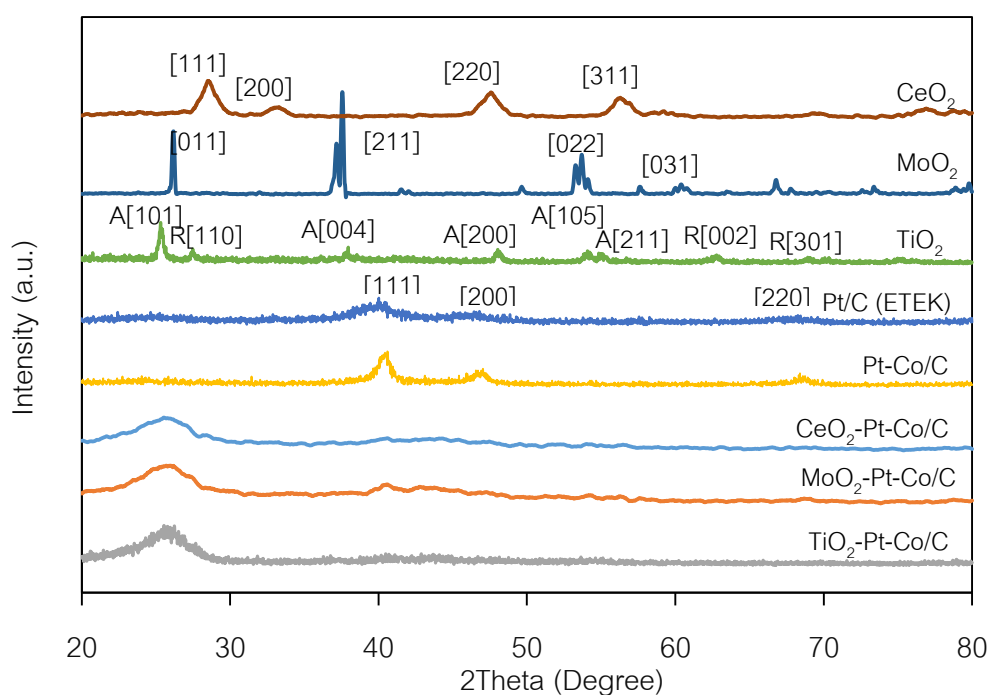


Figure 4. 1 Representative XRD patterns of $CeO_2$, $MoO_2$, $TiO_2$, commercial Pt/C.

(ETEK) and the as-prepared PtCo/C catalysts in the absence and presence of $MO_2$ at different loadings.
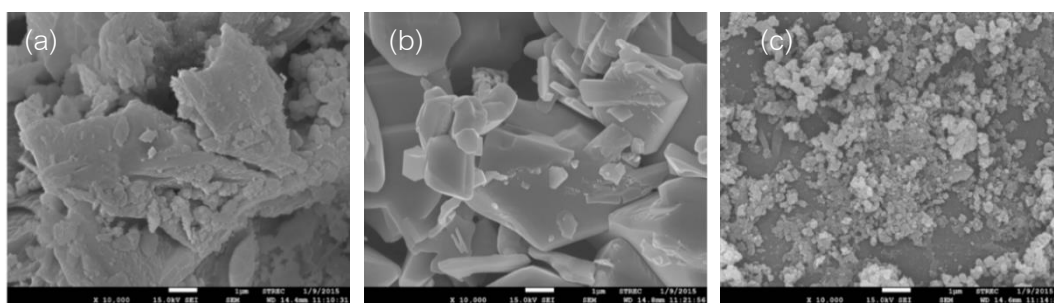
Figure 4. 2 SEM micrographs (x 10,000) of (a) $CeO_2$, (b) $MoO_2$, and (c) $TiO_2$.

## 4.2 Morphology of $MO_2$-PtCo/C electrodes

Representative XRD patterns of the commercial Pt/C (ETEK) electrocatalyst exhibited four main peaks as demonstrated in Figure 4.1. The first peak at a $2\theta$ value of about $24.67^{\circ}$ was due to the presence of the carbon support in the hexagonal structure [73]. The other three peaks are the characteristic peaks for the diffraction pattern of face-centered cubic (FCC) Pt [73], corresponding to the [111], [200] and [220] planes at a $2\theta$ of $39.67^{\circ}$, $45.80^{\circ}$ and $67.78^{\circ}$, respectively. The diffraction peak of the as-prepared PtCo/C catalyst still demonstrated the characteristic FCC crystalline Pt. However, compared with the diffraction of the bulk Pt, its diffraction peaks were shifted slightly to higher $2\theta$ values ($40.6^{\circ}$, $47.04^{\circ}$ and $68.40^{\circ}$). In addition, the $d$-spacing value for the as-prepared PtCo/C catalysts (Table 1) was smaller than that of the commercial Pt/C catalyst. Both parameters indicated the formation of a PtCo alloy due to the particle substitution of Pt by Co in the FCC structure [74].
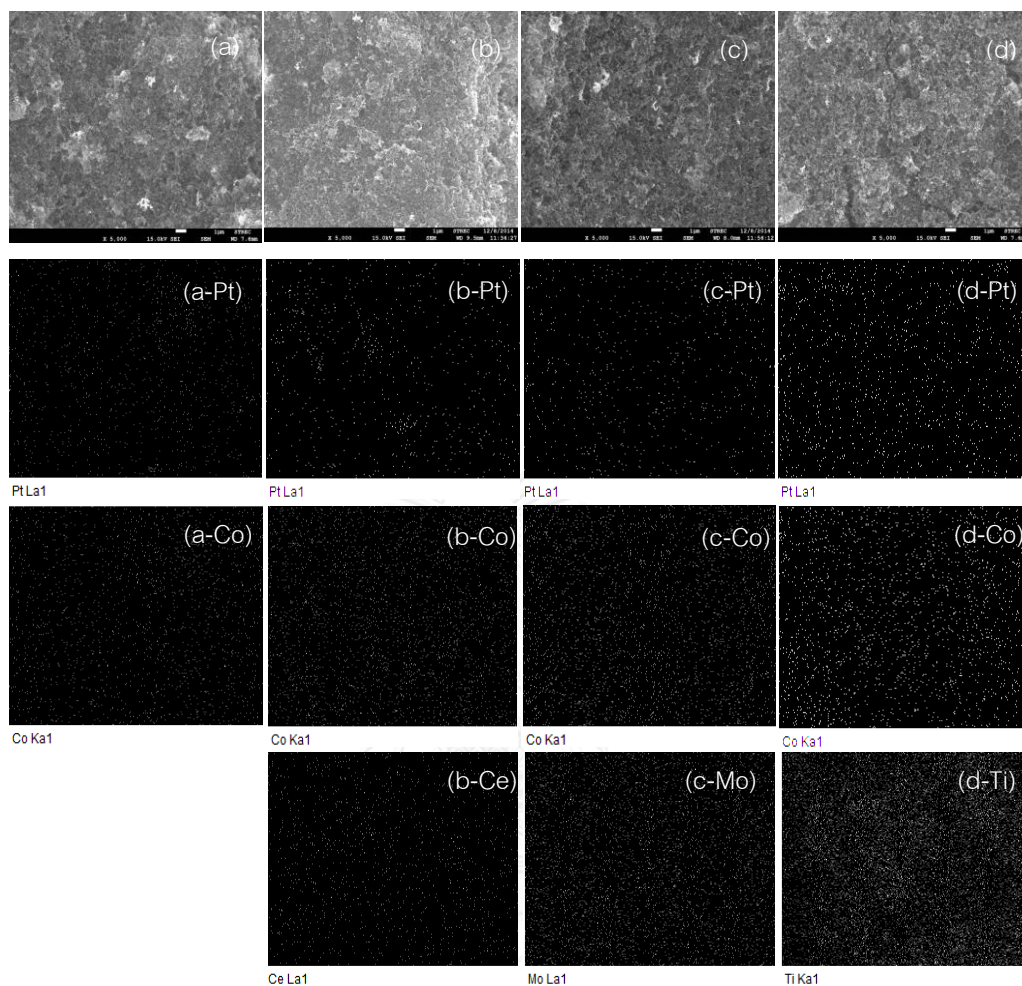
Figure 4. 3 SEM micrographs of crystalline particles (a - d), and X–ray images used to map the location of the elements dispersion of (a) PtCo/C, (b) $CeO_2$-PtCo/C, (c) $MoO_2$-PtCo/C and (d) $TiO_2$-PtCo/C catalysts.

Although no characteristic peaks of metallic Co or its respective oxides were detected in the XRD plots of the PtCo/C catalysts, their presence could not be formally excluded because they may be present in a very small amount and/or in an amorphous form.

When identical loading of metal oxides ($MO_2$) of 0.15 mg/cm$^2$ were incorporated onto the electrode surface between gas diffusion layer and PtCo/C catalyst layer, their XRD patterns also exhibited the characteristic Pt peaks of a FCC structure. The addition of $MO_2$ on PtCo/C catalyst layer led to a decrease in intensity of PtCo peaks and it cannot observe the $MO_2$ peaks, indicating a low degree of crystallinity of PtCo and $MO_2$ on GDL. Nevertheless, the $d$-spacing values of all $MO_2$-PtCo/C catalysts were still lower than that of the commercial Pt/C and were broadly similar to that of the PtCo/C catalyst, indicating that the incorporation of $MO_2$ on the surface of PtCo/C had no effect on the alloy property of the PtCo/C catalysts. By using the Debye-Scherrer equation (Appendix A), the crystalline size for the PtCo particles in the PtCo/C catalyst was determined to be 7.67 nm, which was 2.75-fold larger than that of the commercial Pt/C catalyst (Table 1). The incorporation of $MO_2$ had no significant influence on the crystalline size of PtCo/C catalysts. They deviated in the range of 7.41-7.67 nm (Table 4.1).

To confirm the presence of metal on the electrode, the EDX analysis was used. It exhibited the uniform distribution of metal particles along the GDL surface (Figure 4.3). The presence of Pt particles was slightly denser than that of Co, referring the presence of a higher quantity of Pt particles than Co. Quantitatively, the Pt:Co ratio in the PtCo/C catalyst was around 58.5: 41.5.

Table 4. 1 Morphology of the metal oxides, Pt/C- and PtCo/C-catalyst layer at different $MO_2$ types.

| Type of catalyst | $d$-spacing (nm) | Crystalline size (nm) |
|---|---|---|
| $CeO_2$ | 0.951 | 44.26 |
| $MoO_2$ | 0.519 | 41.61 |
| $TiO_2$ | 0.351 | 11.59 |
| Pt/C (ETEK) | 0.226 | 2.78 |
| PtCo/C | 0.223 | 7.67 |
| $CeO_2$-PtCo/C | 0.225 | 7.65 |
| $MoO_2$-PtCo/C | 0.222 | 7.64 |
| $TiO_2$-PtCo/C | 0.224 | 7.41 |

## 4.3 Effect of $MO_2$ types and loadings

### 4.3.1 Electrochemical property

In this part, the ESA of all $MO_2$-PtCo/C catalysts were then determined by the cyclic voltammetry (CV) under nitrogen atmosphere with different potentials in the range of -0.35 to 1.2 V/SCE at 20 mV/s. The proton adsorption/desorption on the platinum surface can be observed at potentials lower than 0.4 V (Figure 4.4(a)). As demonstrate in Figure 4.4(b), the addition of $CeO_2$ and $MoO_2$ impacted negatively. The increase of $CeO_2$ and $MoO_2$ loading resulted to the decreasing ESA, probably attributed to a large particle of $CeO_2$ and $MoO_2$ that can cover the available active area of PtCo catalyst [75-76]. However, the presence of $TiO_2$ provided both positive and negative impacts on the ESA of PtCo/C catalyst.
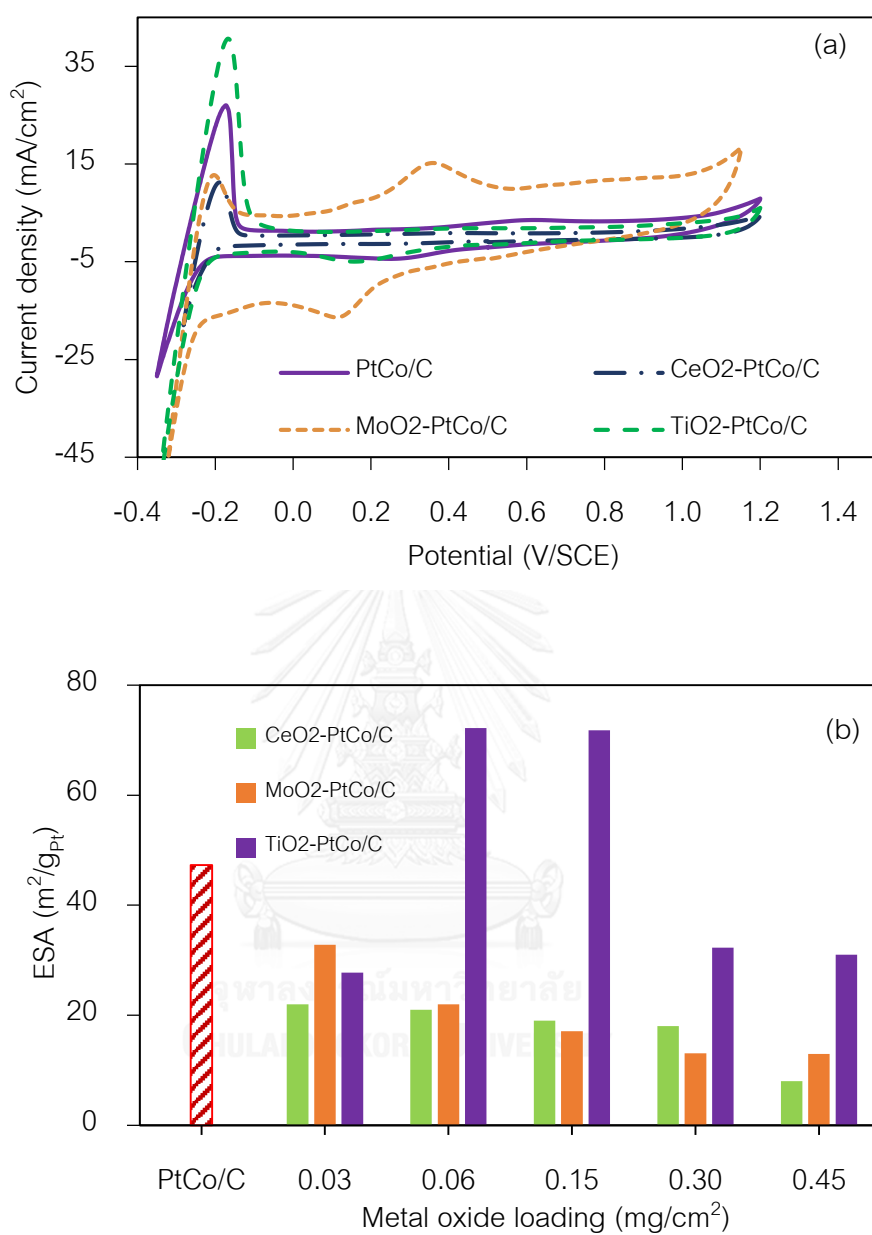
Figure 4. 4 (a) Cyclic voltammograms of $MO_2$-PtCo/C in 0.5 M $H_2SO_4$ at the scan rate of

20 mV/s and (b) The comparison of electrochemical surface area of $MO_2$-PtCo/C

electrodes with different types and loadings of $MO_2$

The increase of $TiO_2$ from 0 to 0.06 mg/cm$^2$ resulted to the increasing ESA.Further raising the $TiO_2$ loading up to 0.45 mg/cm$^2$ led to the decreasing ESA. The increasing ESA at low $TiO_2$ content might be attributed to the increase of electrode roughness. Overloading of $TiO_2$, particularly at 0.3 and 0.45 mg/cm$^2$ induced the blockage of percolating electron-conducting network in the electrode, resulting in a decreasing electronic conductivity as well as ESA.
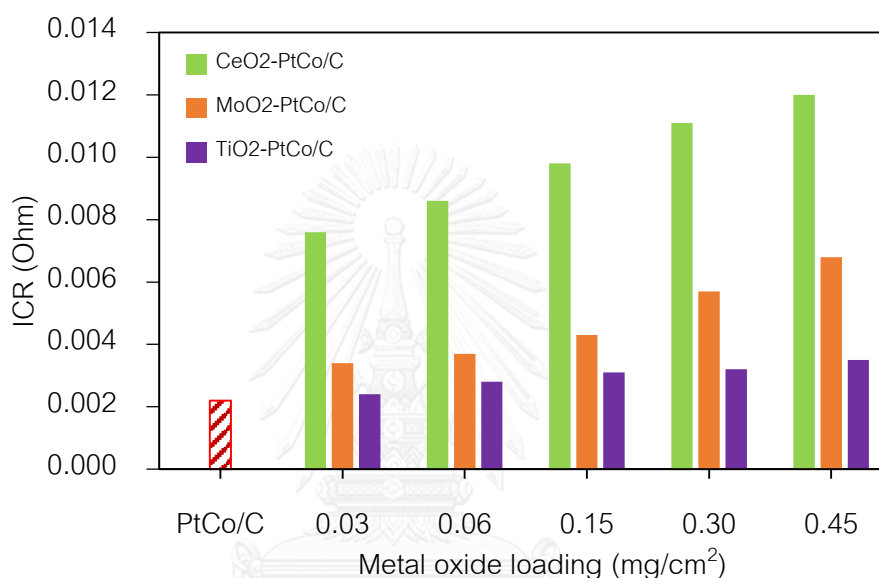


Figure 4. 5 Interfacial contact resistance for PtCo/C catalyst in the presence of different $MO_2$ loadings.

With regard to the effect of $MO_2$ type and loading on the interfacial contact resistance (ICR) of PtCo/C catalyst, as shown in Figure 4.5, it can be seen that the increase of $MO_2$ loading resulted in the increase of ICR with the order of $CeO_2$ > $MoO_2$ > $TiO_2$ because $CeO_2$ and $MoO_2$ had the large particle size and the $CeO_2$ and $MoO_2$ had the sheet or plate shape, then they can more coverage and blockage the electron transfer over the GDL and catalyst layer, that differs from $TiO_2$. The $TiO_2$ had a small particle and spherical shape, which can connect between carbon particle and had lower effect on ICR than $CeO_2$ and $MoO_2$. Moreover, the increase of $MO_2$ loading as well as the $MO_2$ thickness

also affected the increasing ICR. Furthermore, the oxygen molecule on the electrode surface will reduce the electron mobility along carbon surface and other element [69, 77-78]. Nonetheless, the proper amount of $TiO_2$ (0.06 mg/cm$^2$) could show a higher ESA and the lower ICR than other catalysts. This indicated that $TiO_2$ at loading of 0.06 mg/cm$^2$ has a high potential to promote the catalytic activity of PtCo/C catalyst.

### 4.3.2 ORR activity

The ORR activity of all $MO_2$-PtCo/C catalysts were first tested in $O_2$-saturated 0.5 M $H_2SO_4$ using RDE at rotation rates between 500-2,000 rpm during a varying potential of -0.20 to 0.70 V and a constant sweep rate of 10 mV/s. The similar pattern of the voltammogram for the ORR was obtained for all catalysts as demonstrated in Figure 4.6. The curve can be divided into three distinct regions. The first region (0.7 to 0.5 V) is a kinetics-controlled region, where the current density was not affected by the rate of mass transfer, and it is independent of the rotation rate ($\omega$). The second region (0.5 to 0.2 V) is an intermediate region of mixed control where the current is partially controlled by mass transport and partially by the kinetics of electron transfer. The current increases with $\omega$, but not as a linear function of $\omega^{1/2}$. The last region (0.2 to -0.2 V) is a diffusion-controlled region, which showed a well-defined limiting current plateau that increased linearly with $\omega^{1/2}$. The relation between the current density and the rotation rate can be expressed by the Koutecky-Levich equation (Eq.(4.1)).
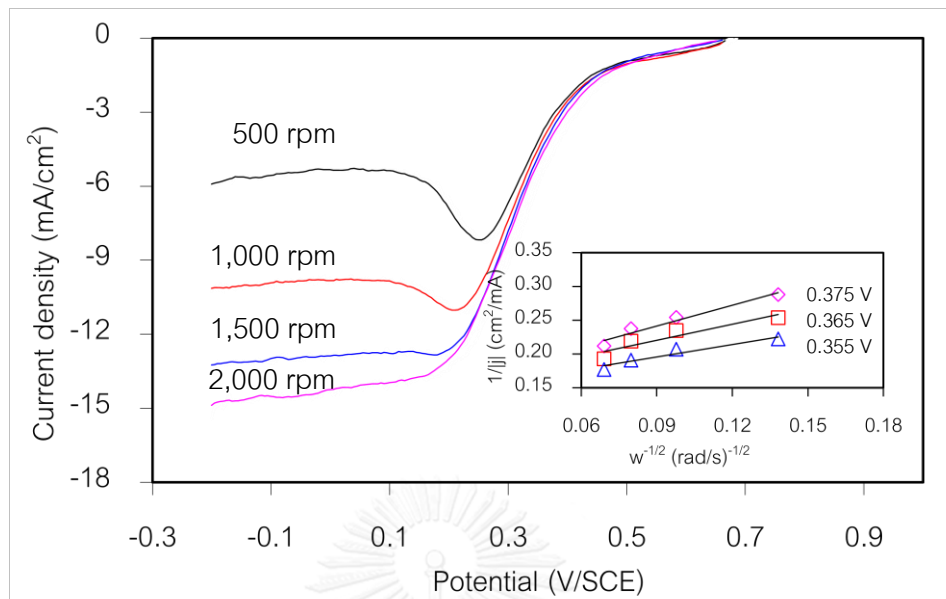
Figure 4. 6 Example plot of voltammogram for the ORR of TiO$_2$-PtCo/C catalyst in 0.5 M H$_2$SO$_4$ (O$_2$-Sat.) at scan rate of 10 mV/s.

This equation is valid for a first order process with respect to the diffusion species [79].

$$\frac{1}{j} = \frac{1}{j_k} + \frac{1}{B\omega^{1/2}}$$ (4.1)

and where $B$ is estimated by Eq. (4.2),

$$B = 0.62n_e FD^{2/3}\nu^{-1/6}C$$ (4.2)

Here, $j_k$ is the kinetic current density, $\omega$ is the rotation rate, $n_e$ is the number of involved electrons, $F$ is the Faraday's constant (96,485 C/mol), $D$ is the diffusion coefficient of oxygen in solution (1.9 × 10$^{-5}$ cm$^2$/s), $\nu$ is the kinematics viscosity (0.01 cm$^2$/s) and $C$ is the oxygen concentration in the bulk solution (1.1 × 10$^{-6}$ mol/cm$^3$).

The plot of $j^{-1}$ vs. $\omega^{-1/2}$ provided straight lines with the intercepts corresponding to the kinetic current density ($j_k$). Figure 4.7 shows the plot of kinetic current density of all MO$_2$-PtCo/C catalysts versus MO$_2$ loadings. The ORR activity or $j_k$ was found to depend on the loading of MO$_2$. The presence of CeO$_2$ and MoO$_2$ showed the low ORR activity of PtCo/C catalyst because the large size of them provided the electron blocking layer

between GDL and catalyst layer. These resulted to slow and less oxygen reduction reaction on electrodes. However, the activity of PtCo/C catalyst in presence of $TiO_2$ increased with the increase of $TiO_2$ loading of 0.03 to 0.15 $mg/cm^2$. Further, raising of $TiO_2$ loading greater than 0.15 $mg/cm^2$ decreased the $j_k$ because the high loading of $TiO_2$ could form the insulating layer onto the electrode similar to the case of $CeO_2$ and $MoO_2$. In addition, the onset potential of PtCo/C catalyst increased with the present of $MO_2$, suggesting that the ORR occurred easier when compare to the pure PtCo/C catalyst as showed in Figure 4.8. Consider the effect of $MO_2$ on the limiting current density ($j_L$) of electrodes, it was found that $j_L$ increased with presence of $MO_2$. This indicated that mass transport of $O_2$ on PtCo/C was enhanced because $MO_2$ can increase the local oxygen concentration on the catalyst surface [15, 80-81]. The $j_L$ of $MO_2$-PtCo/C with the order of $TiO_2$-PtCo/C > $MoO_2$-PtCo/C > $CeO_2$-PtCo/C > PtCo/C. The obtained $j_L$ of $MoO_2$-PtCo/C and $CeO_2$-PtCo/C were small compared to that of the $TiO_2$-PtCo/C because the $MoO_2$ and $CeO_2$ had larger particle size, higher ICR and less ESA than $TiO_2$-PtCo/C. Also from plot of $j^{-1}$ *vs.* $\omega^{-1/2}$, the number of electrons involved in the ORR on the as-prepared catalysts can be estimated. From the calculation, the number of transferred electron in the process via $MO_2$-PtCo/C catalysts were between 3.84 and 3.97 with an average value of 3.91, suggesting that the ORR reaction occurred via the four-electron pathway and the addition of $MO_2$ onto PtCo/C catalyst layer had no effect on electron pathway.
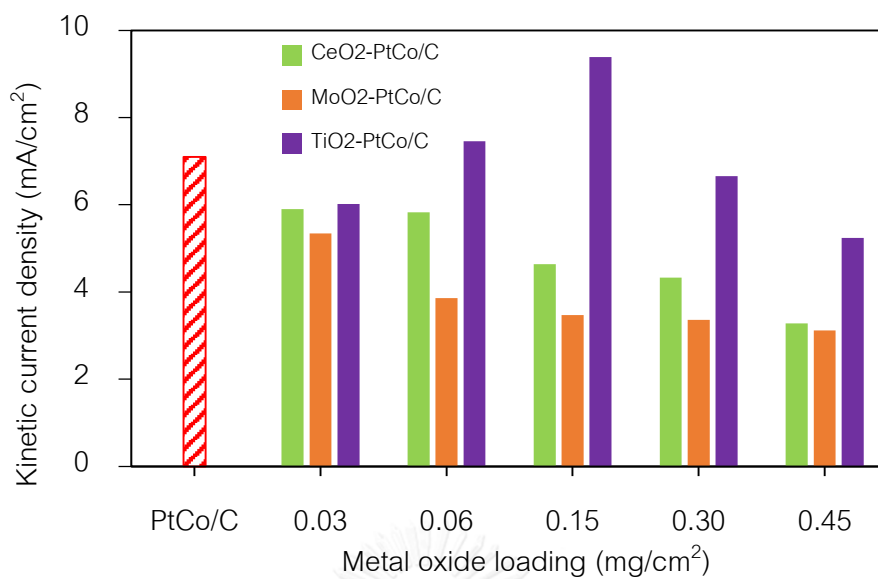
Figure 4. 7 Kinetically controlled ORR at 0.375 V versus SCE electrode for PtCo/C

catalyst in the presence of different $MO_2$ loadings.
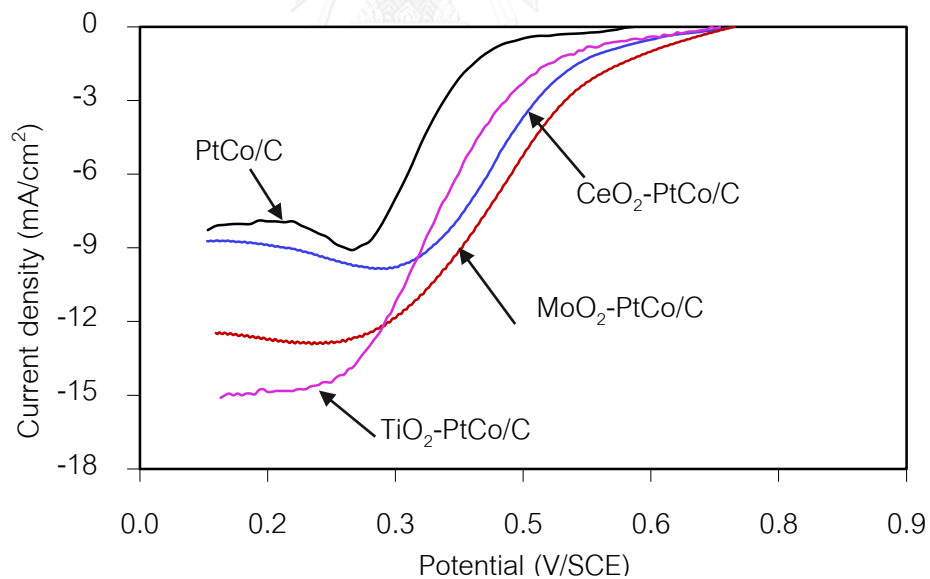


Figure 4. 8 Voltammograms of $MO_2$-PtCo/C at the same rotating speed of 2000 rpm.

### 4.3.3 ORR activity in PEM fuel cell

Besides the activity in acid solution, the activities of the as-prepared PtCo/C and MO$_2$-PtCo/C catalysts in the ORR were tested in a single PEM fuel cell at 60 $^o$C and atmospheric pressure (~101.3 kPa) under a H$_2$/O$_2$ condition. As demonstrated in Figure 4.9, the major reason for the power performance difference was the differences in ohmic resistance and mass transport resistance. The inclusion of MO$_2$ in the PtCo/C catalyst layer did not significantly affect the open circuit potential of the single cell, but significantly affected the cell performance, particularly at medium-to-high current densities.

The ORR activity of PtCo/C catalyst under the activation-controlled region or activation loss can be determined in terms of the current density at a potential of 0.9 V ($j_{0.9}$ $_V$) and under a medium-to-high region or ohmic loss, the PEM fuel cell performance was compared at 0.6 V.  The results showed that the presence of CeO$_2$ and MoO$_2$ negatively affected the ORR activity of PtCo/C catalyst and PEM fuel cell performance. Consider with the previous results, the decrease of ORR activity in PEM fuel cell is probably due to the presence of the large CeO$_2$ and MoO$_2$ size that had the negative effect on ESA of PtCo/C catalyst. However, the presence of TiO$_2$ enhanced the activity of the PtCo/C catalysts.

Nevertheless, the performance of fuel cells at 0.6 V increased as the increase of TiO$_2$ loading from 0.03 to 0.06 mg/cm$^2$ of around 1.19-fold (Table 4.2 and Figure 4.9(c)). Further increase the TiO$_2$ loading from 0.06 to 0.45 mg/cm$^2$ resulted to the decrease of cell performance by approximately 1.18-fold. This demonstrated that the presence of proper loading of TiO$_2$ can reduce the ohmic- as well as the mass transfer losses. The alternation of ohmic resistance in a medium to high current density in the presence of MO$_2$ is probably due to the changing of hydrophobic/hydrophilic property of GDL and catalyst layer. From Figure 4.10, the contact angle of CeO$_2$-PtCo/C and MoO$_2$-PtCo/C were greater than 90°, indicating that CeO$_2$ and MoO$_2$ promoted the hydrophobic property of GDL. The water will be rapidly removed from the electrode resulting in the dry out of Nafion membrane as well as the loss of proton conductivity. In case of TiO$_2$, the contact angle increased as the increase of TiO$_2$ loading during 0.03 to 0.06 mg/cm$^2$ which is able to enhance the current density at 0.6 V of single-cell tests. This is because addition of TiO$_2$

to the catalyst layer bring the catalyst to improve the hydrophilic property of GDL and catalyst layer to avoid fast dryout of PEM at low current densities. Otherwise, the over loading of $TiO_2$ to 0.45 mg/cm$^2$ induced a diminished fuel cell performance because it functioned as an insulating phase in the catalyst layer, resulting in the increasing of the ICR of the catalyst layer (Figure 4.5). In addition, a high $TiO_2$ content can induce a high mass transport limitation because it could combine or adsorb a large quantity of water molecules and so hinder the accessibility of the fuel gas/oxidant to the reaction site. Another possible reason might be that, under an oxygen atmosphere, $TiO_2$ can adsorb oxygen molecules, which then capture electrons from the conduction band and the donor states of $TiO_2$ to form $O_2^-$ and so cause a decreased dark conductivity [82-83]. Although the presence of $TiO_2$ at 0.03 to 0.45 mg/cm$^2$ reduced the electrical conductivity of the $TiO_2$-PtCo/C catalyst 1.78- to 5.40-fold, the cell performances at 0.6 V were still 1.14- to 1.36-fold higher than that of the PtCo/C catalyst (Table 4.2). This indicates that the hydrophilic property of $TiO_2$ plays an important role in the performance of the fuel cell, particular at a medium-to-high current density.

To further understand the effect of the $TiO_2$ loading on the kinetic and mass transport parameters of the electrode, the relationship between the cell potential and current density for the entire current density range was evaluated using a non-linear least squares approach, as expressed by Eq. (4.3) [84];

$$E = E_0 - b\log j - jR - m \exp(nj) \qquad (4.3)$$

where $E_0 = E_r + b \log j_0$; $E_r$ is the reversible potential for the cell; $b$ is the Tafel slope for the ORR; $R$ is the all resistances due to the ohmic resistance contributed from the proton transfer through membrane and the electron transfer through the fuel cell components, and the mass-transport resistance in the intermediate current density region; $j$ is the current density; $j_0$ is the exchange current density, and $m$ and $n$ are the parameters related to the mass transport limitation and mass-transport overpotential, respectively. The $m$ value affects both the slope of the linear region of the current density-potential plot and the region where the current density departs from linearity, whereas the $n$ value has a

major effect on the dependence of the current density-potential curve after the linear region [84]. High values of $m$ and $n$ indicate a high mass transport limitation and mass-transport overpotential in the system, respectively.
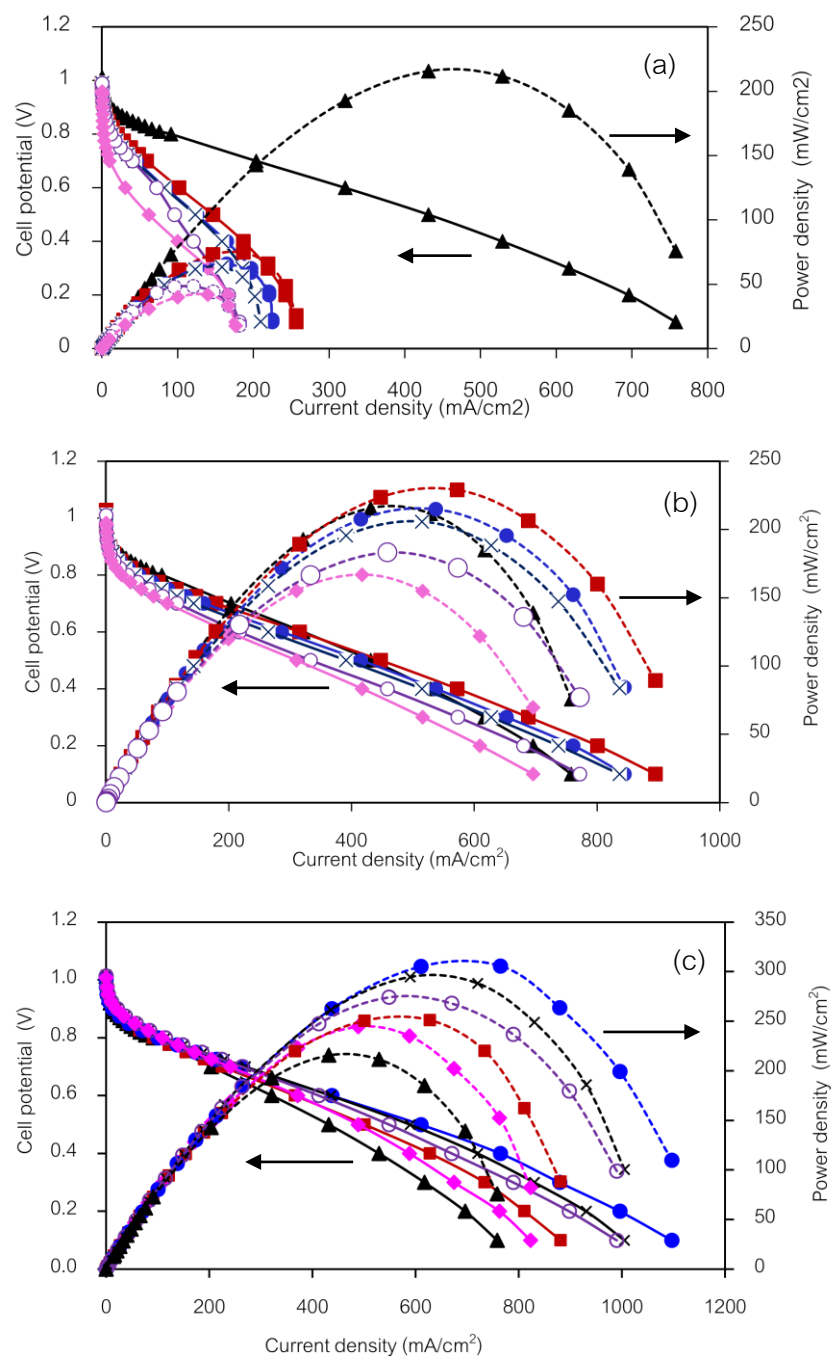


Figure 4. 9 Polarization curves of a single $H_2/O_2$ PEM fuel cell of the as-prepared $MO_2$-PtCo/C catalyst at $MO_2$ loadings of (▲) 0.0, (■) 0.03, (●) 0.06, (✗) 0.15, (○) 0.30 and (◆) 0.45 mg/cm$^2$; (a) $CeO_2$-PtCo/C, (b) $MoO_2$-PtCo/C, and (c) $TiO_2$-PtCo/C.
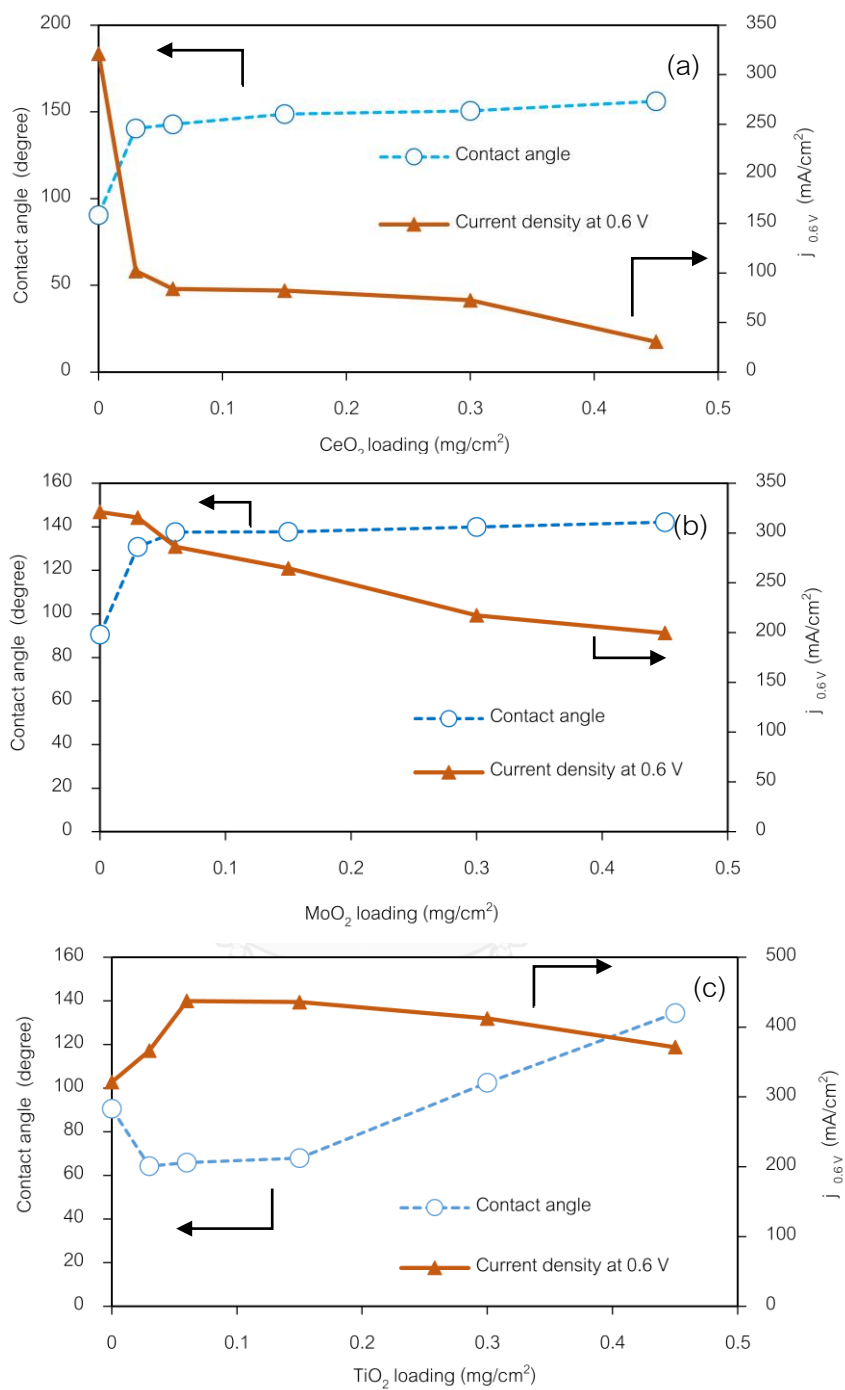
Figure 4. 10 Comparison between contact angle and current density at 0.6 V of the as-prepared $MO_2$-PtCo/C catalyst at $MO_2$ loadings of (O) Contact angle and (▲) Current density at 0.6 V; (a) $CeO_2$-PtCo/C, (b) $MoO_2$-PtCo/C, and (c) $TiO_2$-PtCo/C.

Table 4. 2 Electrochemical properties of the PtCo/C-catalyst layer at different $MO_2$ loadings.

| Type of catalyst | Loading of metal oxide (mg/cm$^2$) | OCV (V) | $j_{0.9\,V}$ (mA/cm$^2$) | $j_{0.6\,V}$ (mA/cm$^2$) |
|---|---|---|---|---|
| PtCo/C | - | 1.012 | 10.8 | 321.2 |
| CeO$_2$-PtCo/C | 0.03 | 0.991 | 2.6 | 101.9 |
| | 0.06 | 0.982 | 2.6 | 84 |
| | 0.15 | 0.991 | 2.2 | 82.2 |
| | 0.3 | 0.99 | 2 | 72.4 |
| | 0.45 | 0.958 | 0.8 | 30.6 |
| MoO$_2$-PtCo/C | 0.03 | 0.983 | 6.8 | 315.6 |
| | 0.06 | 1.003 | 6.4 | 286.4 |
| | 0.15 | 1.008 | 5.6 | 264.6 |
| | 0.3 | 1.011 | 3.4 | 217.4 |
| | 0.45 | 1.01 | 3 | 199.6 |
| TiO$_2$-PtCo/C | 0.03 | 1.002 | 15.2 | 366.2 |
| | 0.06 | 1.004 | 12.4 | 437.6 |
| | 0.15 | 1.017 | 20.2 | 435.8 |
| | 0.3 | 1.013 | 21.6 | 412.4 |
| | 0.45 | 1.008 | 19.2 | 371.4 |

The fitted results, together with the coefficient of determination ($R^2$), are summarized in Table 4.3. The $R^2$ values for all catalysts were greater than 0.9992, indicating that the fitted model was adequate to predict the experimental data. Within the fitting error, the intrinsic Tafel slopes ($b$) for the ORR varied between -63.4 to -69.9 mV/dec under identical testing conditions. These changes might be attributed to the variation in the interphase conditions in the presence of different loadings of TiO$_2$. Theoretically, a

Tafel slope of -60 mV/dec indicates an ORR mechanism involving an initial fast charge-transfer step followed by the rate-determining chemical step [85]. A higher Tafel slope value is found at low $O_2$ concentrations due to mixed activation/mass-transport control. The exchange current density ($j_0$) was found to increase as the $TiO_2$ loading increased up to 0.15 mg/cm$^2$ and remained essentially constant thereafter with further increases in the $TiO_2$ loading. This is consistent with the ORR activity estimated at 0.9 V ($j_{0.9V}$) as reported in Table 4.2.

Table 4. 3 Electrode kinetics and mass transport parameters, obtained from fitting the polarization data of Eq. (4.3), for the different types of supported PtCo/C catalysts.

| Type of catalyst | Activation loss | | Ohmic loss | Mass transport loss | | $R^2$ |
|---|---|---|---|---|---|---|
| | $-b$ (mV/dec) | $j_0$ (mA/cm$^2$) | $R$ ($\Omega$-cm$^2$) | $m$ (mV) | $n$ (cm$^2$/mA) | |
| PtCo/C | 67.0 | $7.19 \times 10^{-4}$ | 0.7000 | 0.0015 | 0.0062 | 0.9992 |
| $TiO_2$(0.03)-PtCo/C | 69.5 | $8.78 \times 10^{-4}$ | 0.5572 | 0.0008 | 0.0060 | 0.9994 |
| $TiO_2$(0.06)-PtCo/C | 69.9 | $9.61 \times 10^{-4}$ | 0.5050 | 0.0005 | 0.0052 | 0.9995 |
| $TiO_2$(0.15)-PtCo/C | 66.4 | $9.93 \times 10^{-4}$ | 0.5100 | 0.0015 | 0.0047 | 0.9997 |
| $TiO_2$(0.30)-PtCo/C | 63.4 | $9.92 \times 10^{-4}$ | 0.5860 | 0.0029 | 0.0043 | 0.9999 |
| $TiO_2$(0.45)-PtCo/C | 66.1 | $9.93 \times 10^{-4}$ | 0.5890 | 0.0052 | 0.0045 | 0.9992 |

The variation of the resistance ($R$) and mass transport limitation parameters ($m$ and $n$) as a function of the $TiO_2$ loading are plotted in Figure 4.11. The incorporation of $TiO_2$ at a loading of between 0.03 to 0.06 mg/cm$^2$ resulted in a 1.10-, 1.60- and 1.15-fold decrease in the $R$, $m$ and $n$ parameters, respectively. Further increasing the $TiO_2$ loading on the PtCo/C catalyst from 0.06 to 0.45 mg/cm$^2$ slightly decreased $n$ by 1.16-fold, but increased $R$ and $m$ by 1.17 and 10.4-fold, respectively. Thus, a high $TiO_2$ content induced a high mass transport limitation, which, as mentioned previously, may be because a high quantity of $TiO_2$ particles can combine or adsorb a large quantity of water molecules and so hinder the accessibility of the fuel/oxidant to the reaction site. In addition, the $TiO_2$

particles can absorb water molecules from the membrane layer and so decrease the proton conduction of the membrane [86].

A decreased proton conductivity with increasing $TiO_2$ loadings has been reported previously for the addition of a nano-$TiO_2$ film onto the membrane surface [87]. The high $TiO_2$ content increased the interfacial contact resistance of the catalyst (Table 1) because it functioned as an insulating phase, as mentioned previously. In addition, a high $TiO_2$ content can adsorb a high quantity of oxygen from the reactant feed, resulting in a loss of electrons from the conduction band and donor state and so a decreased conductivity [83-84]. Accordingly, the addition of an appropriate quantity of $TiO_2$ on the PtCo/C catalyst can help to decrease the mass transport limitation as well as the ohmic resistance of the catalyst layer.
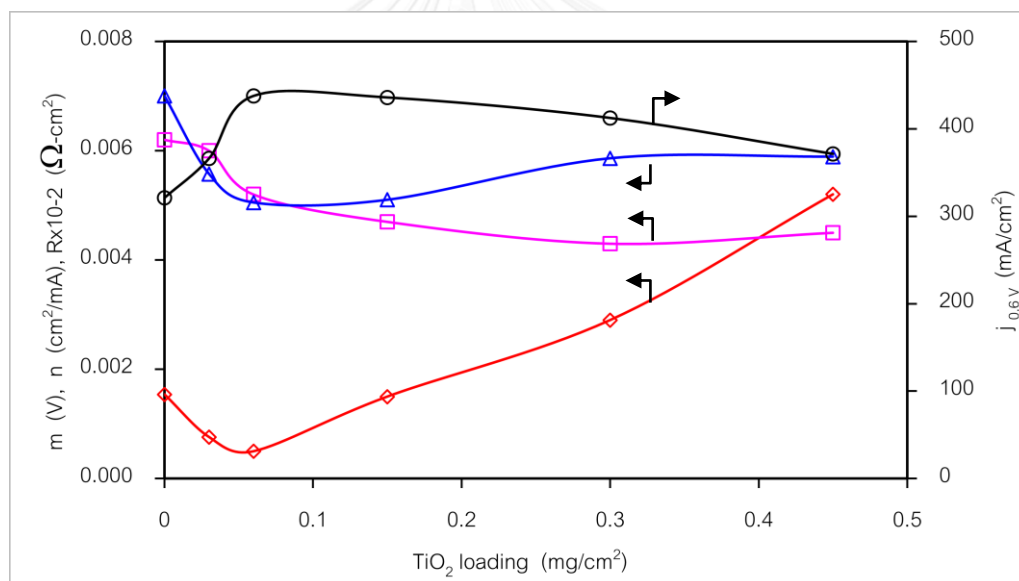


Figure 4. 11 Variation in the ($\diamond$) m, ($\square$) n and ($\triangle$) R parameters, as estimated from Eq. (4.3), and the ($\bigcirc$) current density at 0.6 V ($j_{0.6V}$) for the $TiO_2$-PtCo/C catalyst at different $TiO_2$ loadings.

## 4.4 Effect of TiO$_2$ phase

From the previous results, the TiO$_2$ showed the highest potential to promote the fuel cell performance by improve the water management in medium to high current density range. However the TiO$_2$ has 3 main phases: anatase, rutile and brookite. Anatase and rutile phase have been interested in many research field because their excellent mechanical and high corrosion resistance in both acid and alkaline environment [88], then the next study will explore the effects of the TiO$_2$ phase on the performance of the PEM fuel cell.

The PtCo/C catalyst incorporated with two types of commercial TiO$_2$ were studied. The first is PtCo/C with the presence of the mixed phaseTiO$_2$ between anatase and rutile in the ratio of 4:1, TiO$_2$(AR)-PtCo/C, while the second is PtCo/C with the presence of the pure rutile phase, TiO$_2$(R)-PtCo/C. Figure 4.12 shows typical XRD patterns of the TiO$_2$(AR), TiO$_2$(R), TiO$_2$(AR)-PtCo/C and TiO$_2$(R)-PtCo/C catalysts with TiO$_2$ loadings of 0.06 and 0.15 mg/cm$^2$. As shown in this figure, the diffraction patterns of commercial TiO$_2$(AR) and TiO$_2$(R) are observed at 25.28°, 37.80° and 48.05° corresponding to the TiO$_2$ anatase diffraction, [101], [004], and [200] , respectively. The TiO$_2$ diffraction peaks of rutile structures also showed the peak at 27.5°, 62.3°, and 68.9° represent to [110], [002], and [301] planes, respectively. When TiO$_2$(AR) or TiO$_2$(R) was incorporated onto the surface of PtCo/C catalyst, their XRD patterns also exhibited the characteristic Pt peaks of a FCC structure.
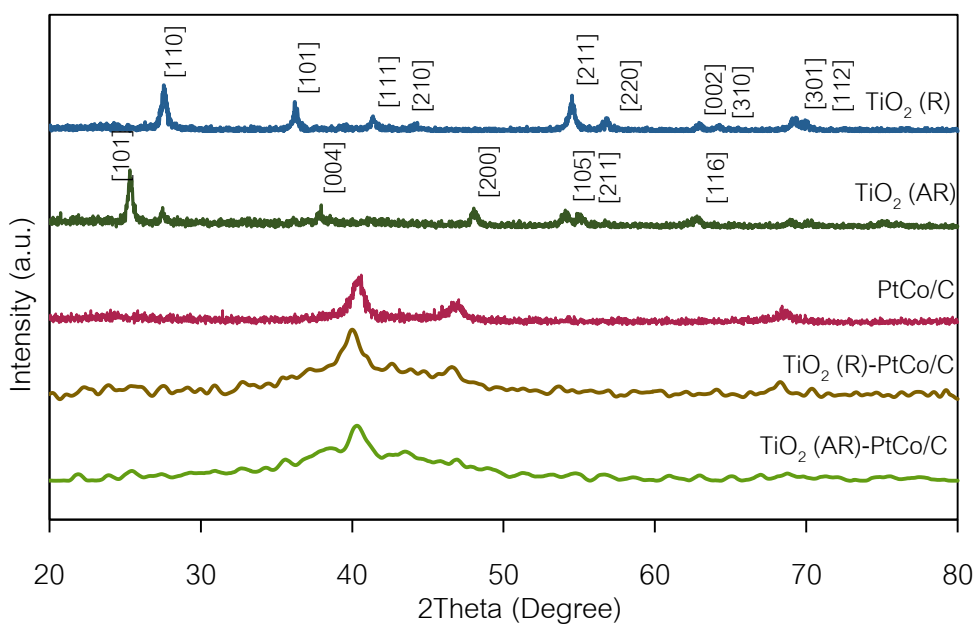
Figure 4. 12 Representative XRD patterns of the as-prepared PtCo/C catalysts in the absence or presence of $TiO_2(AR)$ or $TiO_2(R)$ at $TiO_2$ loading of 0.15 mg/cm$^2$.

However, the XRD features for $TiO_2$ were not observed which might be attributed to the presence of $TiO_2$ in a very small amount and/or in an amorphous form. The *d*-spacing values of all $TiO_2$-PtCo/C catalysts were still lower than that of the commercial Pt/C and were broadly similar to that of the PtCo/C catalyst, indicating that the incorporation of $TiO_2$ on the surface of PtCo/C had no effect on the alloy property of the PtCo/C catalysts. By using the Debye-Scherrer equation, the crystalline size for the PtCo particles in the PtCo/C catalyst was determined to be in the range of 7.41-7.84 nm (Table 4.4). The incorporation of either $TiO_2(AR)$ or $TiO_2(R)$ had no significant influence on the crystalline size of PtCo/C catalyst.

Table 4. 4 Morphology of the PtCo/C-catalyst layer at different $TiO_2$ phases and loadings.

| Type of catalyst | $d$-spacing (nm) | Crystalline size (nm) | ESA $(m^2/g)$ | $j_{0.9\,V}$ $(mA/cm^2)$ | $j_{0.6\,V}$ $(mA/cm^2)$ |
|---|---|---|---|---|---|
| PtCo/C | 0.2231 | 7.67 | 47.3 | 14.4 | 321.2 |
| $TiO_2$(0.06AR)-PtCo/C | 0.2237 | 7.44 | 72.2 | 18.4 | 437.6 |
| $TiO_2$(0.15AR)-PtCo/C | 0.2235 | 7.41 | 71.8 | 20.2 | 435.8 |
| $TiO_2$(0.06R)-PtCo/C | 0.2235 | 7.68 | 43.7 | 13.2 | 309.2 |
| $TiO_2$(0.15R)-PtCo/C | 0.2227 | 7.51 | 36.9 | 12.6 | 301.8 |

The activities of the as-prepared PtCo/C-, $TiO_2$(AR)-PtCo/C- and $TiO_2$(R)-PtCo/C catalysts in the ORR were tested in a single PEM fuel cell at 60 $^{\circ}$C and atmospheric pressure (~101.3 kPa) under a $H_2/O_2$ condition. As demonstrated in Figure 4.13, the major reason for the power performance difference was the differences in ohmic resistance and mass transport resistance. The inclusion of either $TiO_2$(AR) or $TiO_2$(R) in the PtCo/C catalyst layer did not significantly affect the open circuit potential of the single cell, but significantly affected the cell performance, particularly at medium-to-high current densities. Under the activation-controlled region, the presence of $TiO_2$(R) slightly changed the ORR activity, determined in terms of the current density at a potential of 0.9 V ($j_{0.9\,V}$), of the PtCo/C catalysts. However, the presence of $TiO_2$(AR) enhanced the activity of the PtCo/C catalysts. Under a medium-to-high current density, the inclusion of $TiO_2$(AR) into the PtCo/C catalyst layer provided a higher current density compared to that in the presence of $TiO_2$(R) at the same loading. For example, at a loading of 0.06 mg/cm$^2$, replacing the $TiO_2$(R) by $TiO_2$(AR) increased the current density at 0.6 V ($j_{0.6\,V}$) of some 1.42-fold from 309 to 438 mA/cm$^2$ (186 to 263 mW/cm$^2$). To understand the effect of $TiO_2$ phase, it is necessary to take into account the composition and property of $TiO_2$. The electrical conductivity of a $TiO_2$(R)-based mixed oxide was reported to be higher than a

non-crystalline or $TiO_2(A)$-based mixed oxide [89], whilst $TiO_2(A)$ exhibits a hydrophilic behavior [90-91]. Although the incorporation of $TiO_2(AR)$ could reduce the electrical conductivity of the catalyst layer, because of its low electrical conductivity compared to the carbon support and metal catalysts, an appropriate quantity of $TiO_2(AR)$ can improve the hydrophilic properties of the catalyst layer and also prevent the drying out of the membrane, which results in an increased proton conductivity.

From the ORR activity test, although the $TiO_2(0.06AR)$-PtCo/C catalyst exhibited a lower kinetic current density (7.10 $mA/cm^2$) than that of $TiO_2(0.15AR)$-PtCo/C catalyst (9.39 $mA/cm^2$) in acid solution, it provided a slightly higher current density at 0.6 V tested in PEM fuel cell (Table 4.4). For actual application of such catalyst, the performance in PEM fuel cell should be considered first. Thus, it can be said that the optimum $TiO_2(AR)$ in PtCo/C catalyst for ORR in PEM fuel cell was 0.06 $mg/cm^2$.
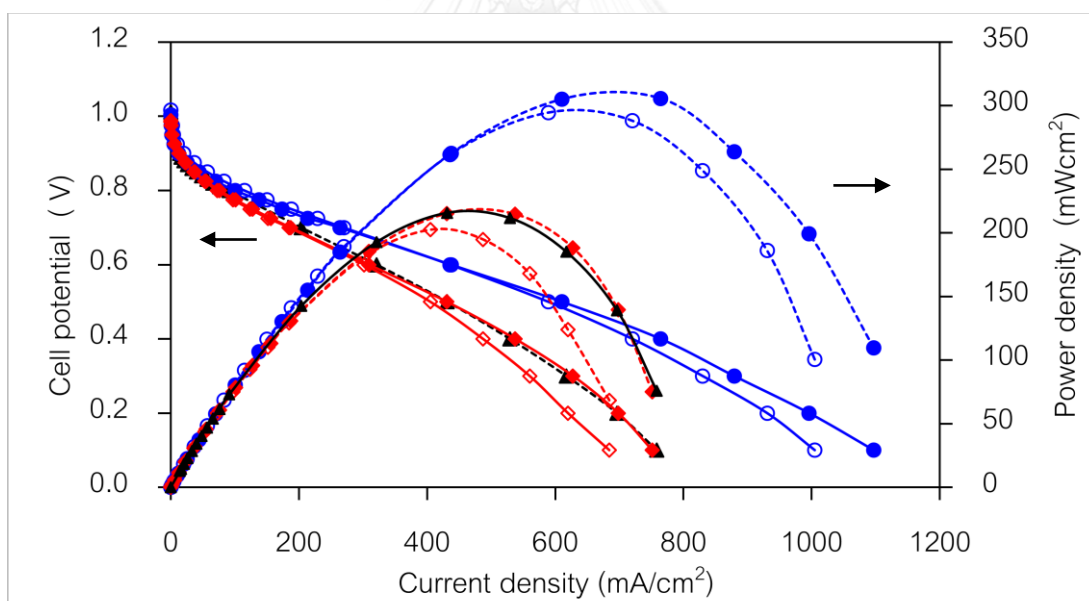


Figure 4. 13 Current density-potential curves of a single $H_2/O_2$ PEM fuel cell with the as-prepared PtCo/C catalyst in the (▲) absence of $TiO_2$, and in the presence of (●,○) $TiO_2(R)$ or (◇,◆) $TiO_2(AR)$ at a loading of (●,◆) 0.06 and (○,◇) 0.15 $mg/cm^2$

## 4.5 Stability of MO$_2$-PtCo/C catalyst

The stability of all MO$_2$-PtCo/C catalysts was finally monitored by the change of ESA during the repetitive potential cycling of these catalysts in N$_2$-saturated 0.5 M H$_2$SO$_4$. The example cyclic voltammogram of MO$_2$-PtCo/C catalysts was exhibits in Figure 4.14(a). The similar pattern of cyclic voltammogram of all as-prepared catalyst was observed. Namely, the H$_2$ adsorption peak appeared as a broad shoulder, not in a sharp peak, probably due to the partial overlapping with the reduction peaks of the oxygen atom (Pt-O reduction). The H$_2$ desorption peak appeared as a clear sharp peak. Increasing the potential cycling from the first cycle to the 10$^{th}$ cycle resulted in the increase of peak intensity, due to the initial wetting of the thin Nafion layer covering the catalyst particles [67]. Further rising the repetitive potential cycling led to the decrease of peak intensity, indicating the decrease of ESA of the catalyst. To compare the catalyst stability, the normalized ESA was calculated by Eq. (4.4).

$$\text{Normalized ESA} = \frac{\text{ESA}}{\text{ESA}_{\text{Max}}}$$

(4.4)

where ESA is the electrochemical surface area and ESA$_{\text{Max}}$ is the maximum electrochemical surface area of each sample.

As summarized in Figure 4.14(b), the loss of normalized ESA of catalysts after 200 cycles was observed as the order of CeO$_2$-PtCo/C > MoO$_2$-PtCo/C > PtCo/C > TiO$_2$-PtCo/C. Approximately 78%, 43%, 28% and 20% were observed for CeO$_2$-PtCo/C, MoO$_2$-PtCo/C, PtCo/C and TiO$_2$-PtCo/C, respectively. This suggests that the TiO$_2$-PtCo/C catalyst had the most stability compared with the other catalysts. This is probably due to a strong resistance of TiO$_2$ in acid media. To get more information about the resistance of all investigated catalysts, the corrosion test of all catalysts was then carried out in 0.5 M H$_2$SO$_4$. As the Tafel plot (Figure 4.15), the magnitude of corrosion current density was changed as the order of CeO$_2$-PtCo/C > MoO$_2$-PtCo/C > PtCo/C > TiO$_2$-PtCo/C as 14.17,

9.37, 6.71 and 5.68 mA/cm$^2$, respectively. This confirms that the TiO$_2$-PtCo/C exhibited the highest corrosion resistance compared to other MO$_2$-PtCo/C catalysts.
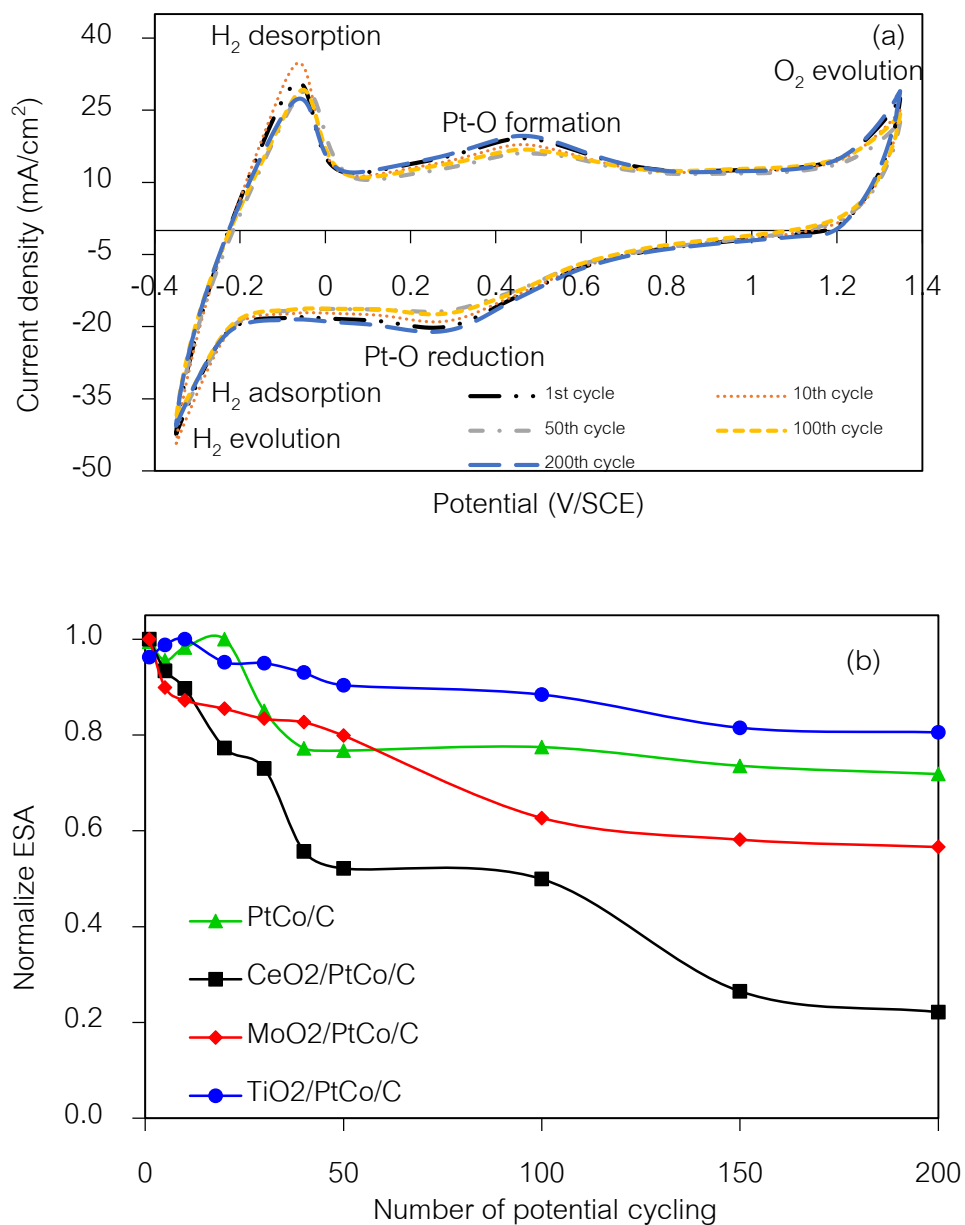


Figure 4. 14 (a) Cyclic voltammogram of TiO$_2$-PtCo/C catalyst after the cycle numbers of repeated potential cycling in 0.5 M H$_2$SO$_4$ at a scan rate of 20 mV/s and (b) variation of normalized ESA.
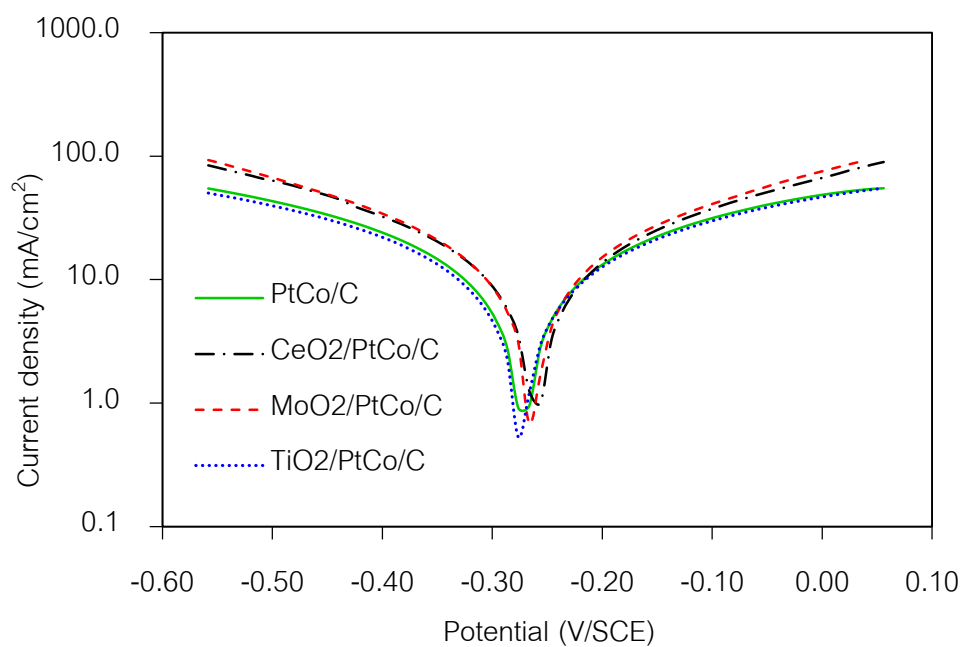
Figure 4. 15 Potentiodynamic polarization for corrosion of PtCo/C and MO$_2$-PtCo/C catalysts in 0.5 M H$_2$SO$_4$.
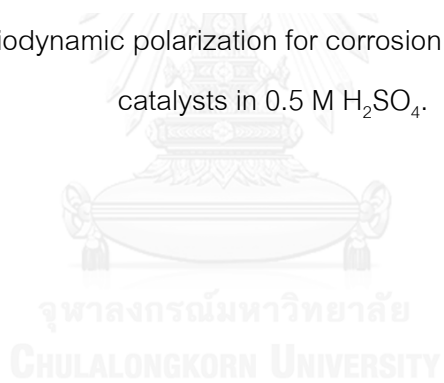
CHAPTER 5

ORR activity of PtCo/C catalyst in the presence of $TiO_2$ layer prepared by CVD

In the previous chapter, the effects of different metal oxide types and loadings on the ORR activity of PtCo/C catalyst layer were presented. The results showed the PtCo/C catalyst in presence of $TiO_2$ layer had higher activity than PtCo/C catalyst in presence of $CeO_2$ and $MoO_2$ layer. In this chapter, we will focus our attention on the $TiO_2$ incorporation procedure on PtCo/C catalyst layer by CVD technique. Morphology of either $TiO_2$ prepared by CVD and $TiO_{2,CVD}$-PtCo/C catalyst will be explored. Finally, their ORR activity will be studied in acid solution and PEM fuel cell under $H_2/O_2$ environment.

5.1 Effect of preparing condition on morphology of $TiO_2$

In the primary study, the comparison of $TiO_2$ particle morphology with different reactant concentrations and deposition temperatures were determined. Figure 5.1 exhibits the SEM micrograph of $TiO_2$ particle obtained from different concentrations of TTIP in the range of 0.01 – 0.05 M. It was clearly seen that the $TiO_{2,CVD}$ particles were interfered together and formed the spherical shape. The precursor concentration did not effect on shape but affected the size of $TiO_{2,CVD}$ particles.

The particle size of $TiO_2$ decreased with an increasing TTIP concentration (Table 5.1). This is because the high reactant concentration can achieve a fast reaction rate. Then, the nucleation process can be promoted more than particle growth process. Thus, many nuclei of $TiO_2$ metal were produced [92] leading to the generation of small metal particle size. Then the TTIP concentration at 0.05 M would be used in the next step. Regarding the effect of deposition temperature, it was clearly seen that the $TiO_2$ particles deposited at 350 °C had a bigger than that of $TiO_2$ particles deposited at 450 °C (Figure 5.2). Since, the temperature had affected on both nucleation and growth processes of particle formation process. The low temperature brought the metal nuclei to lower mobility

along the substrate surface than that at high temperature, resulting in a higher particle growth rate and bigger particle size [93-97]. However, the deposition at high temperature affected the disintegration of substrate compositions. Figure 5.3 shows the thermogravimetric analysis of carbon cloth with sublayer substrate from 80 to 800 °C. The degradation of substrate started at temperature around 407 °C. So, the deposition temperature used in this study will be around 350 °C.
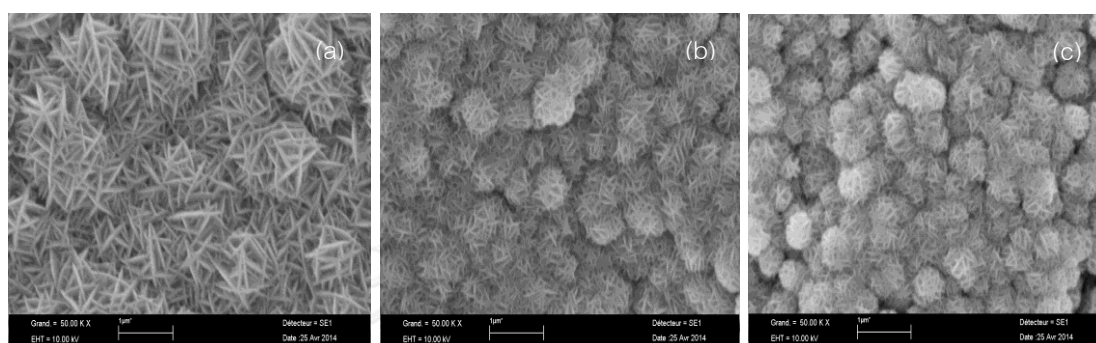


Figure 5. 1 SEM micrographs of TiO$_2$ particle with different reactant concentrations of TTIP at (a) 0.01 M, (b) 0.025, and (c) 0.05 M

Table 5. 1 Preparation conditions of TiO$_2$ coated by CVD at 20 torr

| Sample | Temperature (°C) | [TTIP] (M) | Loading (mg/cm$^2$) | Particle Size (µm) |
|--------|------------------|------------|---------------------|--------------------|
| T1 |     | 0.01  | 0.1350 | 1.216 |
| T2 | 350 | 0.025 | 0.1314 | 0.705 |
| T3 |     | 0.05  | 0.1317 | 0.679 |
| T4 | 450 | 0.05  | N/A    | 0.313 |
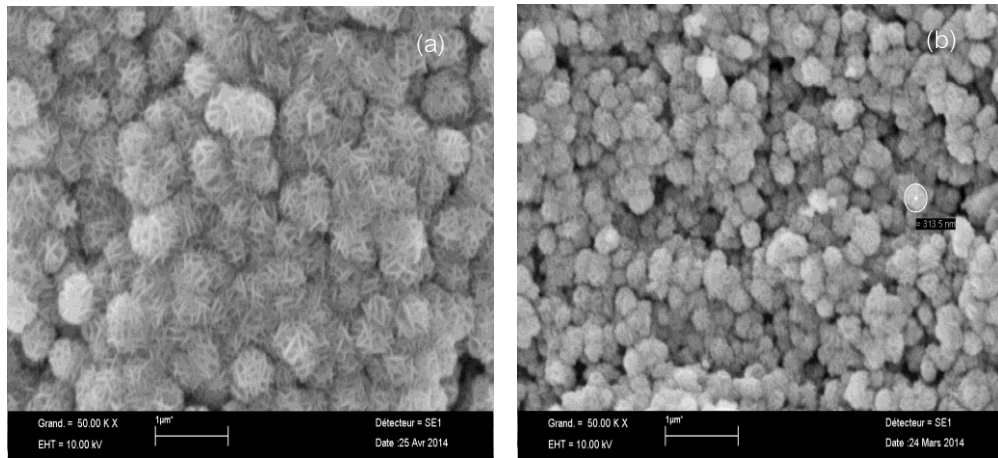
Figure 5. 2 SEM micrographs of TiO$_2$ particle with different deposition temperature of (a) 350 °C and (b) 450 °C
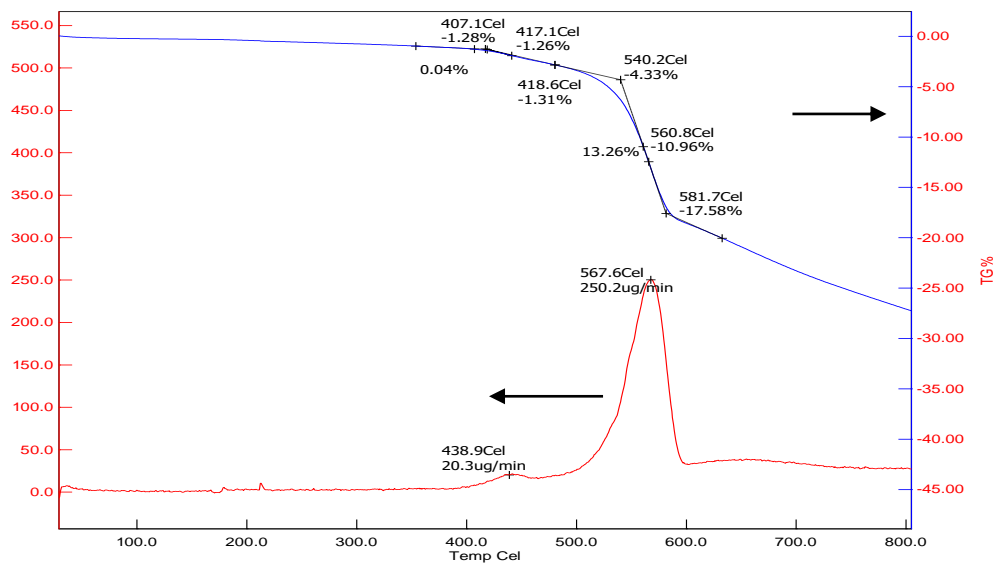


Figure 5. 3 Thermo-gravimetric analysis (TGA, blue) and the differential temperature curves (DTG,Red) of carbon cloth with sublayer substrate

5.2 Morphology of $TiO_{2,CVD}$-PtCo/C catalyst layer (electrode)

The XRD patterns of the crystalline structures of PtCo/C in the presence of different $TiO_2$ loadings prepared by CVD technique are shown in Figure 5.4. For comparative purpose, the XRD pattern of 30 wt.% of PtCo/C and pure $TiO_{2,CVD}$ deposited on sub-layer coated gas diffusion layer (sGDL) are also included in this figure. The diffraction peaks of as-prepared PtCo/C catalyst at $2\theta$ values of $39.67^{\circ}$, $45.80^{\circ}$ and $67.78^{\circ}$ assigned the crystal planes of Pt at (111), (200) and (220), respectively with a face centered cubic (fcc) structure. Furthermore, no characteristic peak of Co was found in XRD pattern, suggesting that it may be present in a very small amount and/or in an amorphous form. In addition, $TiO_2$ showed the characteristic peaks at about $25.28^{\circ}$, $37.80^{\circ}$ and $48.05^{\circ}$ corresponding to the [101], [004], and [200] diffraction planes of anatase phase were presented in $TiO_{2,CVD}$-PtCo/C catalyst. From Figure 5.4, the intersection between a peak [002] of carbon and peak [101] of $TiO_2$ in anatase phase were observed. When $TiO_{2,CVD}$ was incorporated onto the surface of PtCo/C catalyst, their XRD patterns also exhibited the characteristic $TiO_2$ peaks (Figure 5.4) and increased with increasing of $TiO_{2,CVD}$ loading. However, the XRD feature for PtCo alloy was very less intensity than $TiO_{2,CVD}$, which might be attributed to the presence of PtCo particle in a very small amount.

The mean crystalline size of PtCo/C catalyst was calculated from the (111) diffraction line of Pt using Scherrer equation. The crystalline sizes of PtCo in all of $TiO_{2,CVD}$-PtCo/C catalysts were 7.10 nm as shown in Table 5.2. The SEM images of the PtCo/C and $TiO_{2,CVD}$-PtCo/C catalysts coated on the GDL are shown in Figure 5.5. The EDX spectrum (Figure 5.5 (a1 and b1)) revealed the presence of Pt, Co and Ti on the $TiO_{2,CVD}$-PtCo/C catalysts. From Figure 5.5 (a2 and b2), one can see that there are large number of grain boundaries and voids in the catalyst layer. The elemental map of the catalyst layer in both of catalysts for Pt, Co and Ti demonstrates that all metals had a well dispersion on catalyst substrate.
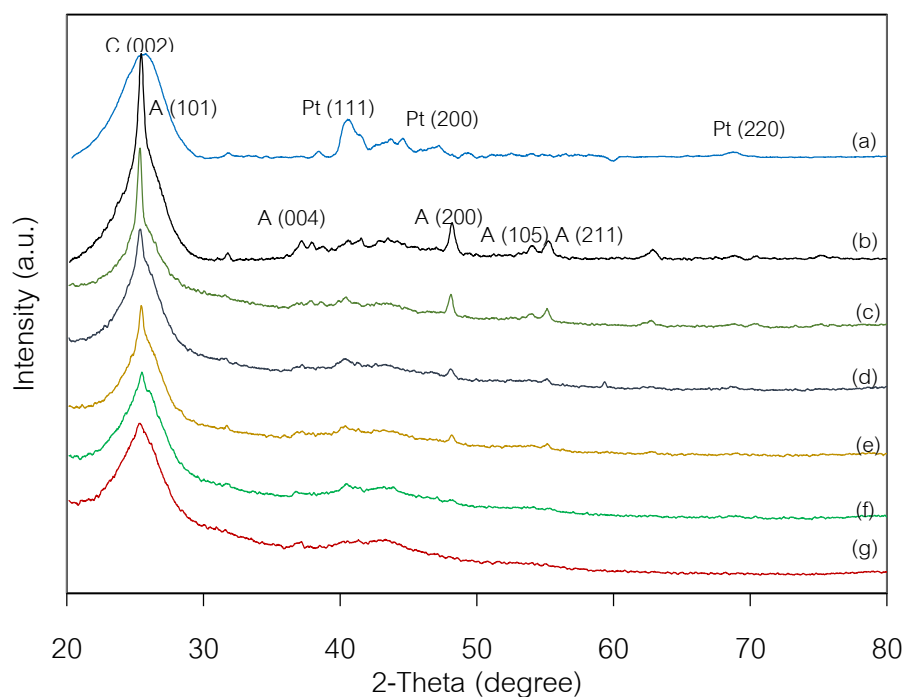
Figure 5. 4 X-ray diffraction patterns of (a) PtCo/C, (b) $TiO_{2,CVD}$ and $TiO_{2,\,CVD}$-PtCo/C

catalysts at different $TiO_2$ contents: (c) 0.03, (d) 0.06, (e) 0.15, (f) 0.3, (g) 0.45 mg/cm$^2$.

Table 5. 2 Morphology of the PtCo/C-catalyst layer at different $TiO_2$ loadings prepared by CVD.

| Catalyst | $TiO_{2,CVD}$ loading (mg/cm$^2$) | $d$-spacing (nm) | Crystalline size (nm) |
|---|---|---|---|
| Pt-Co/C | - | 0.217 | 7.11 |
| $TiO_{2,CVD}$-PtCo/C | 0.03 | 0.217 | 7.10 |
| | 0.06 | 0.217 | 7.10 |
| | 0.15 | 0.217 | 7.10 |
| | 0.30 | 0.217 | 7.10 |
| | 0.45 | 0.218 | 7.11 |
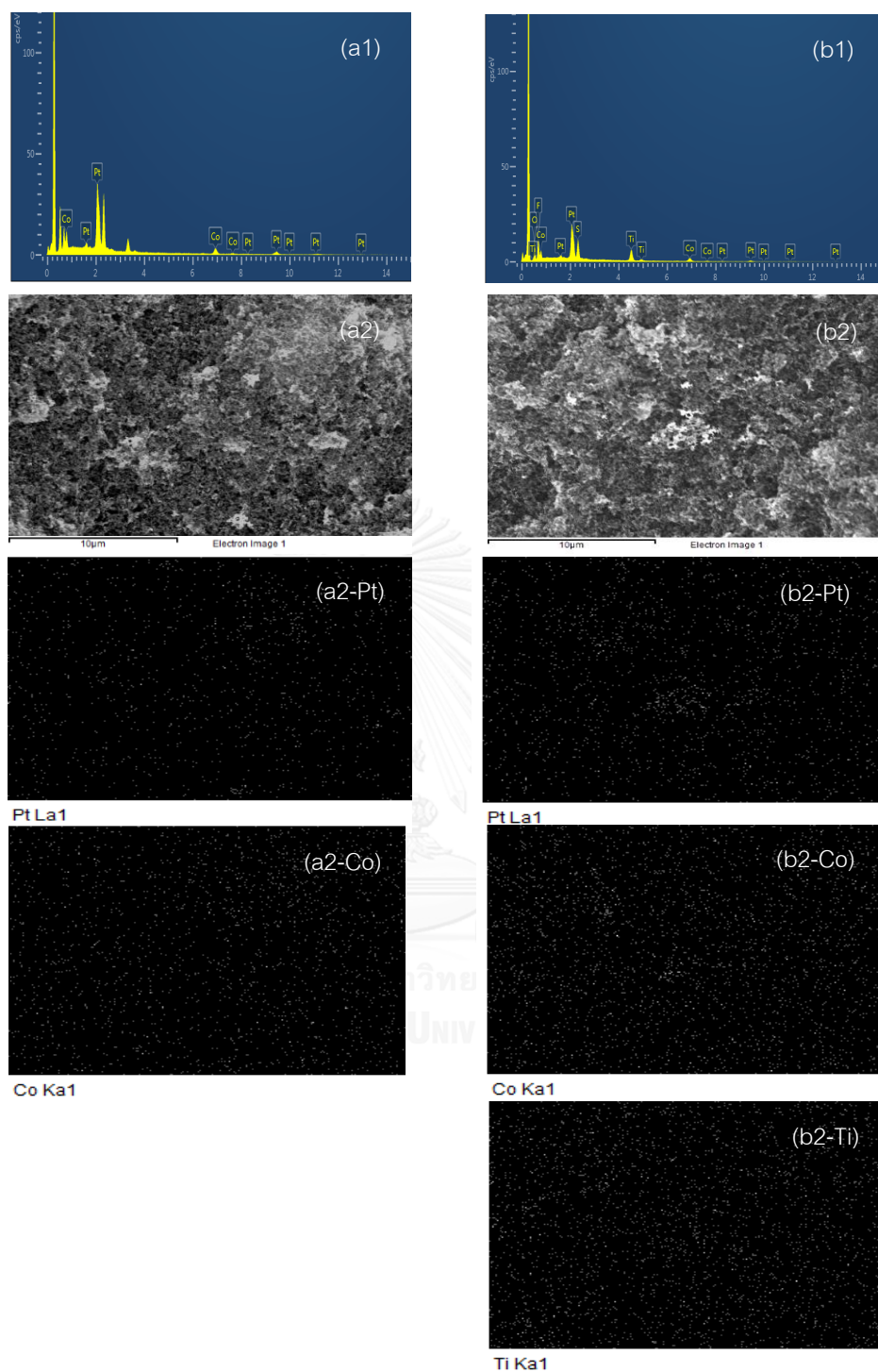
Figure 5. 5 EDX spectra of elements (a1 and b1), SEM micrographs of crystalline particles (a2 and b2), and X–ray images used to map the location of the elements dispersion (Pt, Co and Ti) of (a) PtCo/C and (b) $TiO_{2,\,CVD}$-PtCo/C catalysts at $TiO_{2,CVD}$ loading of 0.15 mg/cm$^2$.

## 5.3 Electrochemical property of $TiO_{2,CVD}$-PtCo/C catalyst layer

The evaluation of electrocatalytic performance of catalyst layer was carried out by electrochemical methods including cyclic voltammetry and ICR. The ORR activity of all catalysts was tested in acid solution by linear sweep voltammetry (LSV) with rotating disk electrode (RDE) and in PEM fuel cell under $H_2/O_2$ environment.

Figure 5.6 shows cyclic voltammograms of $TiO_{2,CVD}$-PtCo/C catalysts together with that of PtCo/C catalyst in 0.5 M $H_2SO_4$ solution under $N_2$-saturated condition. The CV curves measurements were recorded in the range of potential from -0.35 to 1.2 V/SCE. All shapes of the voltammograms are very similar and corresponding to the typical voltammogram of Pt nanoparticles in acid medium [69, 98]. The ESA was determined from the charge corresponding to the oxidation peak of proton, which is formed due to desorption of a monolayer of chemisorbed hydrogen as shown in Appendex B. The calculated ESA values of all the catalysts are presented in Figure 5.7. It can be seen that the ESA for $TiO_{2,CVD}$-PtCo/C catalyst was larger than that of the PtCo/C catalyst in the presence of $TiO_{2,CVD}$ indicating that the $TiO_{2,CVD}$-PtCo/C catalyst had more available active sites to reach the reaction.

Interestingly, the increasing trend of in ESA with respect to the increasing $TiO_2$ content was similar to that reported for $PtTiO_2$/C [99]. According to literatures, the increased ESA for Pt in the presence of $TiO_2$ may be due to the $TiO_2$ can modify favorably the structural and electronic features of Pt to carry the H-adsorption [5, 100-103]. However, too high $TiO_2$ loading (> 0.15 mg/cm$^2$) induced a diminished site reaction because the oxide layer functioned an insulating phase in the catalyst layer, resulting in the reduction of the electrical conductivity of the catalyst layer.
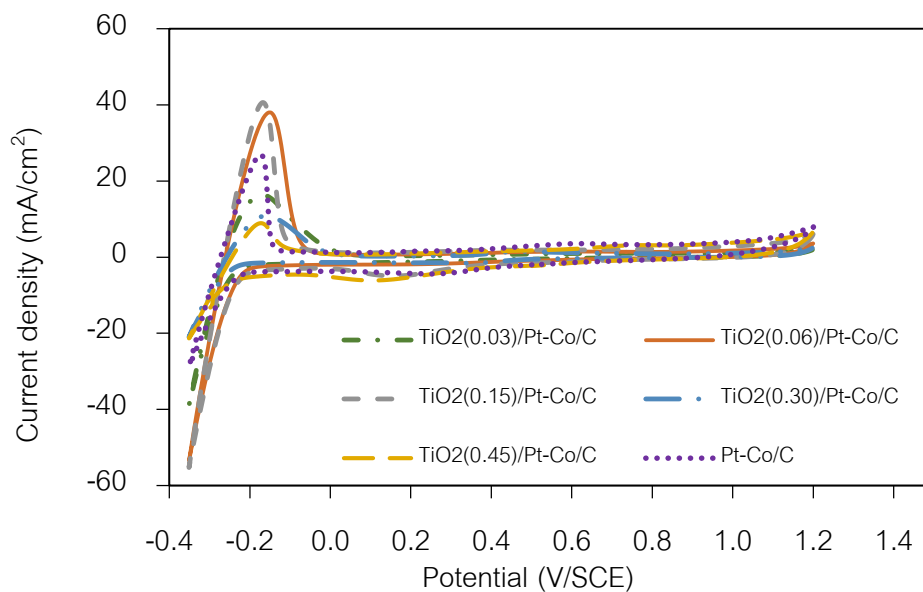
Figure 5. 6 Cyclic voltammetry of the as-prepared $TiO_{2, CVD}$-PtCo/C catalyst at different $TiO_{2, CVD}$ loadings in 0.5 M$H_2SO_4$ ($N_2$ sat.) at scan rate 20 mV/s.
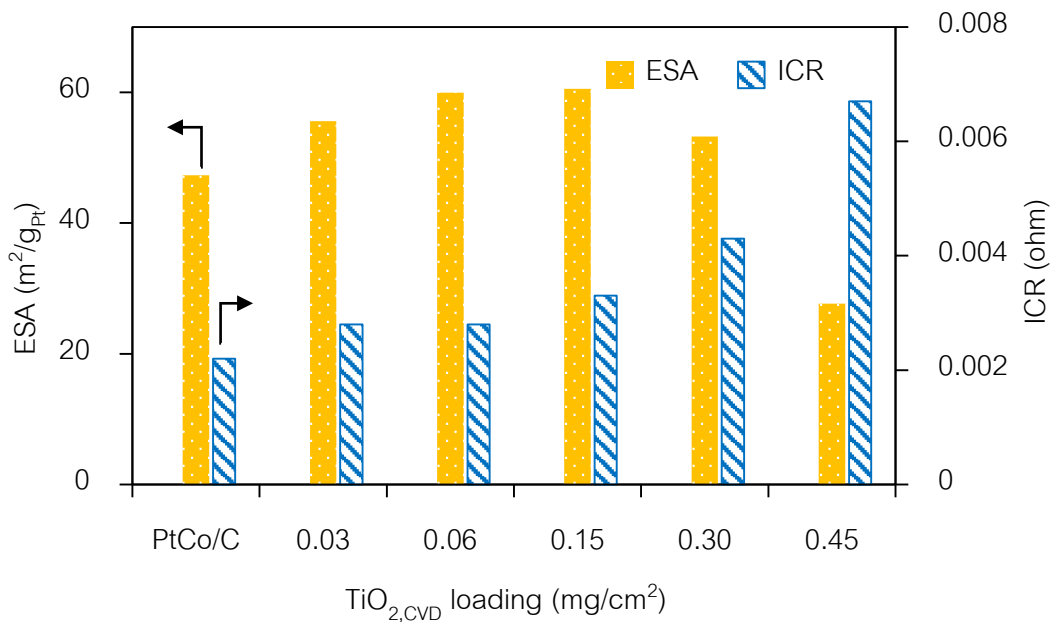


Figure 5. 7 Comparison of electrochemical surface area and interfacial contact resistance of $TiO_{2,CVD}$-PtCo/C electrodes with different loadings of $TiO_{2,CVD.}$

## 5.4 ORR activity of $TiO_{2,CVD}$-PtCo/C

The ORR activity of all $TiO_{2, CVD}$-PtCo/C catalysts were first tested in $O_2$-saturated 0.5 M $H_2SO_4$ using RDE at rotation rates between 500-2,000 rpm during a varying potential of -0.20 to 0.70 V and a constant sweep rate of 10 mV/s. The similar pattern of the voltammogram for the ORR was obtained for all $TiO_{2, CVD}$-PtCo/C catalysts as demonstrated in Figure 5.8. The curve can be divided into three distinct regions. The first region is a kinetics-controlled region, where the current density was not affected by the rate of mass transfer, and it is independent of the rotation rate ($\omega$). The second region is an intermediate region of mixed control where the current is partially controlled by mass transport and partially by the kinetics of electron transfer. The current increases with $\omega$, but not as a linear function of $\omega^{1/2}$. The last region is a diffusion-controlled region, which showed a well-defined limiting current plateau that increased linearly with $\omega^{1/2}$. The relationship between the current density and the rotation rate can be expressed by the Koutecky-Levich equation (Eq.(5.1)). This equation is valid for a first order process with respect to the diffusion species [80].

$$\frac{1}{j} = \frac{1}{j_k} + \frac{1}{B\omega^{1/2}} \tag{5.1}$$

and where $B$ is estimated by Eq. (5.2),

$$B = 0.62 n_e F D^{2/3} v^{-1/6} C \tag{5.2}$$

Here, $j_k$ is the kinetic current density, $\omega$ is the rotation rate, $n_e$ is the number of involved electrons, $F$ is the Faraday's constant (96,485 C/mol), $D$ is the diffusion coefficient of oxygen in solution (1.9 × 10$^{-5}$ cm$^2$/s), $v$ is the kinematics viscosity (0.01 cm$^2$/s) and $C$ is the oxygen concentration in the bulk solution (1.1 × 10$^{-6}$ mol/cm$^3$).
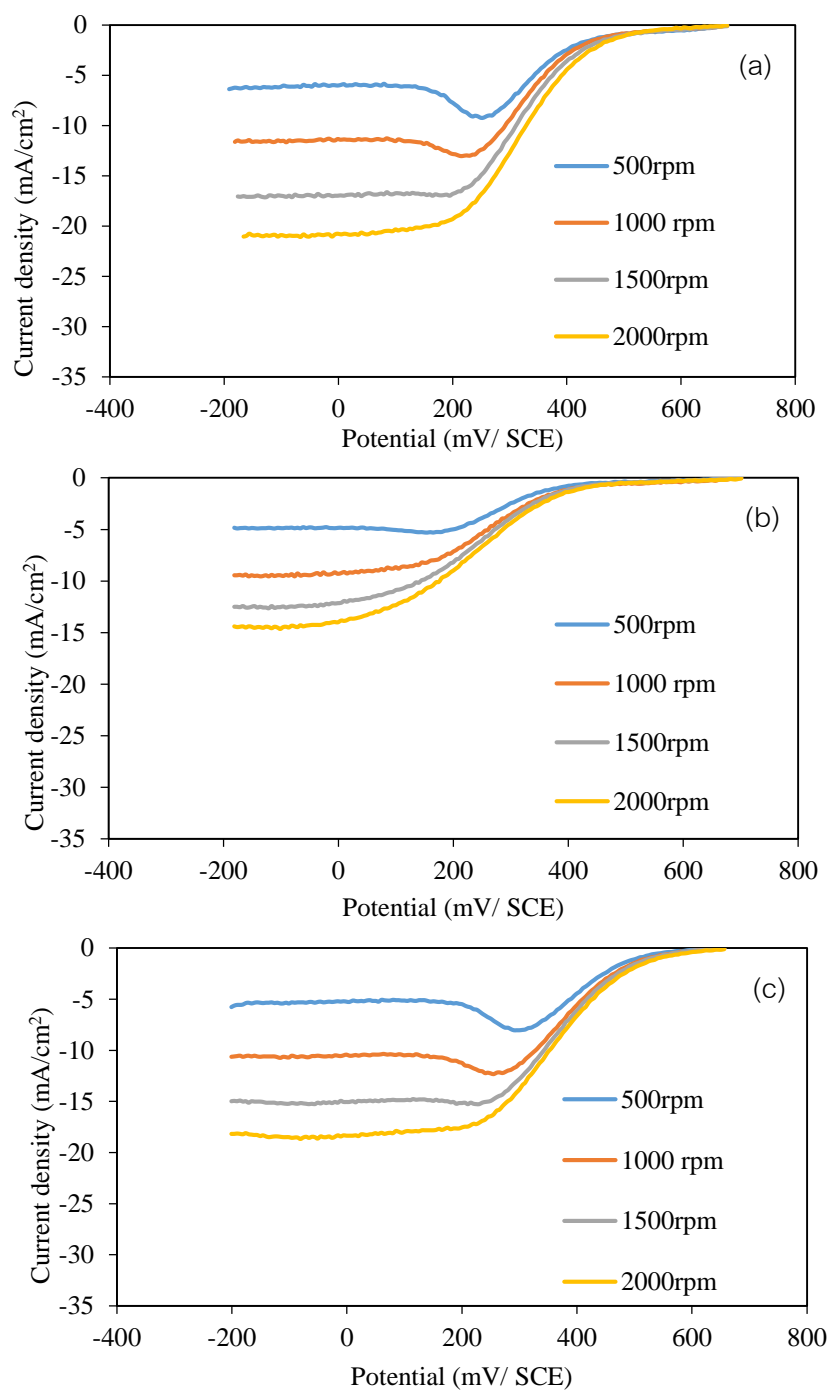
Figure 5. 8 Linear sweep voltammograms for the ORR in 0.5M $H_2SO_4$ (sat.$O_2$) with scan rate 10 mV/sec of the $TiO_{2,CVD}$-PtCo/C catalyst at different $TiO_{2,CVD}$ loadings of (a) 0.0, (b) 0.03, (c) 0.06, (d) 0.15, (e) 0.30, and (f) 0.45 mg/cm$^2$.

Figure 5.8 Linear sweep voltammograms for the ORR in 0.5M $H_2SO_4$ (sat.$O_2$) with scan rate 10 mV/sec of the $TiO_{2,\,CVD}$-PtCo/C catalyst at different $TiO_{2,CVD}$ loadings of (a) 0.0, (b) 0.03, (c) 0.06, (d) 0.15, (e) 0.30, and (f) 0.45 mg/cm$^2$(cont.).

The plot of $j^{-1}$ *vs.* $\omega^{-1/2}$ provided straight lines with the intercepts corresponding to the kinetic current density ($j_k$) and a slope of $1/B$ could be determined. Figure 5.9 shows the plot of kinetic current density of all $TiO_{2,\,CVD}$-PtCo/C catalysts. The increase in the ORR activity or $j_k$ was found to depend on the loading of $TiO_{2,CVD}$. Nevertheless, too high quantity of $TiO_{2,CVD}$ cannot enhance the ORR activity. Just a certain quantity of $TiO_{2,CVD}$ is required to promote the ORR activity. The highest ORR activity for PtCo/C catalayst was observed in the presence of $TiO_{2,CVD}$ at the loading of 0.06 $mg/cm^2$. The number of transferred electrons in the process via $TiO_{2,\,CVD}$-PtCo/C catalyst are between 3.97 and 4.05 with an average value of 3.99, suggesting that the ORR reaction occurred via the four-electron pathway.
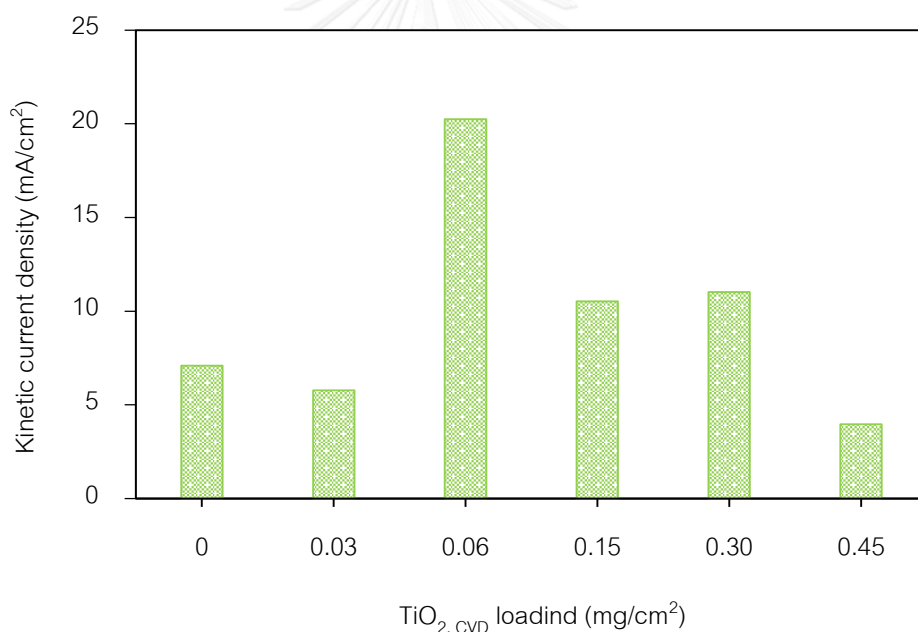


Figure 5. 9 Kinetically controlled ORR at 0.375 V versus SCE electrode for PtCo/C catalyst in the presence of different $TiO_{2,\,CVD}$ loadings.
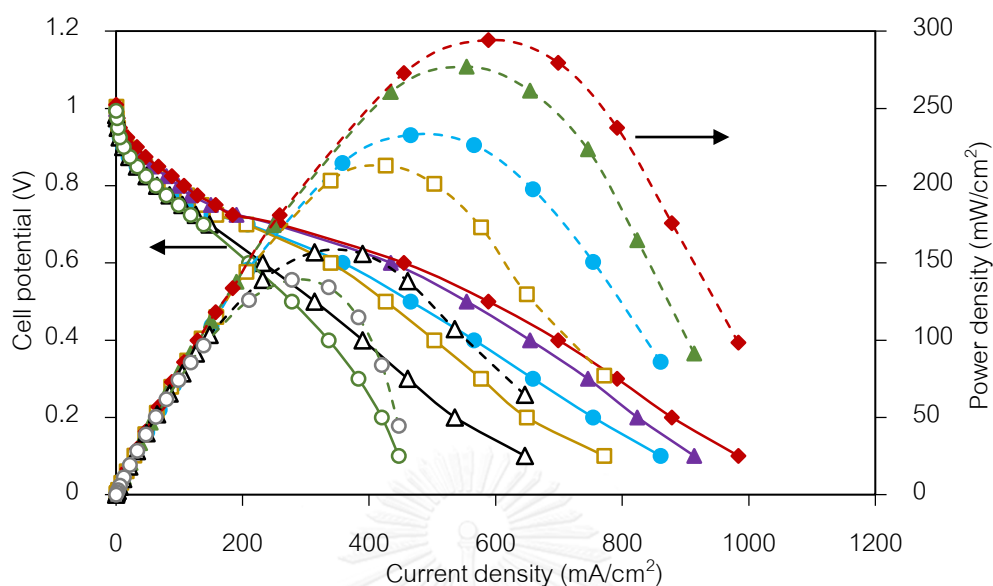
Figure 5. 10 Current density-potential curves of a single $H_2/O_2$ PEM fuel cell of the as-prepared $TiO_{2, CVD}$-PtCo/C catalyst at different $TiO_2$ loadings of ( ● ) 0.0, ( □ ) 0.03, ( ▲ ) 0.06, ( ◆ ) 0.15, ( △ ) 0.30 and ( ○ ) 0.45 mg/cm$^2$.

The catalytic activity of PtCo/C and $TiO_{2, CVD}$-PtCo/C for the ORR was then evaluated in a PEM fuel cell under $H_2/O_2$ atmosphere. All prepared catalysts were used in cathode side, while the commercial Pt/C (ETEK) was used as a catalyst for the HOR at the anode. The catalyst loading was fixed at 0.15 mg/cm$^2$. As demonstrated in Figure 5.10 and Table 5.3, the incorporation of appropriate $TiO_2$ content can promote the performance of PtCo/C catalyst. The reason for an improved Pt utilization and fuel cell performance was probably due to an increasing of a percolating electron-conducting network of $TiO_2$ loading, which resulted in an enhanced macroscopic electronic conductivity in the GDE as showed in Figure 5.7. Among all $TiO_{2, CVD}$-PtCo/C catalyst, the PtCo/C with 0.15 mg/cm$^2$ $TiO_2$ exhibited the highest performance compared with other PtCo/C catalysts. Further raising the $TiO_2$ greater than 0.15 mg/cm$^2$ decreased the performance in fuel cell importantly, probably due to limited macroscopic electronic conductivity. This is because

a sufficiently high macroscopic electronic conductivity can be assumed in the $Pt-TiO_2/C$ composite electrodes when 50 vol% carbon is present [104].

Table 5. 3 Summary of the electrochemical evaluation on all $TiO_{2, CVD}$-PtCo/C catalysts.

| Sample | $TiO_2$,CVD loading (mg/cm$^2$) | $j_{0.9 V}$ (mA/cm$^2$) | $j_{0.6 V}$ (mA/cm$^2$) |
|---|---|---|---|
| Pt-Co/C | 0 | 11.2 | 358 |
| $TiO_{2, CVD}$-PtCo/C | 0.03 | 16.8 | 339 |
| | 0.06 | 22.8 | 434.4 |
| | 0.15 | 33.0 | 454.8 |
| | 0.30 | 11.4 | 231.8 |
| | 0.45 | 11.2 | 210 |

# CHAPTER 6
## ORR activity and stability of TiO$_2$-PtCo/C catalysts in PEM fuel cell

In chapter IV and V, the result showed that PtCo/C catalyst with commercial TiO$_2$ (TiO$_{2,com}$-PtCo/C) at loading of 0.06 mg/cm$^2$ had the highest performance for PEM fuel cell, while the PtCo/C catalyst with TiO$_2$ prepared by CVD technique (TiO$_{2,CVD}$-PtCo/C) gave the highest performance at TiO$_2$ loading of 0.15 mg/cm$^2$. In this chapter, we will compare activity and stability of TiO$_{2,com}$-PtCo/C and TiO$_{2,LPCVD}$-PtCo/C catalyst. The activity was determined both in acid solution and in PEM fuel cell under H$_2$/O$_2$ environment. Moreover, the stability of PtCo/C, TiO$_{2,com}$-PtCo/C and TiO$_{2,CVD}$-PtCo/C catalyst was studied. The obtained results are shown as the following.

## 6.1 Morphology of TiO$_2$-PtCo/C electrode

Figure 6.1 displays the XRD patterns of the sublayer coated-gas diffusion layer (sGDL), TiO$_{2,COM}$ and TiO$_{2,CVD}$ deposited on sGDL. The XRD pattern of sGDL exhibited two broad peaks at 2$\theta$ of 25.27$^\circ$ and 42.87$^\circ$ associating with the hexagonal plane of carbon at planes of C[002] and C[101] (JCP-001-0646), respectively. Both peaks at the same 2$\theta$ were also observed for both types of TiO$_2$ coated on sGDL but with the sharp-end for a peak at 2$\theta$ of 25.27$^\circ$. This might be attributed to the intersection between a peak C[002] of carbon and peak A[101] of TiO$_2$ in anatase phase (JCP-002-0606). Also, the XRD pattern of both TiO$_2$ revealed the peak at 2$\theta$ of 48.05$^\circ$, assigning to the peak of A[200] (JCP-002-0606). Besides, a characteristic peak of rutile phase at a 2$\theta$ of 53.99$^\circ$, corresponding to the R[211] planes (JCP-001-1292) was also observed for TiO$_{2,COM}$. This suggests that the phase of TiO$_{2,COM}$ was a mixture of both anatase and rutile phases, while the phase of TiO$_{2,CVD}$ was only the anatase phase. The particle size, estimated from the

peak at $2\theta$ of 48.05$^\circ$ according to the Debye-Scherrer equation [105], of TiO$_{2,COM}$ was around 38.66 nm, close to that of TiO$_{2,CVD}$ (37.82 nm).
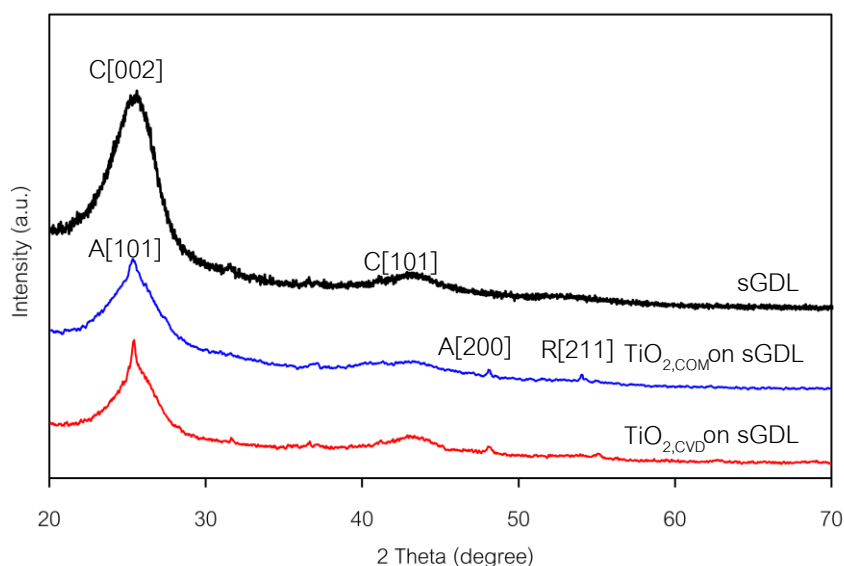


Figure 6. 1 Representative XRD patterns of TiO$_{2,COM}$ and TiO$_{2,CVD}$.

The XRD spectra of PtCo/C catalysts on GDL also demonstrated peak during $2\theta$ between 20$^\circ$ and 30$^\circ$ of carbon substrate. However, a broad sharp-end peak was observed for the TiO$_2$-PtCo/C catalyst at the same $2\theta$ range (Figure 6.2). This is attributed to the intersection between the diffraction peaks of hexagonal carbon substrate and the crystal plane of A[101] of TiO$_2$. Besides, the spectrum of PtCo/C exhibited the main characteristic peaks of the face-center cubic (FCC) structure of crystalline Pt[111] at $2\theta$ of 40.01$^\circ$ [16]. The *d*-spacing of all the supported PtCo/C catalysts was smaller than that of the pure Pt/C catalyst (Table 6.1), indicating a contraction of the Pt lattice, due to the particle substitution of Pt by Co in the FCC structure [106] or the formation of the PtCo alloy. In the presence of TiO$_2$, the XRD pattern of the TiO$_2$-PtCo/C catalyst still exhibits the diffraction peaks of FCC Pt, and the diffraction peaks of TiO$_2$ at about 25.27$^\circ$ and 48.05$^\circ$ are well presented in the TiO$_{2,CVD}$-PtCo/C catalyst. The diffraction peaks of Pt were also noticed in this catalyst at $2\theta$ of 40.01$^\circ$. The crystallize sizes of both TiO$_2$-PtCo/C catalyst

were slightly smaller than that of PtCo/C (Table 6.1). The ratio of Pt and Co was close to the set value of 1: 1. When either $TiO_{2,COM}$ or $TiO_{2,CVD}$ were coated on the PtCo/C catalyst layer, a uniform distribution of metal along the electrode surface was observed for all types of catalysts (Figure 6.3). The EDX spectrum revealed the presence of metal elements including Pt, Co and Ti on the electrode surface (Figure 6.3).

Table 6. 1 Morphology of fresh PtCo/C, $TiO_{2,COM}$ -PtCo/C and $TiO_{2,CVD}$-PtCo/C catalysts

| Catalysts | $d$-spacing ($A°$) | Crystallize size (nm) | Pt : Co (wt ratio) | ESA ($m^2$/gPt) | Contact angle (degree) | Corrosion current density ($j_{corr}$) |
|---|---|---|---|---|---|---|
| Pt/C | 2.26 | | | | | |
| PtCo/C | 2.22 | 9.4 | 52:48 | 55.3 | 88.7 | 13.7 |
| $T_{COM}$-PtCo/C | 2.22 | 9.5 | 51:49 | 79.6 | 35.9 | 8.2 |
| $T_{CVD}$-PtCo/C | 2.22 | 9.3 | 55:45 | 121 | ∼ 0 | 4.5 |
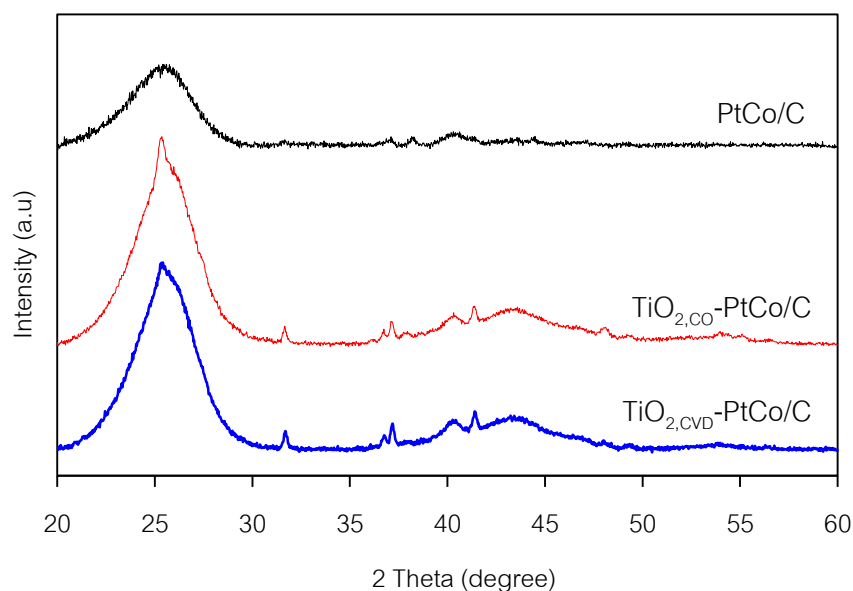


Figure 6. 2 XRD patterns of fresh PtCo/C and $TiO_2$-PtCo/C catalysts.
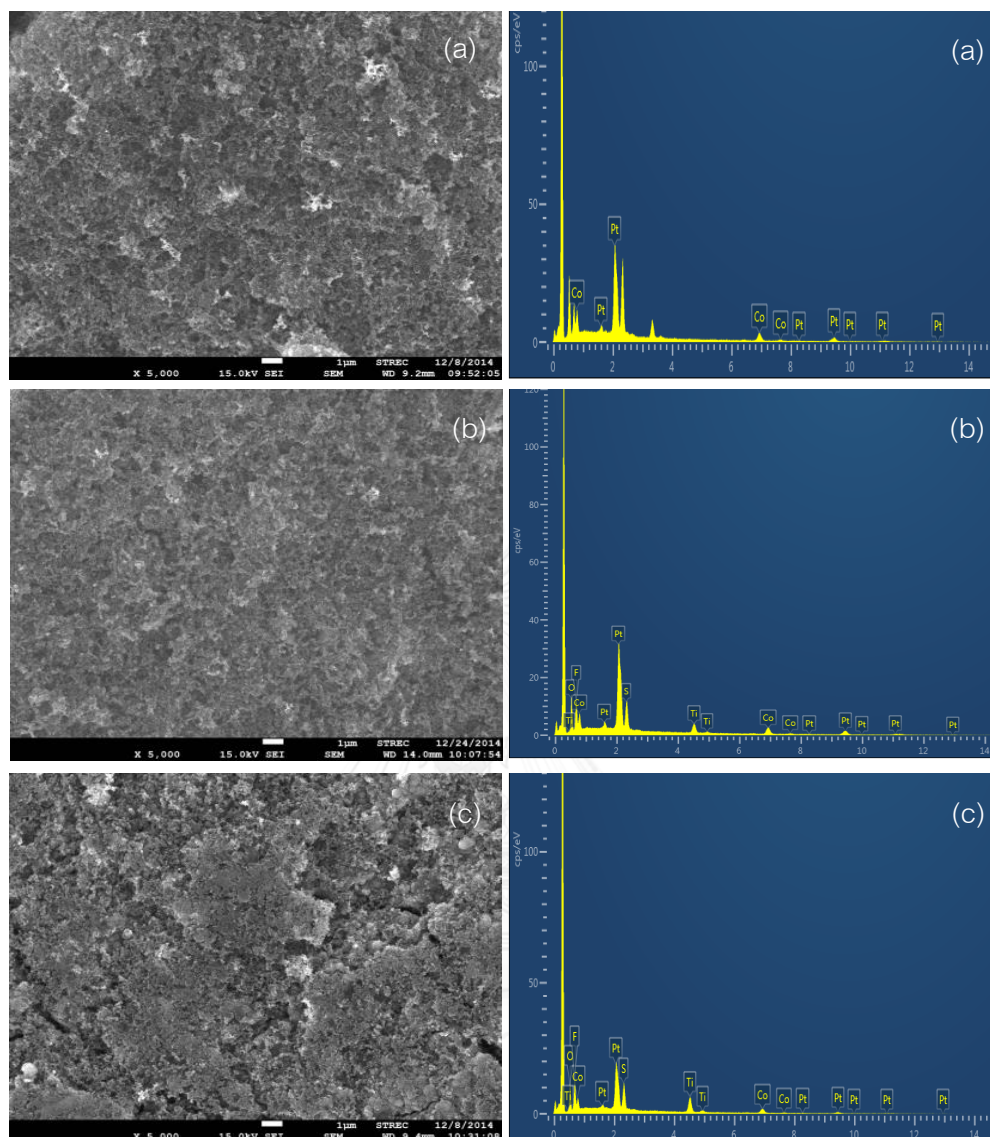
Figure 6. 3 SEM micrographs of crystalline particles and EDX spectra of fresh catalysts:

(a) PtCo/C, (b) TiO$_{2,COM}$-PtCo/C and (c) TiO$_{2,CVD}$-PtCo/C catalyst.

## 6.2 Electrochemical property of prepared $TiO_{2,CVD}$ and $TiO_{2,com}$-PtCo/C catalysts

Regarding the ESA of $TiO_2$ and $TiO_2$-PtCo/C, the magnitude of hydrogen desorption area was observed as the order of $TiO_{2,CVD}$-PtCo/C > $TiO_{2,com}$-PtCo/C > PtCo/C catalysts (Figure 6.3), suggesting that the maximum ESA was ranked in the order of $TiO_{2,CVD}$-PtCo/C > $TiO_{2,com}$-PtCo/C > PtCo/C catalysts (Table 6.1). The presence of $TiO_2$ in the catalyst layer can enhance an increase of ESA compared with that in the absence of $TiO_2$, probably due to the increase of electrode roughness in the presence of $TiO_2$ [107]. Moreover, either pure $TiO_{2,COM}$ or $TiO_{2,CVD}$ can participate in the $H_{upd}$ adsorption/desorption reaction as shown as the insert of Figure 6.4. A higher hydrogen desorption area was observed for $TiO_{2,CVD}$ than that of $TiO_{2,COM}$, resulting in a high ESA of the $TiO_{2,CVD}$-PtCo/C catalyst.
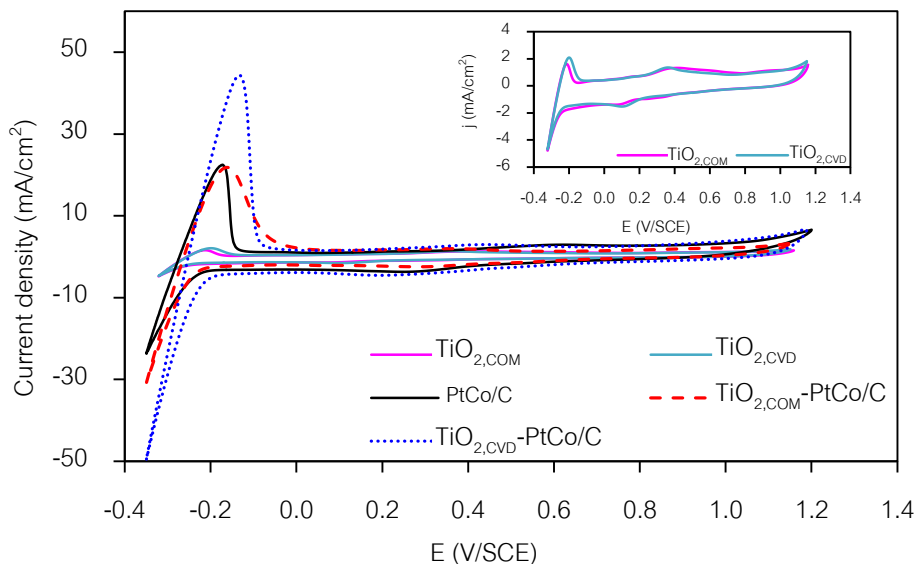


Figure 6. 4 Representative cyclic voltammetery of PEM fuel cells with pure $TiO_2$ and fresh $TiO_2$-PtCo/C catalysts in 0.5 M $H_2SO_4$ ($N_2$ sat.) at scan rate of 20 mV/s.

## 6.3 Activity of $TiO_2$-PtCo/C catalysts

The activity of all three PtCo/C catalysts was then tested in a single PEM fuel cell under $H_2/O_2$ at atmospheric pressure and temperature of 60 $^{o}$C. As clearly seen in Figure 6.5, the $TiO_{2,CVD}$-PtCo/C exhibited the highest current density (20.5 mA/cm$^2$) compared with that of $TiO_{2,COM}$-PtCo/C (12.6 mA/cm$^2$) and PtCo/C (10.1 mA/cm$^2$) catalysts at 0.9 V. It also exhibited the highest current density (434 mA/cm$^2$) as well as power density (277 mW/cm$^2$) at 0.6 V during the medium-through-high current density region. This suggests that the $TiO_{2,CVD}$-PtCo/C catalyst had the highest activity in the PEM fuel cell, probably attributed to its highest ESA as well as its hydrophilic property (Table 6.1) measured in terms of water contact angle. Although $TiO_2$ has low electrical conductivity compared to the carbon support and metal catalysts, which could reduce the electrical conductivity of the catalyst layer, it can improve the hydrophilic properties of the catalyst layer in fuel cells as well as prevent the drying out of the membrane, which results in an increasing proton conductivity as well as decreasing ohmic resistance in actual operation.
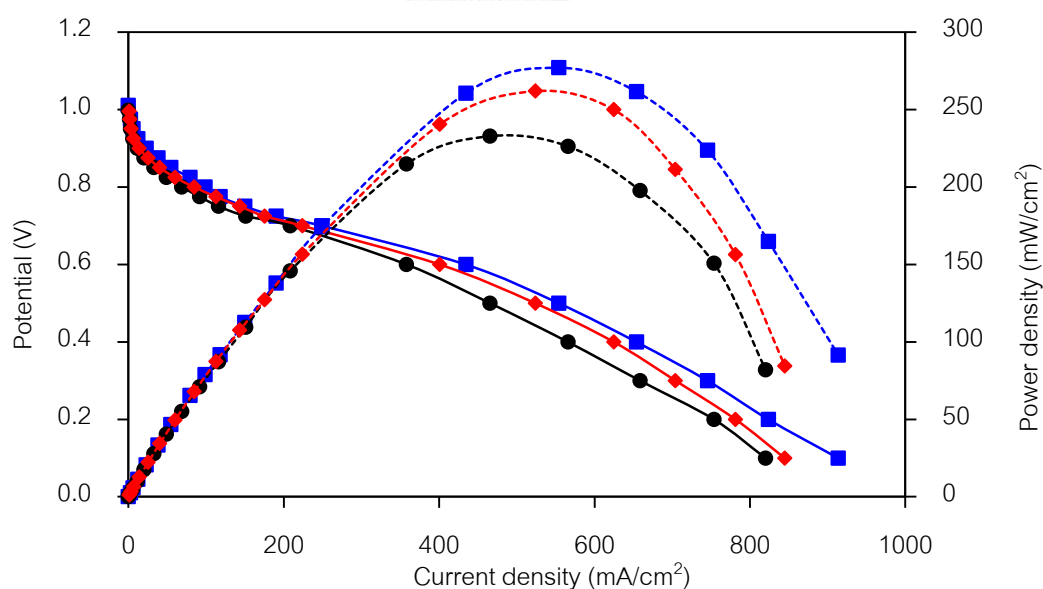


Figure 6. 5 Current density-potential curves of the as-prepared (●) PtCo/C, (◆)$TiO_{2,COM}$-PtCo/C and (■)$TiO_{2,CVD}$-PtCo/C catalysts in a single $H_2/O_2$ PEM fuel cell.

This is also supported by previous work which reported that the oxygen atom could be adsorbed on the $TiO_2$ surface in the similar adsorbed state as Pt surfaces [6, 108], suggesting that the addition of $TiO_2$ on the surface of catalyst layer can also enhance the ORR activity of PtCo/C catalyst.

## 6.3 Stability of $TiO_2$-PtCo/C catalysts

To test the stability of all prepared catalysts, the repetitive LSV was conducted in 0.5 M $H_2SO_4$. Figure 6.6 shows example plots obtained from the stability test of the $TiO_{2,CVD}$-PtCo/C catalyst at particular LSV cycles. A well-defined polarization curve for oxygen reduction with the thin film electrode fabrication was observed for all repetitive cycles (Figure 6.6(a)). The value of the limiting current ($j_L$), the maximum current density occurs when the concentration of reactant species at the electrode surface becomes zero, obtained from this plot can be used to determine the ORR performance [109-111].The limiting current ($j_L$) increased during the first 2,000 LSV-cycles and decreased importantly when the testing cycle was prolonged to 8,000 cycles.

The complex plane representation obtained from the EIS measurement after the particular LSV cycle is demonstrated in Figure 6.6(b). Linear spectra originating from the x-axis with positive slope value deviating from $45^{\circ}$ were observed, suggesting that this system comprised two circuit elements, resistance (R) and constant phase element (CPE) [112]. With this electrochemical configuration, the obtained resistance is the electrolyte resistance ($R\Omega$), which could be used to monitor the variation of electrolyte conductivity. A low value of $R\Omega$ exhibited a high electron conductivity of the electrolyte. From the plot, it seems to be that the value of $R\Omega$ decreased with increasing repetitive LSV cycles.

For the CV measurement (Figure 6.6(c)), a fresh $T_{CVD}$-PtCo/C catalyst exhibited only a clear hydrogen desorption peak at a potential of -0.18 V/SCE. After repetitive LSV cycles were conducted, an adsorption peak of the oxygen atom on the catalyst surface (Pt-O) was observed at +0.39 V/SCE after 1,000 LSV-cycles (peak I). The downfield shift of the reduction potential was observed as increasing repetitive LSV cycles, probably due

to the accumulation of an electronic charge on the electrocatalyst-electrolyte interface and the formation of a high double-layer charging current, due to a strongly adsorbed hydride as well as oxide layers on the catalyst surface [112]. High intensity of hydrogen adsorption (region II)/desorption peak (region III) with a more pronounced peak segregation to Pt[100] and Pt[110] was observed as the increasing repetitive LSV cycle. This suggests an increase of ESA as well as an alternation of crystalline structure of the Pt catalyst. The intensity of the oxide formation peak (Pt-OH and then Pt-O, region IV) also increased with the increase of the LSV cycles.

Figure 6.7 sumarizes the variation of normalized $j_L$, $R\Omega$ and nomalized ESA as a functoin of repetitive LSV cycles in 0.5 M $H_2SO_4$. The normalized $j_L$ of the PtCo/C catalyst decreased drastically after the beginning of the stability test. The semilar variation trend of normalized $j_L$ was observed for both $TiO_{2,COM}$-PtCo/C and $TiO_{2,CVD}$-PtCo/C catalysts (Figure 6.7(a)). They increased during the early period of the LSV cycles to reach their maximum value (1.0) at 2,000th LSV-cycle and then drop drastically, suggesting the start up of catalyst degradation after the 2,000 LSV-cycle. Importantly, the drop of normalized $j_L$ of the PtCo/C catalyst was low pronounced in the presence of $TiO_2$, probably due to an excellent corrosion resistance property of $TiO_2$ both in acid and alkaline environments [113-114]. This could be confirmed by the Tafel plot as shown in Figure 6.8. The corrosion current density of $TiO_{2,COM}$ and $TiO_{2,CVD}$ were 0.515 and 0.095 mA/cm$^2$, lower than that of sGDL of 0.12 and 0.68-fold, respectively. When they were incorporated on the PtCo/C catalyst layer, they can reduce the corrosion current density of PtCo/C catalyst significantly. Namely, the corrosion current density of PtCo/C catalyst was reduced from 13.7 mA/cm$^2$ to 8.2 and 4.5 mA/cm$^2$, when $TiO_{2,COM}$ and $TiO_{2,CVD}$ were respectively added on the PtCo/C catalyst (Table 6.1). The $TiO_{2,CVD}$ can promote a more corrosion resistance of PtCo/C catalyst than $TiO_{2,COM}$, probably due to the different $TiO_2$ incorporation technique into the sGDL. The incorporation of $T_{COM}$ by direct spray might provide a non-adhesive $TiO_2$ layer on the sGDL, while the CVD technique induced under high temperature and low pressure (350 $^{\circ}$C and 0.026 atm) could enhance the adhesion with a carbon layer providing an impregnable $TiO_2$ layer.
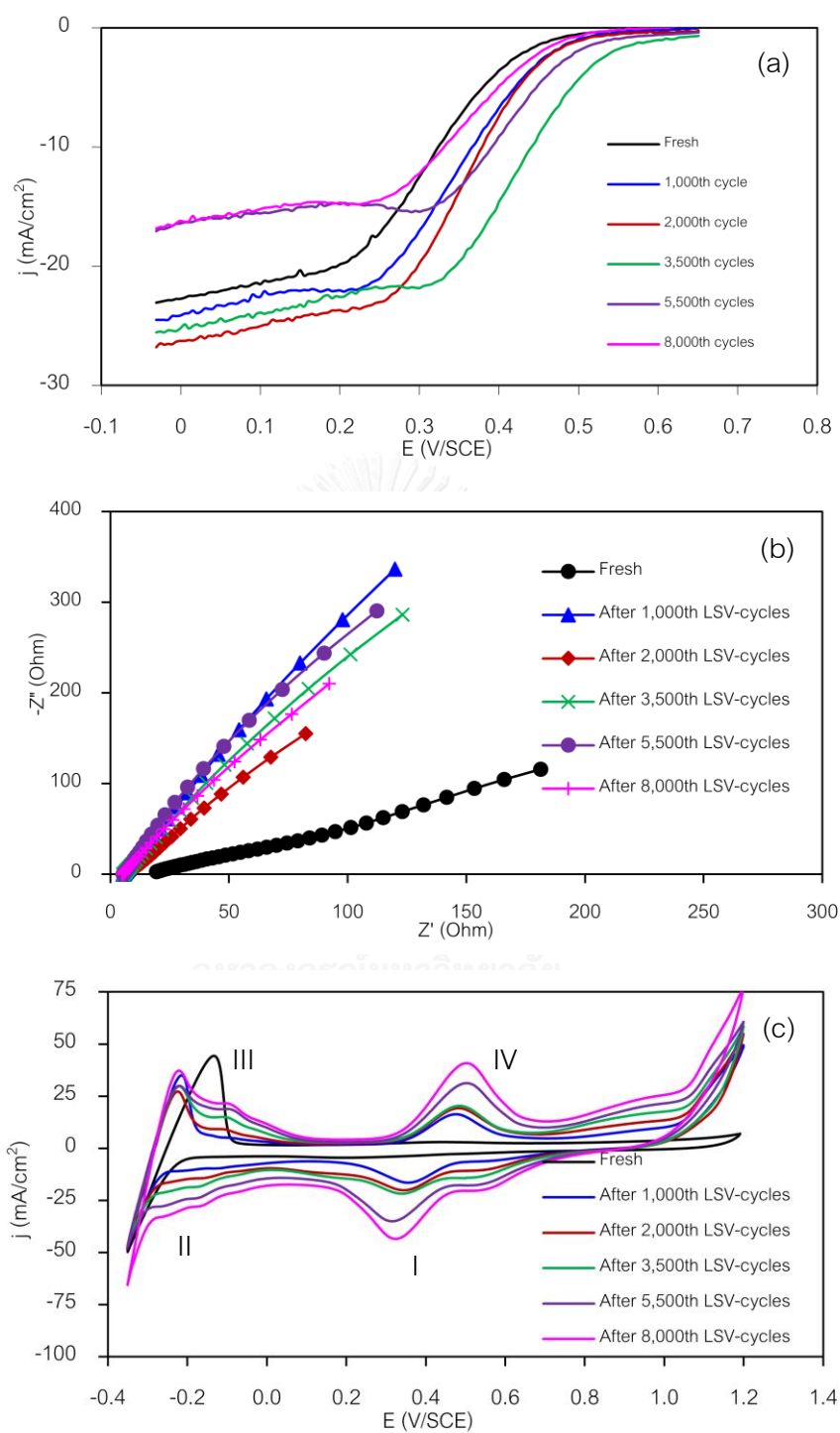
Figure 6. 6 Example plot of stability test for $TiO_{2,CVD}$-PtCo/C catalyst obatined from (a) LSV, (b) EIS and (c) CV measurement in 0.5 M $H_2SO_4$.
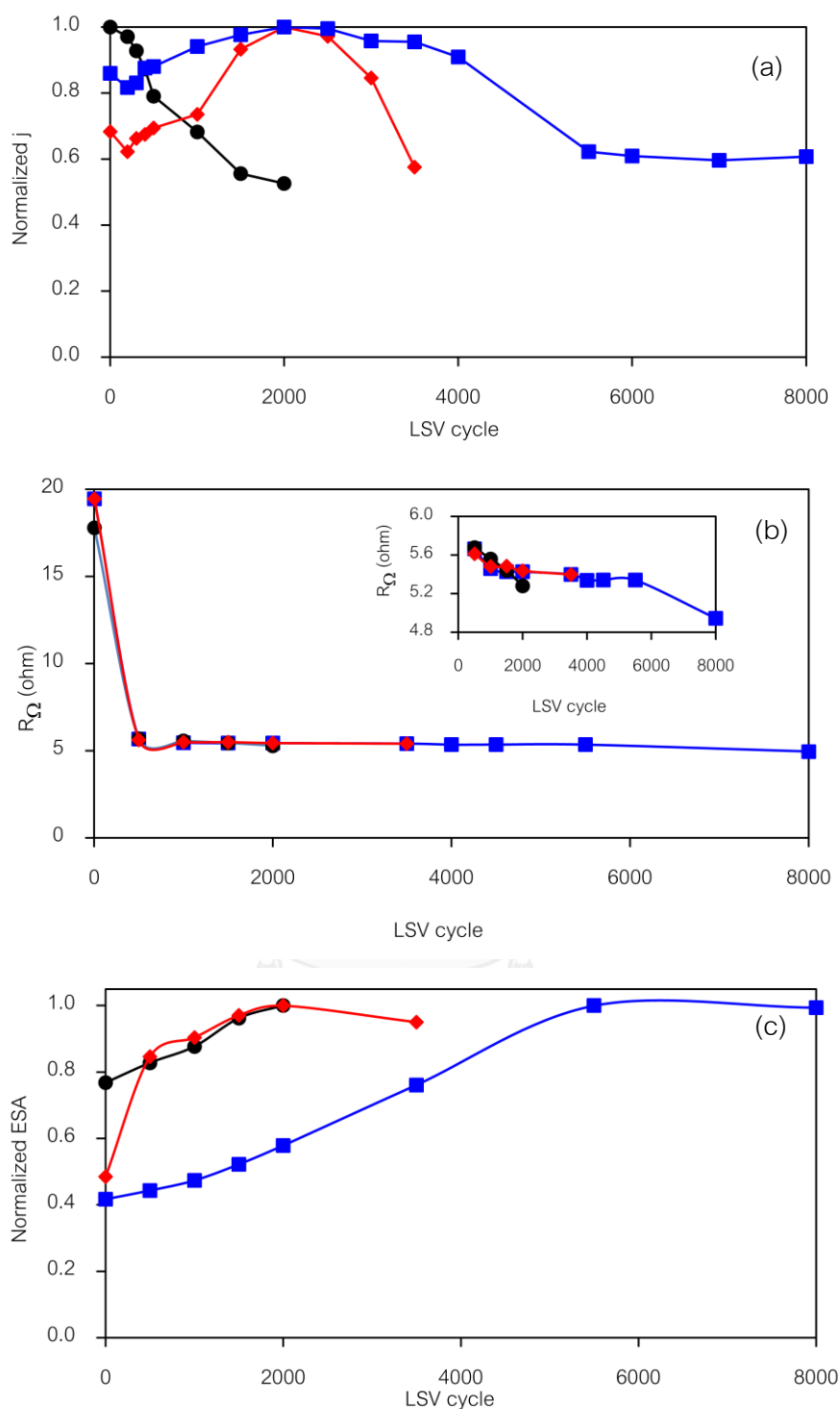
Figure 6. 7 Variation of (a) limiting current ($j_L$), (b) ohmic resistance and (c) ESA of (●) PtCo/C, (◆)TiO$_{2,COM}$-PtCo/C and (■)TiO$_{2,CVD}$-PtCo/C catalysts during the stability test by repetitive LSV in 0.5 M H$_2$SO$_4$.

Regarding the alternation of the $R\Omega$ value with the increasing repetitive LSV cycle, the drastically decreasing $R\Omega$ was observed after the 500th-LSV cycle for all prepared catalysts (Figure 6.7(b)), suggesting an increase in electrical conductivity of the acid electrolyte. This is probably due to the dissolution of the metal catalyst into the electrolyte. As the LSV cycles increased to greater than 500 cycles, a slight decrease of $R\Omega$ of all prepared catalysts was observed. More d ecrease of $R\Omega$ was observed for the PtCo/C catalyst, suggesting increased electrolyte conductivity, or in other words, more metal dissolution into the acid electrolyte than other prepared catalysts, which is agreeable with the corrosion rate as listed in Table 6.1 and Figure 6.8.
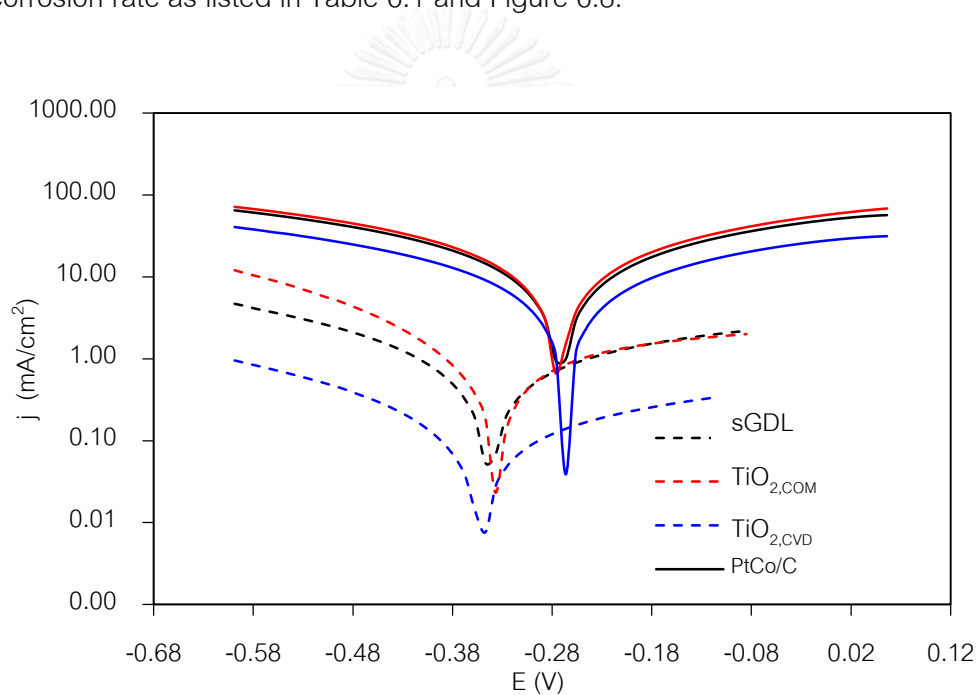


Figure 6. 8 Tafel plot of PtCo/C and $TiO_2$-PtCo/C catalysts in 0.5 M $H_2SO_4$.

With regard to ESA, the normalized ESA of all prepared catalysts increased noticeably with increasing repetitive LSV cycles to reach the maximum value (1.0) and then dropped afterward with the prolonged LSV cycles (Figure 6.7(c)). The increase of ESA during the early period of the LSV cycles was probably due to the initial wetting behavior of the thin Nafion layer covering the catalyst particles [109]. The maximum ESA of the $TiO_{2,COM}$- PtCo/C catalyst was found at 2,000[th] LSV-cycles, corresponding to the

maximum $j_L$. However, the ESA of the $TiO_{2,CVD}$-PtCo/C catalysts still increased and reached the maximum value at 5,000[th] LSV-cycles, which was inconsistent with the variation of $j_L$. The increasing tendency of ESA after stability tests previously showed that the $H_{upd}$ adsorption/desorption on the Pt surface is more improved for age surfaces than fresh surfaces due to the dissolution of Co [115]. Thus, the presence of a high quantity of Co atoms at the near-surface region deducted the $H_{upd}$ charge density [116-117]. As shown in Figure 6.9, the XRD peaks shifted to a low angle closer to the pure Pt peak while no $TiO_2$ peaks were observed, indicating the loss of alloy property as well as $TiO_2$ elements during the stability test. Furthermore, their $d$-spacing was close to that of pure Pt, and the crystallize size of all catalysts increased around 1.2-fold after the stability test (Table 2). To prove this hypothesis, the metal composition of all prepared catalysts after the stability test was again measured. As demonstrated in Table 6.2 and Figure 6.10, all prepared catalysts after the stability test lost Co and Ti contents from their structures, resulting in an increase of ESA with increasing repetitive LSV cycles. The inconsistent trend between the ESA and $j_L$ might be attributed to the change of catalyst morphology after the stability test. This is due to the catalyst agglomeration as confirmed by the SEM images (Figure 6.10), owing to the carbon-support loss and Ostwald ripening [118-120]. The dissolution behavior of metal elements from Pt-M alloy under the 0.5 M $H_2SO_4$ solution was already proved and explained elsewhere [7, 118]. That is, the M atoms at the first top layer will dissolve, and Pt atoms will diffuse on the surface and accumulate to form a cluster on the surface. Finally, the surface of the Pt alloy will become completely covered with Pt atoms, which is consistent with this study's results.

Based on the obtained results, although all prepared PtCo/C catalysts lost their stability after testing in 0.5 M $H_2SO_4$ using the LSV, catalyst deterioration was ranked as the order of PtCo/C > $TiO_{2,COM}$-PtCo/C > $TiO_{2,CVD}$-PtCo/C. Approximately 40% of performance loss was observed for PtCo/C, $TiO_{2,COM}$-PtCo/C and $TiO_{2,CVD}$-PtCo/C after 1,300, 3,300 and 6,000 LSV-cycles. This suggests that a home-prepared $T_{CVD}$ can enhance the stability and durability of PtCo/C catalyst due to its excellent corrosion resistance property and its preparation/incorporation technique.

Table 6. 2 Morphology of PtCo/C, $TiO_{2,COM}$-PtCo/C and $TiO_{2,CVD}$-PtCo/C catalysts after stability test by repetitive LSV for 2,000, 3,500 and 8,000 cycles, respectively.

| Catalysts | $d$-spacing (A°) | Crystallize size (nm) | Pt : Co ratio (wt. ratio) | ESA ($m^2/g_{Pt}$) |
|---|---|---|---|---|
| PtCo/C | 2.28 | 11.6 | 100:0 | 114 |
| $T_{COM}$-PtCo/C | 2.27 | 11.4 | 100:0 | 93.9 |
| $T_{CVD}$-PtCo/C | 2.27 | 11.1 | 100:0 | 110 |
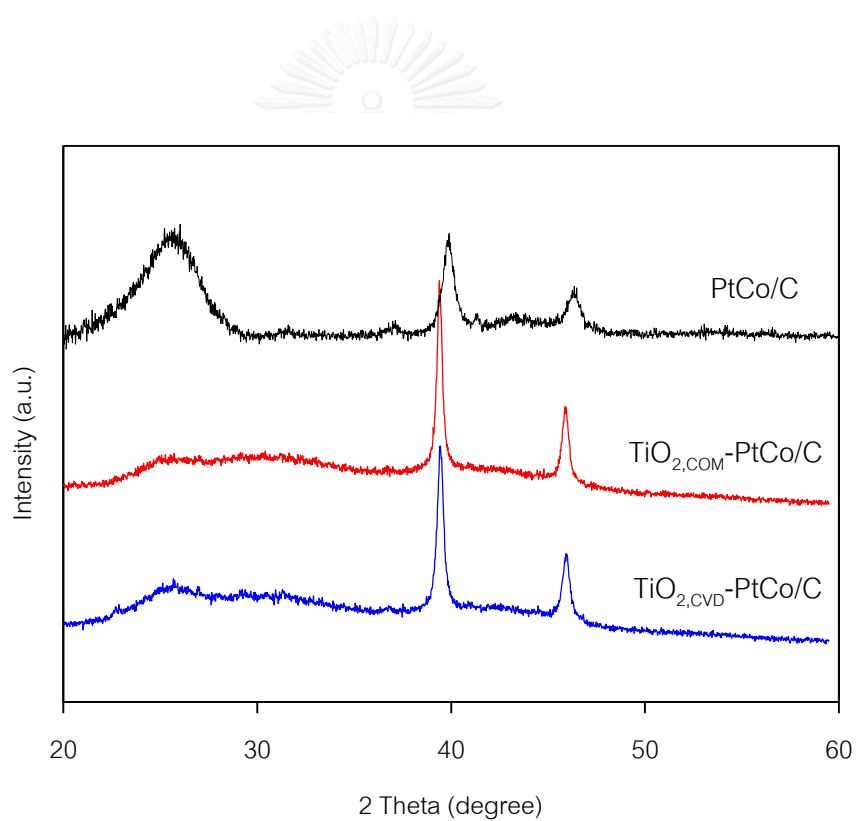


Figure 6. 9 XRD patterns of PtCo/C, $TiO_{2,com}$-PtCo/C, and $TiO_{2,CVD}$-PtCo/C catalysts after stability test by repetitive LSV for 2,000, 3,500 and 8,000 cycles, respectivel
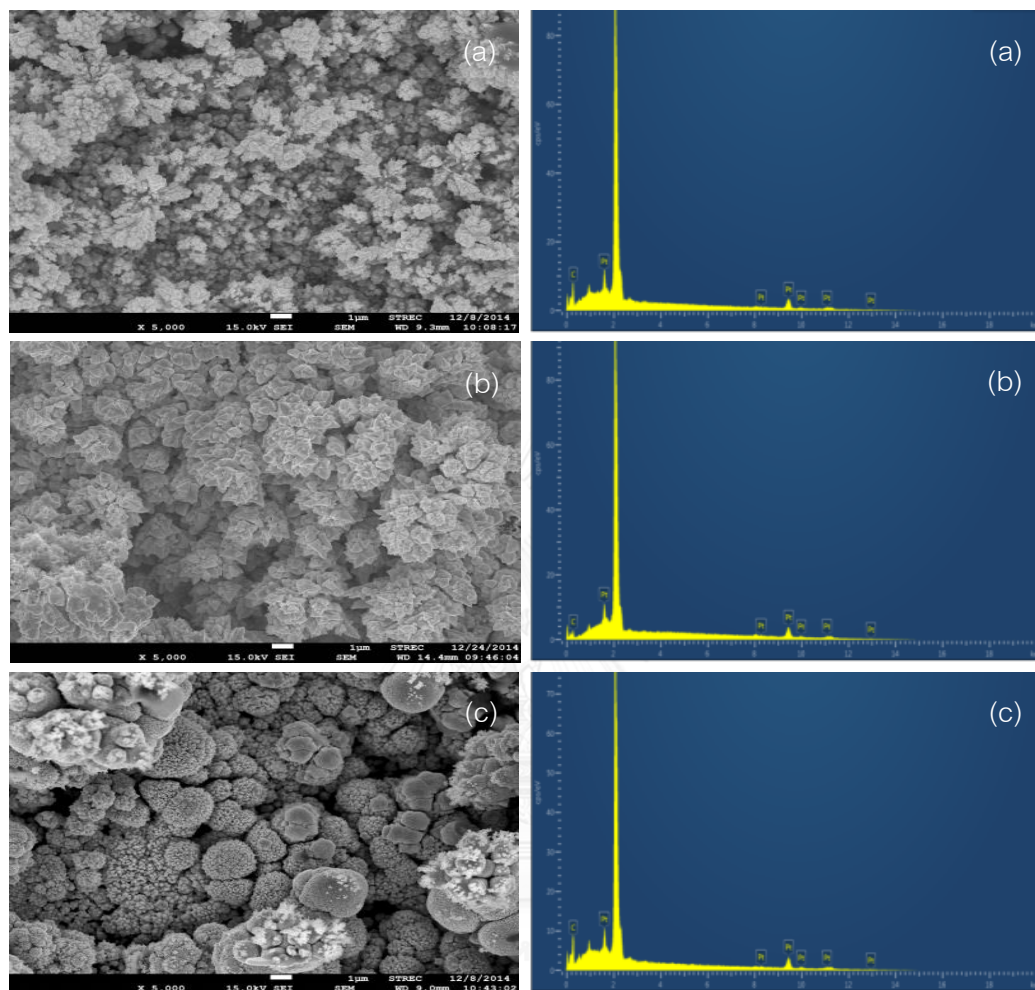
Figure 6. 10 SEM micrographs and EDX spectra of crystalline particles of catalyst after stability test: (a) PtCo/C, (b) $TiO_{2,COM}$-PtCo/C and (c) $TiO_{2,CVD}$-PtCo/C catalysts.

CHAPTER 7

Conclusions and Recommendations


7.1 Conclusions


Part 1: Effects of metal oxide ($CeO_2$, $MoO_2$, and $TiO_2$) on activity and stability of PtCo/C catalyst.

Three types of metal oxides including $CeO_2$, $MoO_2$ and $TiO_2$ were incorporated as the interlayer of PtCo/C catalysts at different loadings. The results demonstrated that incorporation of those metal oxides had insignificant effect on either crystalline size or $d$-spacing of the PtCo/C catalyst. However, they have a significant effect on the ESA and ICR. Addition of $CeO_2$ and $MoO_2$ affected negatively the ESA and ICR as well as the hydrophilic/hydrophobic property of the PtCo/C catalyst. The addition of $TiO_2$ at appropriate loading can enhance an increase of ESA as well as the decrease of ICR of the PtCo/C catalyst. Moreover, it can help to manage the water in the catalyst layer. The PtCo/C catalyst with $TiO_2$ of 0.06-0.15 mg/cm$^2$ can produce a maximum power density of 305 mW/cm$^2$ with a loss of around 20% of ESA after the repetitive potential cycling of 200 cycles.

Part 2: Effects of $TiO_2$ phases on activity of PtCo/C catalyst.

The interlayer of either $TiO_2$ phases rutile or mixed phase (anatase-rutile) on PtCo/C catalysts at different loadings did not affect the alloy properties, structure, and morphology of the PtCo/C catalyst layer, but affected on the ESA and the ORR activity. The PtCo/C catalyst with $TiO_2$ in mixed phase had significant effect on the PEM fuel cell performance in middle to high voltage than that of PtCo/C catalyst with $TiO_2$ in rutile phase.

Part 3: ORR activity of PtCo/C catalyst in the presence of $TiO_2$ layer prepared by chemical vapor deposition.

In the preparation process, the size of $TiO_2$ layer, which was prepared by low-pressure chemical vapor, was controlled by the precursor concentration and deposition temperature. The selected preparation conditions were precursor concentration at 0.05 M and deposition temperature at 350 °C. The $TiO_2$ loadings was varied by deposition time. After incorporated with PtCo/C catalyst, it did not change the structure and morphology of PtCo/C catalyst but it could promote the ESA and kinetic current density of PtCo/C catalyst. The ESA, ORR activity and performance of PEM fuel cells were characterized at different $TiO_2$ loadings (0.03 mg/cm$^2$, 0.06 mg/cm$^2$, 0.15 mg/cm$^2$, 0.30 mg/cm$^2$ and 0.45 mg/cm$^2$ on GDLs). The PtCo/C catalyst with $TiO_2$ layer at $TiO_2$ loading of 0.06 mg/cm$^2$ gave the highest ESA, ORR activity and PEM fuel cell performance with 59.98 m$^2$/g$_{Pt}$, 20.24 mA/cm$^2$ and 460.8 mA/cm$^2$ at PEM fuel cell operating potential 0.6V, respectively.

Part 4: ORR activity and stability of $TiO_2$-PtCo/C catalysts

The comparative study of PtCo/C catalyst activity and stability in the presence of different types of $TiO_2$ ($TiO_{2,COM}$ and $TiO_{2,CVD}$) was explored in PEM fuel cells and an acid electrolyte (0.5 M $H_2SO_4$). Both $TiO_2$ ($TiO_{2,COM}$ and $TiO_{2,CVD}$) had a similar particle size, but in different phases. The $TiO_{2,COM}$ was in a mixed phase of rutile and anatase, while $TiO_{2,CVD}$ was in a pure anatase. When both were incorporated on the PtCo/C catalyst, the $TiO_{2,CVD}$-PtCo/C catalyst exhibited higher ESA and super hydrophilic property compared with the PtCo/C and $TiO_{2,COM}$-PtCo/C catalysts, which could thus induce the highest performance in PEM fuel cells. Regarding the stability test by the repetitive LSV, the drastic drop of normalized $j_L$ was observed for the PtCo/C catalyst, while that of the $TiO_2$-PtCo/C catalyst increased to its maximum value at around 2,000 LSV-cycle and dropped afterward. The impedance spectra displayed the decrease of electrolyte resistance along the repetitive LSV, due to the dissolution of metal elements into the electrolyte. The ESA of the catalyst increased with the increasing LSV cycles, due to the dissolution of the Co atom from the catalyst layer and the change of the Pt crystalline structure. In summary, a home-prepared $TiO_{2,CVD}$ exhibited an effective property to

enhance the activity and stability of the PtCo/C catalyst, which can produce the current density of 434 mA/cm$^2$ (277 mW/cm$^2$) at 0.6 V with performance loss of around 40% after a 6,000 LSV-cycle, due to its excellent corrosion resistance property and preparation/incorporation technique.

## 7.2 Recommendations

There are several additional ideas for further research that have been focused by the studies undertaken for this dissertation.

1. This study has investigated the effects of metal oxide and PtCo/C catalyst incorporation on activity and stability of ORR in PEM fuel cell. This has shown the both significant negative and positive results. The negative effect came from the addition of $CeO_2$ and $MoO_2$ that had the large particle size. In the other word, the small particle size $TiO_2$ provided the best of ESA, ORR activity, PEM fuel cell performance and also stability. Then, to get the precious result, the effect of metal oxide size should be more studied.

2. The metal oxide and PtCo/C catalyst incorporation method should be further explored. In this study, the metal oxide was created as the interlayer between GDLs and catalyst layer which increased the resistance of electrode. Then, it would benefit additional investigation in order to determine how to mix the metal oxide with the catalyst to get the high catalytic performance.

3. The catalyst stability should be determined in the PEM fuel cell application.

REFERENCES

# REFERENCES

[1] M.M. Hasani-Sadrabadi, S.H. Emami, R. Ghaffarian, H. Moaddel. Nanocomposite Membranes Made from Sulfonated Poly(ether ether ketone) and Montmorillonite Clay for Fuel Cell Applications. Energy & Fuels, 22 (2008): 2539-2542.

[2] Y. Tang, W. Yuan, M. Pan, Z. Li, G. Chen, Y. Li. Experimental investigation of dynamic performance and transient responses of a kW-class PEM fuel cell stack under various load changes. Applied Energy, 87 (2010): 1410-1417.

[3] X. Zhang, J. Guo, J. Chen. The parametric optimum analysis of a proton exchange membrane (PEM) fuel cell and its load matching. Energy, 35 (2010): 5294-5299.

[4] C.W.B. Bezerra, L. Zhang, H. Liu, K. Lee, A.L.B. Marques, E.P. Marques, H. Wang, J. Zhang. A review of heat-treatment effects on activity and stability of PEM fuel cell catalysts for oxygen reduction reaction. Journal of Power Sources, 173 (2007): 891-908.

[5] K. Kinoshita. Electrochemical oxygen technology. John Wiley & Sons, 1992.

[6] H.A. Gasteiger, S.S. Kocha, B. Sompalli, F.T. Wagner. Activity benchmarks and requirements for Pt, Pt-alloy, and non-Pt oxygen reduction catalysts for PEMFCs. Applied Catalysis B: Environmental, 56 (2005): 9-35.

[7] M.T. Paffett, J.G. Beery, S. Gottesfeld. Oxygen Reduction at $Pt_{0.65}Cr_{0.35}$, $Pt_{0.2}Cr_{0.8}$ and Roughened Platinum. Journal of The Electrochemical Society, 135 (1988): 1431-1436.

[8] B.C. Beard, P.N. Ross. The Structure and Activity of Pt-Co Alloys as Oxygen Reduction Electrocatalysts. Journal of The Electrochemical Society, 137 (1990): 3368-3374.

[9] E. Antolini, J.R.C. Salgado, M.J. Giz, E.R. Gonzalez. Effects of geometric and electronic factors on ORR activity of carbon supported Pt–Co electrocatalysts in PEM fuel cells. International Journal of Hydrogen Energy, 30 (2005): 1213-1220.

[10] P.A. Thiel, M. Shen, D.-J. Liu, J.W. Evans. Coarsening of Two-Dimensional Nanoclusters on Metal Surfaces. The Journal of Physical Chemistry C, 113 (2009): 5047-5067.

[11] E.F. Holby, W. Sheng, Y. Shao-Horn, D. Morgan. Pt nanoparticle stability in PEM fuel cells: influence of particle size distribution and crossover hydrogen. Energy & Environmental Science, 2 (2009): 865-871.

[12] F. Hasche, M. Oezaslan, P. Strasser. Activity, stability and degradation of multi walled carbon nanotube (MWCNT) supported Pt fuel cell electrocatalysts. Physical Chemistry Chemical Physics, 12 (2010): 15251-15258.

[13] C. Xu, P.K. Shen. Novel $Pt/CeO_2/C$ catalysts for electrooxidation of alcohols in alkaline media. Chemical Communications, (2004): 2238-2239.

[14] C. Xu, P.K. Shen, X. Ji, R. Zeng, Y. Liu. Enhanced activity for ethanol electrooxidation on Pt–MgO/C catalysts. Electrochemistry Communications, 7 (2005): 1305-1308.

[15] Hydrogen fuel cell [Online]. http://www.hydrogen.energy.gov/pdfs/doe_fuelcell_factsheet.pdf [20 October 2015].

[16] R.P. O'Hayre, S.-W. Cha, W. Colella, F.B. Prinz. Fuel cell fundamentals. John Wiley & Sons New York, 2006.

[17] W. Vielstich, A. Lamm, H.A. Gasteiger. Handbook of Fuel Cells: Fundamentals Technology and Applications. Vol. 2, Electrocatalysis. Wiley, 2003.

[18] Fuel Cell: Proton exchange membrane fuel cell [Online]. http://file.scirp.org/Html/2-6401059_4954.htm: [20 October 2015].

[19] J. Larminie, A. Dicks, M.S. McDonald. Fuel cell systems explained. Wiley New York, 2003.

[20] I. Pilatowsky, R.J. Romero, C. Isaza, S. Gamboa, P. Sebastian, W. Rivera. Cogeneration fuel cell-sorption air conditioning systems. Springer Science & Business Media, 2011.

[21] Losses in fuel cell. [Online]. http://users.encs.concordia.ca/~pillay/fuel-cells.html: [20 October 2015].

[22] A. Appleby, F.F.F.C. Handbook. van Nostrand Reinhold. New York, 18 (1989).

[23] R. O'Hayre, D.M. Barnett, F.B. Prinz. The Triple Phase Boundary: A Mathematical Model and Experimental Investigations for Fuel Cells. Journal of The Electrochemical Society, 152 (2005): A439-A444.

[24] The technical targets of the U.S. Department of Energy for each component of MEAs for transportation applications. [Online]. http://energy.gov/sites/prod/files/2014/02/f8/fctt_roadmap_june2013.pdf: [14 November 2015].

[25] P. Kiatkittikul, T. Nohira, R. Hagiwara. Nonhumidified Fuel Cells Using N-Ethyl-N-methyl-pyrrolidinium Fluorohydrogenate Ionic Liquid-poly(Vinylidene Fluoride-Hexafluoropropylene) Composite Membranes. Energies, 8 (2015): 6202.

[26] A. Jayakumar, S. Sethu, M. Ramos, J. Robertson, A. Al-Jumaily. A technical review on gas diffusion, mechanism and medium of PEM fuel cell. Ionics, 21 (2015): 1-18.

[27] L. Cindrella, A.M. Kannan, J.F. Lin, K. Saminathan, Y. Ho, C.W. Lin, J. Wertz. Gas diffusion layer for proton exchange membrane fuel cells—A review. Journal of Power Sources, 194 (2009): 146-160.

[28] O.T. Holton, J.W. Stevenson. The Role of Platinum in Proton Exchange Membrane Fuel Cells. Platinum Metals Review, 57 (2013): 259-271.

[29] N.M. Marković, T.J. Schmidt, V. Stamenković, P.N. Ross. Oxygen Reduction Reaction on Pt and Pt Bimetallic Surfaces: A Selective Review. Fuel Cells, 1 (2001): 105-116.

[30] Nafion 117 membrane. [Online]. http://www.sigmaaldrich.com/catalog/product/aldrich/274674?lang=en&region=TH: [8 November 2015].

[31] H. Wu, D. Wexler, G. Wang. PtxNi alloy nanoparticles as cathode catalyst for PEM fuel cells with enhanced catalytic activity. Journal of Alloys and Compounds, 488 (2009): 195-198.

[32] E. Antolini, J.R.C. Salgado, E.R. Gonzalez. The stability of Pt–M (M = first row transition metal) alloy catalysts and its effect on the activity in low temperature fuel

cells: A literature review and tests on a Pt–Co catalyst. <u>Journal of Power Sources,</u> 160 (2006): 957-968.

[33] T. Toda, H. Igarashi, H. Uchida, M. Watanabe. Enhancement of the Electroreduction of Oxygen on Pt Alloys with Fe, Ni, and Co. <u>Journal of The Electrochemical Society,</u> 146 (1999): 3750-3756.

[34] S. Koh, J. Leisch, M.F. Toney, P. Strasser. Structure-Activity-Stability Relationships of Pt━Co Alloy Electrocatalysts in Gas-Diffusion Electrode Layers. <u>The Journal of Physical Chemistry C,</u> 111 (2007): 3744-3752.

[35] S. Takenaka, A. Hirata, E. Tanabe, H. Matsune, M. Kishida. Preparation of supported Pt–Co alloy nanoparticle catalysts for the oxygen reduction reaction by coverage with silica. <u>Journal of Catalysis,</u> 274 (2010): 228-238.

[36] S.S. Kocha. Chapter 3 - Electrochemical Degradation: Electrocatalyst and Support Durability, in M.M.M.C.K.N. Veziroglu (Ed.), <u>Polymer Electrolyte Fuel Cell Degradation,</u> pp. 89-214. Boston: Academic Press, 2012.

[37] Dissolution mechanisms for Pt in acid media. [Online]. <u>http://d-nb.info/1021976377/34:</u> [8 November 2015].

[38] E. Bailón-García, F. Maldonado-Hódar, A. Pérez-Cadenas, F. Carrasco-Marín. Catalysts Supported on Carbon Materials for the Selective Hydrogenation of Citral. <u>Catalysts,</u> 3 (2013): 853.

[39] Z.Y. Liu, J.L. Zhang, P.T. Yu, J.X. Zhang, R. Makharia, K.L. More, E.A. Stach. Transmission Electron Microscopy Observation of Corrosion Behaviors of Platinized Carbon Blacks under Thermal and Electrochemical Conditions. <u>Journal of The Electrochemical Society,</u> 157 (2010): B906-B913.

[40] L.M. Roen, C.H. Paik, T.D. Jarvi. Electrocatalytic Corrosion of Carbon Support in PEMFC Cathodes. <u>Electrochemical and Solid-State Letters,</u> 7 (2004): A19-A22.

[41] J. Wu, X.Z. Yuan, J.J. Martin, H. Wang, J. Zhang, J. Shen, S. Wu, W. Merida. A review of PEM fuel cell durability: Degradation mechanisms and mitigation strategies. <u>Journal of Power Sources,</u> 184 (2008): 104-119.

[42] E. Antolini, R.R. Passos, E.A. Ticianelli. Electrocatalysis of oxygen reduction on a carbon supported platinum–vanadium alloy in polymer electrolyte fuel cells. Electrochimica Acta, 48 (2002): 263-270.

[43] V. Stamenkovic, B.S. Mun, K.J. Mayrhofer, P.N. Ross, N.M. Markovic, J. Rossmeisl, J. Greeley, J.K. Nørskov. Changing the activity of electrocatalysts for oxygen reduction by tuning the surface electronic structure. Angewandte Chemie, 118 (2006): 2963-2967.

[44] M.P. Hyman, J.W. Medlin. Effects of Electronic Structure Modifications on the Adsorption of Oxygen Reduction Reaction Intermediates on Model Pt(111)-Alloy Surfaces. The Journal of Physical Chemistry C, 111 (2007): 17052-17060.

[45] A.L. Linsebigler, G. Lu, J.T. Yates. Photocatalysis on $TiO_2$ Surfaces: Principles, Mechanisms, and Selected Results. Chemical Reviews, 95 (1995): 735-758.

[46] U. Diebold. Structure and properties of $TiO_2$ surfaces: a brief review. Appl Phys A, 76 (2003): 681-687.

[47] A. Di Paola, M. Addamo, M. Bellardita, E. Cazzanelli, L. Palmisano. Preparation of photocatalytic brookite thin films. Thin Solid Films, 515 (2007): 3527-3529.

[48] $TiO_2$ structure. [Online]. https://pavemaintenance.wikispaces.com/file/view/TiO2_ball_and_stick.jpg/32123 2034/880x220/TiO2_ball_and_stick.jpg: [10 November 2015].

[49] D. Devilliers, M.T. Dinh, E. Mahé, D. Krulic, N. Larabi, N. Fatouros. Behaviour of titanium in sulphuric acid-Application to DSAs. Journal of New Materials for Electrochemical Systems, 9 (2006): 221.

[50] Physical property of $TiO_2$ [Online]. http://ruby.colorado.edu/~smyth/min/tio2.html: [10 November 2015].

[51] G.D. Considine. Molybdenum. Van Nostrand's Encyclopedia of Chemistry, (2005): 1038-1040.

[52] L.C. Dufour, O. Bertrand, N. Floquet. Chemical reactivity of (010)$MoO_3$: a structural study of the $MoO_2$ formation in molecular hydrogen. Surface Science, 147 (1984): 396-412.

[53] V. Henrich, P. Cox. The surface science of metal oxidesCambridge Univ. Press, Cambridge, (1994).

[54] F. Werfel, E. Minni. Photoemission study of the electronic structure of Mo and Mo oxides. Journal of Physics C: Solid State Physics, 16 (1983): 6091.

[55] A. Gulino, S. Parker, F. Jones, R. Egdell. Influence of metal–metal bonds on electron spectra of $MoO_2$ and $WO_2$. J. Chem. Soc., Faraday Trans., 92 (1996): 2137-2141.

[56] Structure of molybdenum dioxide ($MoO_2$) [Online].   http://goo.gl/9cDpGR: [10 November 2015].

[57] M. Pourbaix. Atlas of electrochemical equilibria in aqueous solutions. (1966).

[58] B. Choudhury, P. Chetri, A. Choudhury. Oxygen defects and formation of $Ce^{3+}$ affecting the photocatalytic performance of $CeO_2$ nanoparticles. RSC Advances, 4 (2014): 4663-4671.

[59] Structure of Ceria dioxide [Online].  https://goo.gl/OdN9Hu: [10 November 2015].

[60] E. Stoyanova, D. Stoychev. Corrosion behavior of stainless steels modified by cerium oxides layers. INTECH Open Access Publisher, 2012.

[61] P. Yu, S.A. Hayes, T.J. O'Keefe, M.J. O'Keefe, J.O. Stoffer. The Phase Stability of Cerium Species in Aqueous Systems II. The Systems. Equilibrium Considerations and Pourbaix Diagram Calculations. Journal of the Electrochemical Society, 153 (2006): C74-C79.

[62] J. Geus. Production and Thermal Pretreatmewt of Supported Catalysts. Studies in Surface Science and Catalysis, 16 (1983): 1-33.

[63] M. Schlesinger, M. Paunovic. Modern electroplating. John Wiley & Sons, 2011.

[64] Y. Saejeng, N. Tantavichet. Preparation of Pt–Co alloy catalysts by electrodeposition for oxygen reduction in PEMFC. Journal of Applied Electrochemistry, 39 (2009): 123-134.

[65] J. Creighton, P. Ho. Introduction to chemical vapor deposition (CVD). Chemical vapor deposition, (2001): 2.

[66] A.C. Jones, M.L. Hitchman. Chemical vapour deposition: precursors, processes and applications. Royal Society of Chemistry, 2009.

[67] H.R. Colón-Mercado, B.N. Popov. Stability of platinum based alloy cathode catalysts in PEM fuel cells. Journal of Power Sources, 155 (2006): 253-263.

[68] S.C. Zignani, E. Antolini, E.R. Gonzalez. Evaluation of the stability and durability of Pt and Pt–Co/C catalysts for polymer electrolyte membrane fuel cells. Journal of Power Sources, 182 (2008): 83-90.

[69] N. Elezovic, B. Babic, V. Radmilovic, L.M. Vracar, N. Krstajic. Synthesis and characterization of $MoO_x$-Pt/C and $TiO_x$-Pt/C nano-catalysts for oxygen reduction. Electrochimica Acta, 54 (2009): 2404-2409.

[70] K. Fugane, T. Mori, D.R. Ou, A. Suzuki, H. Yoshikawa, T. Masuda, K. Uosaki, Y. Yamashita, S. Ueda, K. Kobayashi. Activity of oxygen reduction reaction on small amount of amorphous $CeO_x$ promoted Pt cathode for fuel cell application. Electrochimica Acta, 56 (2011): 3874-3883.

[71] V. Rico-Pérez, A. Bueno-López. Effect of $RhO_x/CeO_2$ Calcination on Metal-Support Interaction and Catalytic Activity for $N_2O$ Decomposition. Applied Sciences, 4 (2014): 468-481.

[72] L. Jinlong, L. Tongxiang, L. Hongyun. Effect of grain refinement and electrochemical nitridation on corrosion resistance of the 316L stainless steel for bipolar plates in PEMFCs environment. Journal of Power Sources, 293 (2015): 692-697.

[73] T. Ungár, J. Gubicza, G. Tichy, C. Pantea, T. Zerda. Size and shape of crystallites and internal stresses in carbon blacks. Composites Part A: Applied Science and Manufacturing, 36 (2005): 431-436.

[74] Y. Ra, J. Lee, I. Kim, S. Bong, H. Kim. Preparation of Pt–Ru catalysts on Nafion (Na+)-bonded carbon layer using galvanostatic pulse electrodeposition for proton-exchange membrane fuel cell. Journal of Power Sources, 187 (2009): 363-370.

[75] Z. Wang, G. Yin, P. Shi, Y. Sun. Novel Pt–Ru–Ni/C catalysts for methanol electro-oxidation in acid medium. Electrochemical and solid-state letters, 9 (2006): A13-A15.

[76] Z. Yan, J. Xie, J. Jing, M. Zhang, W. Wei, S. Yin. $MoO_2$ nanocrystals down to 5 nm as Pt electrocatalyst promoter for stable oxygen reduction reaction. International Journal of Hydrogen Energy, 37 (2012): 15948-15955.

[77] A.G. Pandolfo, A.F. Hollenkamp. Carbon properties and their role in supercapacitors. Journal of Power Sources, 157 (2006): 11-27.

[78] K.H. Radeke, K.O. Backhaus, A. Swiatkowski. Electrical conductivity of activated carbons. Carbon, 29 (1991): 122-123.

[79] M. Polovina, B. Babić, B. Kaluderović, A. Dekanski. Surface characterization of oxidized activated carbon cloth. Carbon, 35 (1997): 1047-1052.

[80] A.J. Bard, L.R. Faulkner. Electrochemical methods: fundamentals and applications. Wiley New York, 1980.

[81] H.B. Yu, J.-H. Kim, H.-I. Lee, M.A. Scibioh, J. Lee, J. Han, S.P. Yoon, H.Y. Ha. Development of nanophase $CeO_2$-Pt/C cathode catalyst for direct methanol fuel cell. Journal of Power Sources, 140 (2005): 59-65.

[82] C. Xu, P.K. Shen. Electrochamical oxidation of ethanol on $Pt-CeO_2$/C catalysts. Journal of Power Sources, 142 (2005): 27-29.

[83] C. Xu, R. Zeng, P.K. Shen, Z. Wei. Synergistic effect of $CeO_2$ modified Pt/C catalysts on the alcohols oxidation. Electrochimica Acta, 51 (2005): 1031-1035.

[84] A.M. Eppler, I.M. Ballard, J. Nelson. Charge transport in porous nanocrystalline titanium dioxide. Physica E: Low-dimensional Systems and Nanostructures, 14 (2002): 197-202.

[85] K. Pomoni, M.V. Sofianou, T. Georgakopoulos, N. Boukos, C. Trapalis. Electrical conductivity studies of anatase $TiO_2$ with dominant highly reactive {0 0 1} facets. Journal of Alloys and Compounds, 548 (2013): 194-200.

[86] J. Kim, S.M. Lee, S. Srinivasan, C.E. Chamberlin. Modeling of proton exchange membrane fuel cell performance with an empirical equation. Journal of the Electrochemical Society, 142 (1995): 2670-2674.

[87] E. Antolini, L. Giorgi, A. Pozio, E. Passalacqua. Influence of Nafion loading in the catalyst layer of gas-diffusion electrodes for PEFC. Journal of Power Sources, 77 (1999): 136-142.

[88] E.I. Santiago, R.A. Isidoro, M.A. Dresch, B.R. Matos, M. Linardi, F.C. Fonseca. Nafion–TiO2 hybrid electrolytes for stable operation of PEM fuel cells at high temperature. Electrochimica Acta, 54 (2009): 4111-4117.

[89] Z. Liu, B. Guo, J. Huang, L. Hong, M. Han, L.M. Gan. Nano-TiO$_2$-coated polymer electrolyte membranes for direct methanol fuel cells. Journal of Power Sources, 157 (2006): 207-211.

[90] C. Montero-Ocampo, J. Vargas Garcia, E. Arce Estrada. Comparison of TiO$_2$ and TiO2-CNT as cathode catalyst supports for ORR. International Journal of Electrochemical Science, 8 (2013): 1278-1280.

[91] S.-Y. Huang, P. Ganesan, B.N. Popov. Electrocatalytic activity and stability of niobium-doped titanium oxide supported platinum catalyst for polymer electrolyte membrane fuel cells. Applied Catalysis B: Environmental, 96 (2010): 224-231.

[92] A. Fujishima, K. Hashimoto, T. Watanabe. TiO$_2$ photocatalysis: fundamentals and applications. BKC Incorporated, 1999.

[93] S.B. Abu Suilik, D. Shimamoto, H. Kitagawa, K. Hasezaki, Y. Noda. Experimental study of nucleation and quality of CVD diamond adopting two-step deposition approach using MPECVD. Diamond and Related Materials, 15 (2006): 1765-1772.

[94] J. Zhang, X. Cui, Z. Shi, B. Wu, Y. Zhang, B. Zhang. Nucleation and growth of ZnO films on Si substrates by LP-MOCVD. Superlattices and Microstructures, 71 (2014): 23-29.

[95] C. Kittel, H. Kroemer, Thermal physics 2nd ed, in: C. Kittel, H. Kroemer (Eds.), Freeman, 1980.

[96] R.W. Chia, C.C. Wang, J.J. Lee. Effect of adatom mobility and substrate finish on film morphology and porosity: Thin chromium film on hard disk. Journal of magnetism and magnetic materials, 209 (2000): 45-49.

[97] J. Wagner, C. Mitterer, M. Penoy, C. Michotte, W. Wallgram, M. Kathrein. The effect of deposition temperature on microstructure and properties of thermal CVD TiN coatings. International Journal of Refractory Metals and Hard Materials, 26 (2008): 120-126.

[98] K. Tiido, N. Alexeyeva, M. Couillard, C. Bock, B.R. MacDougall, K. Tammeveski. Graphene–TiO$_2$ composite supported Pt electrocatalyst for oxygen reduction reaction. Electrochimica Acta, 107 (2013): 509-517.

[99] G. Selvarani, S. Maheswari, P. Sridhar, S. Pitchumani, A. Shukla. Carbon-Supported Pt–TiO$_2$ as a Methanol-Tolerant Oxygen-Reduction Catalyst for DMFCs. Journal of the Electrochemical Society, 156 (2009): B1354-B1360.

[100] B. Ruiz-Camacho, H.R. Santoyo, J. Medina-Flores, O. Álvarez-Martínez. Platinum deposited on TiO$_2$-C and SnO$_2$-C composites for methanol oxidation and oxygen reduction. Electrochimica Acta, 120 (2014): 344-349.

[101] L. Timperman, A.S. Gago, N. Alonso-Vante. Oxygen reduction reaction increased tolerance and fuel cell performance of Pt and Ru$_x$Se$_y$ onto oxide–carbon composites. Journal of Power Sources, 196 (2011): 4290-4297.

[102] L. Xiong, A. Manthiram. Synthesis and characterization of methanol tolerant Pt/TiO$_x$/C nanocomposites for oxygen reduction in direct methanol fuel Cells. Electrochimica Acta, 49 (2004): 4163-4170.

[103] S. Maheswari, S. Karthikeyan, P. Murugan, P. Sridhar, S. Pitchumani. Carbon-supported Pd–Co as cathode catalyst for APEMFCs and validation by DFT. Physical Chemistry Chemical Physics, 14 (2012): 9683-9695.

[104] G. Álvarez, M. Mamlouk, K. Scott. An investigation of palladium oxygen reduction catalysts for the direct methanol fuel cell. International Journal of Electrochemistry, 2011 (2011).

[105] H.-J. Kim, D.-Y. Kim, H. Han, Y.-G. Shul. PtRu/C-Au/TiO$_2$ electrocatalyst for a direct methanol fuel cell. Journal of power sources, 159 (2006): 484-490.

[106] S. Von Kraemer, K. Wikander, G. Lindbergh, A. Lundblad, A.E. Palmqvist. Evaluation of $TiO_2$ as catalyst support in Pt-$TiO_2$/C composite cathodes for the proton exchange membrane fuel cell. Journal of Power Sources, 180 (2008): 185-190.

[107] J. Xu, T. Zhao, W. Yang, S. Shen. Effect of surface composition of Pt-Au alloy cathode catalyst on the performance of direct methanol fuel cells. international journal of hydrogen energy, 35 (2010): 8699-8706.

[108] S.C. Zignani, E. Antolini, E.R. Gonzalez. Stability of Pt–Ni/C (1: 1) and Pt/C electrocatalysts as cathode materials for polymer electrolyte fuel cells: effect of ageing tests. Journal of Power Sources, 191 (2009): 344-350.

[109] T. Lopes, E. Antolini, E. Gonzalez. Carbon supported Pt–Pd alloy as an ethanol tolerant oxygen reduction electrocatalyst for direct ethanol fuel cells. international journal of hydrogen energy, 33 (2008): 5563-5570.

[110] N. Chaisubanan, K. Pruksathorn, H. Vergnes, M. Hunsom. Effect of the $TiO_2$ phase and loading on oxygen reduction reaction activity of PtCo/C catalysts in proton exchange membrane fuel cells. Korean Journal of Chemical Engineering, (2015): 1-9.

[111] H. Steininger, S. Lehwald, H. Ibach. Adsorption of oxygen on Pt (111). Surface Science, 123 (1982): 1-17.

[112] N.H. Linh, T.Q. Nguyen, W.A. Diño, H. Kasai. Effect of oxygen vacancy on the adsorption of $O_2$ on anatase $TiO_2$ (001): A DFT-based study. Surface Science, 633 (2015): 38-45.

[113] K. Hyun, J.H. Lee, C.W. Yoon, Y. Kwon. The effect of platinum based bimetallic electrocatalysts on oxygen reduction reaction of proton exchange membrane fuel cells. Int. J. Electrochem. Sci, 8 (2013): 11752-11767.

[114] L. Lai, J.R. Potts, D. Zhan, L. Wang, C.K. Poh, C. Tang, H. Gong, Z. Shen, J. Lin, R.S. Ruoff. Exploration of the active center structure of nitrogen-doped graphene-based catalysts for oxygen reduction reaction. Energy & Environmental Science, 5 (2012): 7936-7942.

[115] U. Paulus, A. Wokaun, G. Scherer, T. Schmidt, V. Stamenkovic, V. Radmilovic, N. Markovic, P. Ross. Oxygen reduction on carbon-supported Pt-Ni and Pt-Co alloy catalysts. The Journal of Physical Chemistry B, 106 (2002): 4181-4191.

[116] M. Hunsom. Electrochemical impedance spectroscopy (EIS) for PEM fuel cells. Spectroscopic Properties of Inorganic and Organometallic Compounds: Techniques, Materials and Applications, 42 (2011): 196-247.

[117] H.R. Colón-Mercado, H. Kim, B.N. Popov. Durability study of $Pt_3 Ni_1$ catalysts as cathode in PEM fuel cells. Electrochemistry Communications, 6 (2004): 795-799.

[118] Z.-Z. Jiang, D.-M. Gu, Z.-B. Wang, W.-L. Qu, G.-P. Yin, K.-J. Qian. Effects of anatase $TiO_2$ with different particle sizes and contents on the stability of supported Pt catalysts. Journal of Power Sources, 196 (2011): 8207-8215.

[119] C. Odetola, L. Trevani, E.B. Easton. Enhanced activity and stability of $Pt/TiO_2/carbon$ fuel cell electrocatalyst prepared using a glucose modifier. Journal of Power Sources, 294 (2015): 254-263.

[120] S. Ohyagi, T. Sasaki. Durability of a PEMFC Pt–Co cathode catalyst layer during voltage cycling tests under supersaturated humidity conditions. Electrochimica Acta, 102 (2013): 336-341.

REFERENCES

APPENDIX

**Appendix A**

A.1 The crystalline size of metal from XRD diffraction peak was calculated by Debye-Scherrer equation.

$$L = \frac{0.9\lambda_{k\alpha1}}{B_{2\theta}\cos\theta_{max}}$$ (A.1)

Where $L$      is crystallite size (nm)

$\lambda_{kal}$      is wave range of X-rays (0.154056 nm)

$\beta_{2\theta}$      is *full width at half maximum* (rad)

$\theta$      is Bragg angle (rad)

     The example of Pt/C (commercial) crystalline size calculation.

$\beta_{2\theta}$ = 3.037 degree (0.053 rad)

$2\theta$ = 39.79 degree (0.347 rad)

$\cos\theta$ = cos(0.347) = 0.9403

Substitute in the eq. (A.1) then,

$$L = \frac{0.9 \times 0.154}{0.053 \times 0.9403} = 2.78 \text{ nm.}$$

A.2 The *d*-spacing was calculated by Bragg's law to determine the inter planar spacing d (this is experimental d value depend on $2\theta$ measured experimentally)

$$\lambda = 2d_{hkl}\sin\theta_{hkl}$$ (A.2)

Where $\lambda_{kal}$      is wave range of X-rays (0.154056 nm)

$d_{kal}$      is *d*-spacing (nm)

$\theta$      is Bragg angle (rad)

The example of Pt/C (commercial) crystalline size calculation. Choose a Pt(111) plane for this calculation.

$$\lambda = 2d_{hkl}\sin\theta_{hkl}$$

$2\theta$ = 39.79 degree (0.347 rad)

$\sin\theta = \sin(0.347) = 0.3401$

Substitute in the eq. (A.2) then,

$$d_{hlk} = \frac{0.154}{2x0.3401} = 0.226 \text{ nm.}$$

Appendix B


The ESA of catalyst can be estimated from the hydrogen desorption peak (Figure. B1) according to Eq.(B.1):
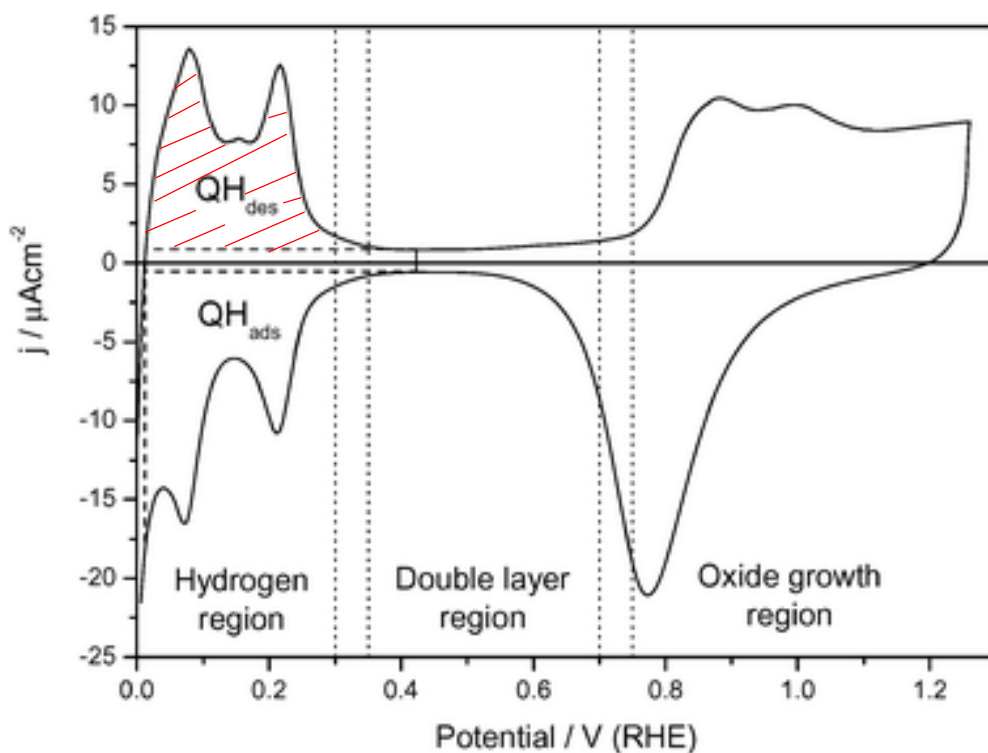


Figure B1. Integrated H$_{des}$ peak area of cyclic votammogram


$$ESA = \frac{Q_H}{[M] \times 0.21}$$ (B.1)


Where $Q_H$ is the charge for hydrogen desorption (C/cm$^2$)

0.21 is the charge required to oxidize a monolayer of H$_2$ on bright Pt and (mC/cm$^2$)

[M] is the metal loading of Pt on the electrode (mg$_{Pt}$/cm$^2$)

**The example of ESA calculation for PtCo/C catalyst**

- Integrated peak area = 7.452 mC/cm$^2$

- Pt loading = 0.075 mg/cm$^2$

Substitute in eq. (B.1) then,

$$ESA = \frac{7.452}{0.21 \times 0.075} = 473.14 \ cm^2\big/mg_{Pt}$$

$$= 47.314 \ m^2\big/g_{Pt}$$

Appendix C

The relationship between the current density and the rotation rate can be expressed by the Koutecky-Levich equation (Eq.(C.1)). This equation is valid for a first order process with respect to the diffusion species [88].

$$\frac{1}{j} = \frac{1}{j_k} + \frac{1}{B\omega^{1/2}}$$
(C.1)

and where $B$ is estimated by Eq. (C.2),

$$B = 0.62n_e FD^{2/3}v^{-1/6}C$$
(C.2)

Here, $j_k$     is the kinetic current density,

     $\omega$     is the angular velocity (rad/sec),

     $n_e$     is the number of involved electrons,

     $F$     is the Faraday's constant (96,485 C/mol),

     $D$     is the diffusion coefficient of oxygen in solution ($1.9 \times 10^{-5}$ cm$^2$/s),

     $v$     is the kinematics viscosity (0.01 cm$^2$/s)

     $C$     is the oxygen concentration in the bulk solution ($1.1 \times 10^{-6}$ mol/cm$^3$).

Or,                    $B = (const.)(n_e)$
(C.3)

     $Cnost.$ is 0.1001,

     $n_e$     is the number of involved electrons

**The example of kinetic current density and number of electron calculation for PtCo/C catalyst**

- Selected the voltage in the range of kinetic – mass transfer mixed region of linear sweep voltammogram.

- Plot between 1/|i| vs 1/$\omega^{1/2}$ to get the slope and interception of linear trend line
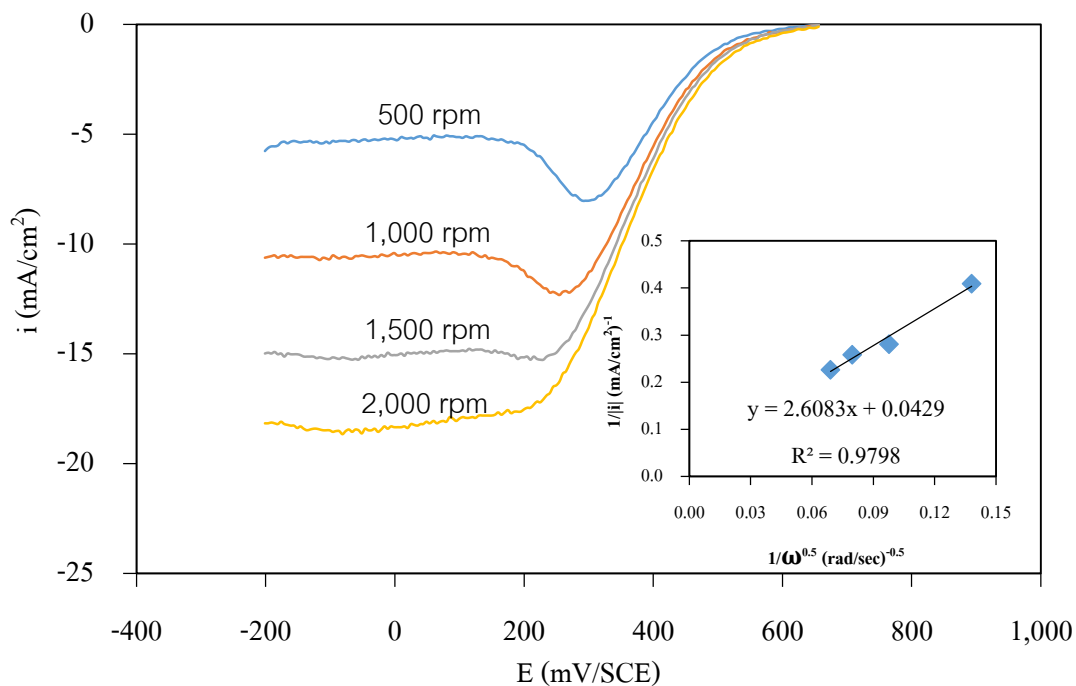
Figure C.1 Example plot of voltammogram for the ORR of $TiO_2$-PtCo/C catalyst in 0.5 M $H_2SO_4$ ($O_2$-Sat.) at scan rate of 10 mV/s.

From Figure C.1 (inset); substitute slope = 2.6083 and interception = 0.0429 in eq. C.3

Then,
$$B = \frac{1}{slope}$$

$$0.1001(n_e) = \frac{1}{2.6083}$$

$$n_e = 3.80$$

And
$$\frac{1}{i_k} = interception$$

$$i_k = \frac{1}{0.0429}$$

$$i_k = 23.31 \text{ mA/cm}^2 \qquad \underline{\text{Ans.}}$$

# VITA

Miss Napapat Chaisubanan was born on February 16, 1987 in Kanchanaburi Thailand. She received her B.Sc. degree in Physics and M.Sc. degree in Fuel Technology from Chulalongkorn University. She joined the Department of Chemical Technology, Chulalongkorn University as Ph.D. student in 2011. She has receive the scholarship from the Royal Golden Jubilee Ph.D. program, Thailand research fund.